2012

Variance In Fade-time Of A Gamma-gamma Distributed Irradiance Signal

Troy T. Leclerc
University of Central Florida

VARIANCE IN FADE-TIME OF A GAMMA-GAMMA DISTRIBUTED IRRADIANCE SIGNAL

by

TROY T. LECLERC
B.S.E.E. University of Central Florida, 2008
M.S.E.E. University of Central Florida, 2010

A dissertation submitted in partial fulfillment of the requirements
for the degree of Doctor of Philosophy
in the School of Electrical Engineering and Computer Science
in the College of Engineering and Computer Science
at the University of Central Florida
Orlando, FL

Summer Term
2012

Major Professor: Ronald L. Phillips

ABSTRACT

Free-space optical communications are predominantly hindered by optical turbulence, an effect caused by temperature and pressure variations within the atmosphere. The result is an optical wave interfering with itself due to multipath propagation via tiny refractive-index fluctuations across the wave-front. Optical communication systems are affected when the channel conditions induce fading in the irradiance signal that is received at the detector. The nature of optical interference imparted by the atmosphere is a random process and therefore the received irradiance signal is often characterized by an appropriate probability density function (PDF). Data collected during past free-space optical experiments in the atmosphere support the gamma-gamma distribution as a practical PDF model for received irradiance fluctuations, although the irradiance fluctuations do occasionally tend towards a lognormal distribution.

Utilization of the gamma-gamma irradiance PDF allows for calculation of statistical moments of the irradiance threshold level-crossing distribution. Presented analysis focuses on the results of the gamma-gamma irradiance PDF. Previously, expressions were developed for the expected number of gamma-gamma distributed irradiance threshold level-crossings. Expressions for the mean square number of gamma-gamma distributed irradiance threshold level-crossings are derived and presented. The derived expressions lead to the mean and variance of signal fade time. Outcomes of the derived expressions are presented in relation to free-space optical communication system performance.

Comparisons are made between the theoretical analysis and experimental data taken at the Innovative Science and Technology Facility (ISTEF) located at the Kennedy Space Center in Cape Canaveral, Florida. The strength of the atmospheric turbulence is often characterized by three measurable parameters: the refractive index structure constant C_n^2, the inner scale l_0, and the outer scale L_0. The optical path ($L{\sim}1km$) was instrumented such that direct comparisons could be drawn between the measured atmospheric turbulence parameters and the parameters of the gamma-gamma irradiance model. Variance of fade time data were found to agree well for smaller apertures where effects of aperture averaging are not present and in cases where scintillation is weak to moderate. It is suggested that a more appropriate PDF, with a heavier focus on aperture averaging, may be applied in future studies of these fade statistics.

ACKNOWLEDGMENTS

I extend my gratitude to Dr. Ronald Phillips and Dr. Larry Andrews for every bit of the effort they have put forth into my continuing education. I would like to give thanks to Dr. John Stryjewski for his support and expertise in engineering as well as mission management. I thank every person that works, and has worked, with my research group at the Innovative Science and Testing Experimentation Facility. I also thank the professors I had the privilege of experiencing during my studies at the University of Central Florida, as well as other faculty members that I have worked with during my graduate career. Most of all, I would like to thank my friends and family for their continued love and support.

TABLE OF CONTENTS

LIST OF FIGURES

LIST OF TABLES

LIST OF SYMBOLS AND NOTATION

$\langle \cdot \rangle$	Ensemble average
A	Surface area
b^2	Variance of the time derivative of a stationary Gaussian random process
C_n^2	Refractive index structure constant
D_n	Refractive index structure function
F_T	Fade threshold parameter
f	Focal length
h	Heat transfer coefficient
I	Irradiance signal
$\dot{I}$	Time derivative of irradiance signal
I_T	Irradiance threshold level
k	Optical wave number
$K_\gamma(\cdot)$	Modified Bessel function of the second kind
L	Optical path length
L_o	Outer scale of atmospheric turbulence
l_0	Inner scale of atmospheric turbulence
$M_I(\cdot)$	Arbitrary integral function
n	Refractive index
$N^{(j)}(\cdot)$	Number of level crossings in the j^{th} time interval
$\overline{n(\cdot)}$	Mean number of level crossings

$\overline{n^2(\cdot)}$	Mean square number of level crossings
P	Atmospheric pressure
$p_X(\cdot)$	Probability density function of random variable X
$p_i(\cdot)$	Joint PDF of a signal and its time derivative at i instances in time
$\dot{Q}$	Heat transfer rate
$\dot{q}''$	Heat flux
$\boldsymbol{R}$	Separation vector
RH	Relative humidity
$\boldsymbol{r}_i$	i^{th} position vector
r_0	Fried's coherence length
$StDEV[\cdot]$	Standard deviation
T	Temperature
t	Denotes time variable
t_n	n^{th} instant in time
U_0	Complex field amplitude
$u(\cdot)$	Heaviside step function
$VAR[\cdot]$	Variance
$v_\perp$	Cross-wind speed
$v_\parallel$	Parallel-wind speed
W_0	Beam Spot Radius
WS	Wind speed

W_{TH}	Temporal hour weight
w	Dummy variable
X	Arbitrary random variable
x	Horizontal Cartesian coordinate
Y	Arbitrary random variable
y	Vertical Cartesian coordinate
z	Longitudinal Cartesian coordinate
α	Gamma-Gamma large-scale parameter
β	Gamma-Gamma small-scale parameter
$\delta(\cdot)$	Dirac delta function
$\Gamma(\cdot)$	Gamma function
γ	Dummy variable
ρ_0	Spatial coherence length
ρ_{sp}	Spherical wave coherence length
Λ_0	Refractive beam parameter
λ	Wavelength
ν_0	Quasi frequency
σ_I^2	Scintillation index
τ_i	Optical detection integration time
ΔT	Temperature difference
CDF	Cumulative distribution function

DARPA	Defense Advanced Research Projects Agency
FOENEX	Free-space Optical Experimental Network Experiment (DARPA)
FSO	Free-space Optical (communications network)
FSI	Florida Space Institute
IR	Infrared (optical wavelength)
ISTEF	Innovative Science and Technology Experimental Facility
MTF	Modulation transfer function
ORCA	Optical RF Communications Adjunct (DARPA)
PDF	Probability density function
UCF	University of Central Florida
WPRG	(UCF) Wave Propagation Research Group

1. INTRODUCTION

1.1 Free-Space Optical Communication Systems

Information transfer is continually given the expectation of and accomplishing the feat of attaining a greater quantity of data throughput. Large bandwidth (~10Gps) free-space optical (FSO) communication systems have been demonstrated in a range of scenarios from short distance to long distances; however, wide-spread use of such systems has not yet occurred [1-3]. It can be difficult to establish reliable FSO communication systems especially as the atmospheric conditions change on an hourly basis [4, 5]. Optical communication system engineers have long been familiarized with the twinkling phenomenon (similar to that of a star) imparted by the atmosphere when an object is viewed at a long distance. This concept is commonly referred to as *scintillation*; it is this phenomenon that can induce fading on an optical signal. Analyses of scintillation statistics are important for the reliable operation of an FSO system because information cannot be passed through the channel by the transmitter when the signal is not received by detector. This analysis will focus on real-time utilization of atmospheric parameters to model the amount of time the signal is available at the receiver side of the communication channel.

1.2 Atmospheric Turbulence

The universal method to understanding atmospheric turbulence and its interaction with optical system performance has been based on micrometeorology, use point measurements of local gradients, wind shear, and other parameters [6, 7] . However, to characterize atmospheric turbulence over long distances it is best to use macro-scale parameters such as air temperature, wind speed, wind direction, and relative humidity, all of which do not vary too greatly with

distance. The refractive index structure parameter, C_n^2 (units of meters raised to the negative two thirds) is widely considered one of the most important parameters in characterizing propagation through optical turbulence because it is directly related to the modulation transfer function (MTF) of the atmosphere [7]. Researchers such as Kopeika have introduced simple predictive meteorological models of C_n^2 based upon measurements of temperature, relative humidity, wind speed, and solar flux [6]. The effect of C_n^2 become increasingly detrimental over when analyzing longer propagation path lengths. It is therefore important to develop theory based upon parameters that can be directly related to the atmospheric conditions.

Since the 1970's there have been studies on the effects of scintillation on a laser beam propagating through the atmosphere. It has been found that C_n^2 was not adequate enough to fully encompass the effects of atmospheric turbulence. Since the models did not accurately predict experimental results, additional parameters were introduced in order describe the naturally occurring phenomena of atmospheric turbulence. Two additional parameters of importance are the inner scale of atmospheric turbulence l_0 and the outer scale of atmospheric turbulence L_0. Several methods have been developed to infer the useful atmospheric parameters such as the refractive index structure parameter, C_n^2, the temperature structure parameter C_T^2, the inner scale of turbulence l_0, the outer scale of turbulence L_0, and Fried's coherence length r_0. Many of these methods have been proven accurate in the presence of weak turbulence and over short path lengths [7]. Commercial instruments have been developed based upon 1970's theory, Scintec instruments are utilized in these experiments [8]. This research explores the phenomena of optical turbulence and aspects of its impact on the implementation of optical communication

systems. To characterize the optical path in the atmospheric turbulence, measurements from commercial instruments are used to estimate the channel model parameters.

1.3 Significant Contribution to Field of Study

If an optical wave is traveling along a path within a material, the characteristics of the traversed material impart a number of effects on the wave. For an optical wave propagating within atmospheric turbulence, the spatial state and the temporal evolution of the atmospheric propagation path impart characteristics of its statistical conditions. When situated with random fields it is a usual practice to develop models based upon direct observations or experiments. A large number of models have been created to predict the statistical structure of atmospheric turbulence with respect to optical wave propagation, namely those developed by the theories of Tatarskii and Kolmogorov [7, 9]. Although meaningful progress towards reliable system operation has been achieved, a number of circumstances arise in which models do not accurately predict the phenomena. This thesis will focus on the further development of predictive models that are practical from a modern communication engineering approach.

One such aspect of free-space optical communication system engineering deals with the fluctuations of a received irradiance signal, and the amount of time the irradiance signal spends below a specified irradiance threshold level. The expected value (first-moment) of the number of irradiance signal-irradiance threshold level crossings within a specified time interval can be related to the expected duration of time during which irradiance will signal fade, referred to as mean fade time. Much work in the past has been focused on mean fade time calculations for various models of the received irradiance probability density function [7, 10-13]. The distinction of this dissertation is to derive an expression for the variance of fade time, such that a standard

deviation of fade time can be represented about the mean fade time value. Specifically, several approaches will be taken in attempt to develop a model for the expected mean squared value (second-moment) of the number of irradiance signal- irradiance threshold level crossings within a specified time interval.

2. BACKGROUND

The city lights twinkling as seen from an airplane and the steam that appears to be rising from the asphalt on a hot day are a result of atmospheric turbulence. What is seen is due to differences in the refractive index of the atmosphere. Random fluctuations in the index of refraction cause: the spreading of the beam beyond that of the diffraction limit, random movement of the beam center (beam wander), loss of spatial coherence, and random fluctuations in the irradiance hereby referred to as scintillation [13]. The changes in refractive index are due to temperature gradients between the earth's surface and the atmosphere's air give rise to the phenomenon of atmospheric turbulence [5, 9, 14]. Atmospheric turbulence is normally described with the refractive-index structure parameter C_n^2, as it is the most commonly used term in literature to quantify refractive strength [9].

Nature usually presents itself in a manner that requires analysis beyond that which an outcome can be found deterministically. It is a standard approach of engineers, physicists, and mathematicians alike to describe such phenomena in terms of a random, or stochastic, process. In the study of random processes, random variables are used to represent quantities that which are non-deterministic. Examination of statistical behavior often leads to deeper insights to the phenomena of study. This section will provide an introduction to atmospheric turbulence, and briefly describe some of the tools used in study of the phenomenon.

2.1 Optical Wave Propagation

Optical waves may be practically described by the properties and shape of their wave front. We start by introducing the Cartesian coordinates x, y, and z. We will use x to denote horizontal

dependence, y to denote vertical dependence, and z to denote dependence along the optical path length (also referred to as propagation path L). As is practice, the complex number square root of negative one is denoted $i = \sqrt{-1}$. The vector $\boldsymbol{R}$ will represent the Cartesian coordinates in three spatial dimensions. The magnitude of $\boldsymbol{R}$ will be denoted by the radial distance R, given as

$$R = |\boldsymbol{R}| = \sqrt{x^2 + y^2 + z^2}. \tag{2.1}$$

Next, we briefly introduce the fundamental concept of wavelength λ (unit of meters), or alternatively their corresponding wave number $k = 2\pi/\lambda$ (unit of radians inverse meters). Detectors will only be operable within a range of wavelengths, efficiency will also depend on the chosen wavelength [15].

Generally there are three basic models in use to depict electromagnetic waves in the optical or near-infrared regimes: plane waves, spherical waves, and Gaussian beam waves [7]. The most basic type is an unbounded wave with amplitude E_0 and phase ϕ_0 that is constant with the respective horizontal and vertical Cartesian coordinates x and y. We will hereby refer to this form of optical wave as a *plane wave*, and describe it by the complex field amplitude U_0. The complex field amplitude of a plane wave is often written as a function of optical path length z, with constant horizontal dependence x and constant vertical dependence y as

$$U_0(x, y, z) = E_0(z)e^{i\phi(z)}. \tag{2.2}$$

A second type of unbounded wave model, which is derived from the from the properties of *point source* light propagation, is referred to as a *spherical wave* and its complex field amplitude is given as

$$U_0(x,y,z) = \lim_{R\to 0} \frac{E_0(z)e^{ikR}}{4\pi R}. \tag{2.3}$$

This type of wave is often used for a small-aperture source, or for a source that exhibits a large divergence angle [7]. It is noted that the spherical wave complex field amplitude will decrease with increasing distance from the radiation source. The experimental data presented in the analysis will follow the spherical wave model.

A third pertinent type of wave model is referred to as a *Gaussian beam wave*. This wave model exhibits a finite size, and is described as a function of optical path by $ABCD$ matrix transformations. The Gaussian-beam wave has a complex field amplitude given at the plane of the optical transmitter ($z = 0$) as

$$U_0(x,y,0) = a_0 \exp\left[-\frac{x^2+y^2}{W_0^2} - \frac{ik}{2F_0}\right], \tag{2.4}$$

where a_0 is the 'on-axis' ($x \cong y \cong 0$) amplitude, W_0 is the beam spot radius (radial distance from on-axis where the field amplitude is measured to be $a_0 \cdot e^{-1}$), and F_0 is the phase front radius of curvature [7]. Gaussian-beam wave models are useful in expediting many modeling aspects especially those of lumped elements [16, 17]. The Gaussian-beam model will not be utilized in this analysis because the spherical wave model provides a much readier approach to deriving parameters [7, 10, 13].

2.2 Optical Wave Detection

Electronic receivers of optical energy are modeled as *square-law devices*, where the output is a current generated proportional to the incident intensity. The primary focus of this analysis will be on the direct detection of intensity modulated optical waves transmitted through atmospheric turbulence. Optical signal power received by the photo-detector is measured proportional to the detector's output current, a relationship specified by manufacturer of the commercial instrument [18]. Direct detection of irradiance is that only the power of the optical signal is measured by the detector as photon energy is converted to electrical current. Measurements of the instantaneous power are made by averaging the photoelectrons generated by a detector over an integration period of time τ_i. This period is fixed within demonstrable limits. The generated photoelectrons may be due to the received laser signal, or the various noise sources present within the system. It is convenient to state the generated signal and noise currents in terms of a photoelectron rates. The signal current from the detector is given by

$$i_s = \left(\frac{\eta q}{h\nu}\right) GIA, \tag{2.5}$$

where I is the detected laser signal irradiance (units of Watts per meters squared), η is the detector efficiency, q is the electron charge (Coulombs), h is Planck's constant, ν is the optical frequency (unit of Hertz), G is the detector gain, and A is the area of the detector (units of meters squared) [6].

As a result of the photoelectron process, the received signal will be a detector current i_{det}

$$i_{det} = i_s + i_n, \tag{2.6}$$

where i_s is the detected optical signal and i_n is total the noise introduced throughout the

detection process. The noise current i_n will be considered to include all noise sources within the detected current. This term contains background (in-band sunlight irradiance) noise $i_{n,sun}$ and noise current generated by detector i_{det}. The detector noise current is stated explicitly as $i_n = i_{n,sun} + i_{n,det}$.The detector noise current will be present within the detector even if laser signal is not transmitted. If one were to place the lens cover over the lens system, as such to shield any incoming light and place the detector in complete darkness, we would expect the only noise present to be detector noise ($i_n = i_{n,det}$). To be captured as a digitized signal, the detector current must be transformed into a detector voltage v_{det} that measured across a minimal-detector resistance. One such method for measuring such voltage is a *transresistance amplifier*; this configuration provides extremely small input, output and feedback resistances [19]. Commercially packaged products geared towards research will be utilized in the detection scheme for this analysis to reduce noise values, alternative sources of error, and complexity of task.

To receive the transmitted laser signal at the receiver, an optical imaging system must be utilized. The system will generally consist of an assortment of collection lens to focus the incoming beam onto a charge-coupled device (CCD) whose output current can be digitally transcribed. Several filters should be employed to ensure maximum benefit in the receiver's signal to noise ratio. Namely, the light incident on the collection lens should be optically filtered to match the spectral shape of the transmit laser beam. For example, a 532nm laser beam with a factory-specified or experimentally measured spectral line width should be received by an imaging system that supports 532nm radiation and is filtered with a coating or glass-placement

that is transparent to only wavelengths within the spectral range of the transmitting laser. Optical filters covering a wide range of specifications: longpass, shortpass, and bandpass are readily purchasable on commercial websites such as Thorlabs [20]. An optical bandpass filter at the receiver with a spectral range matching the transmitter laser's spectral range will be assumed. Figure 1: Direct detection of an optical signal exemplifies a simple overview of the aforementioned scheme.

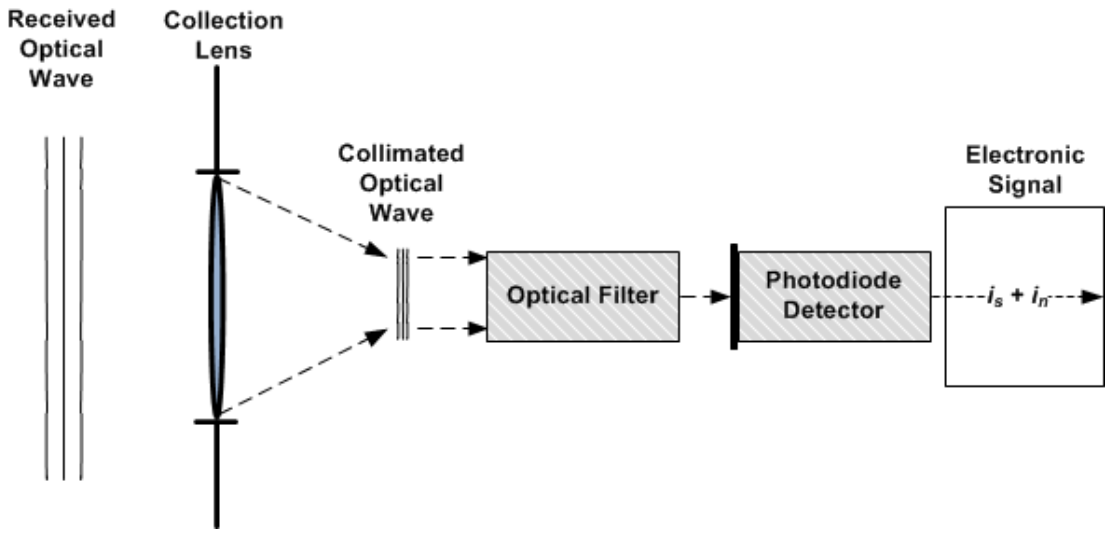

Figure 1: Direct detection of an optical signal.

For the experiments supporting the proceeding analysis, the primary source of noise within the detector receiver is assumed to be thermal noise. This assumption is taken to be valid because the detector was in an outdoor environment (at the Kennedy Space Center in Cape Canaveral, FL) and the components were not thermally cooled. When the photodiode receiver is exposed to sunlight, the noise current generated by in-band background (sunlight) is known to exceed the thermal noise current by many orders of magnitude. Note that in-band background (sunlight)

irradiance will contribute the biggest portion of noise when the detector is exposed to daytime conditions.

2.3 Effects of Atmospheric Turbulence on Optical Wave Propagation

The cycle of heating of the Earth's ground during the day and its cooling during night leads to the driving factor of atmospheric turbulence. The process of convection heat transfer is understood by taking that the heat flux $\dot{q}''$ is equal to the rate of heat transfer $\dot{Q}$ from the surface divided by surrounding surface area A, or $\dot{q}'' = \dot{Q}/A$ [21]. The heat flow vector is considered to be positive when heat flows from the surface to the fluid. From [21], the heat transfer coefficient, h, is defined in terms of the heat flux at the fluid to surface boundary and a temperature difference, ΔT as

$$h \equiv \frac{\dot{q}''}{\Delta T}, \tag{2.7}$$

with the units $\frac{W}{m^2} \cdot ℃$. The temperature difference is the difference between the temperature if the surface and the temperature of the fluid outside the boundary layer. The total rate at which heat is transferred from an isothermal surface is most conveniently obtained using the average heat transfer coefficient $\bar{h}$. The relationship between heat transfer, temperature difference, and surface area is then readily found to be

$$\dot{Q} = \bar{h}\, A\, \Delta T, \tag{2.8}$$

in units of Watts [21]. It is suggested from experimental data that in the case of two fixed points close to the surface, high-frequency structures move with the mean wind velocity, and low-frequency structures move similar to a convective velocity [5]. A visual outcome of the low-

frequency structure effect may be observed in Figure 2, with an experiment involving buoyant thermals that rise from a heated surface [22].

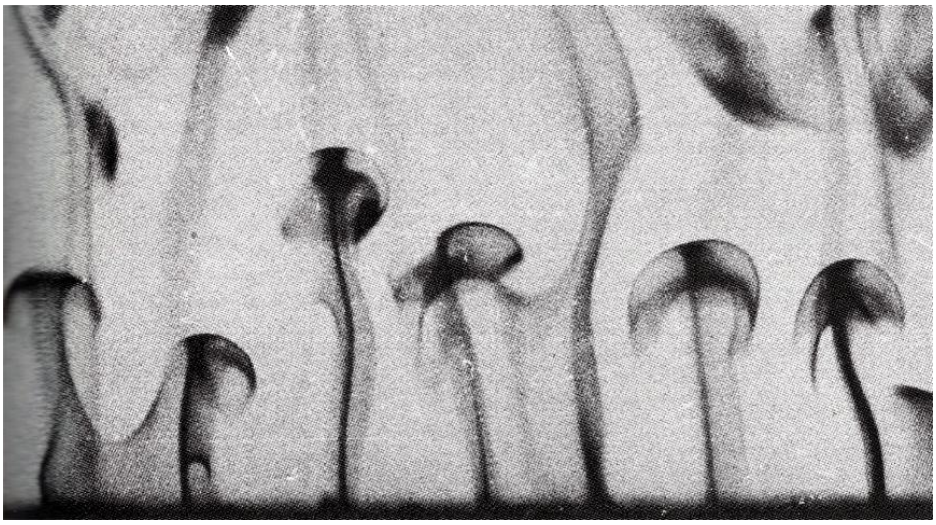

Figure 2: Low-frequency thermal plume structures rising from a heated surface.

Figure 3 depicts the cross section of a turbulent high-frequency structure under the exposure of wind. In this case, smoke in a wind tunnel is illuminated by laser light [22].

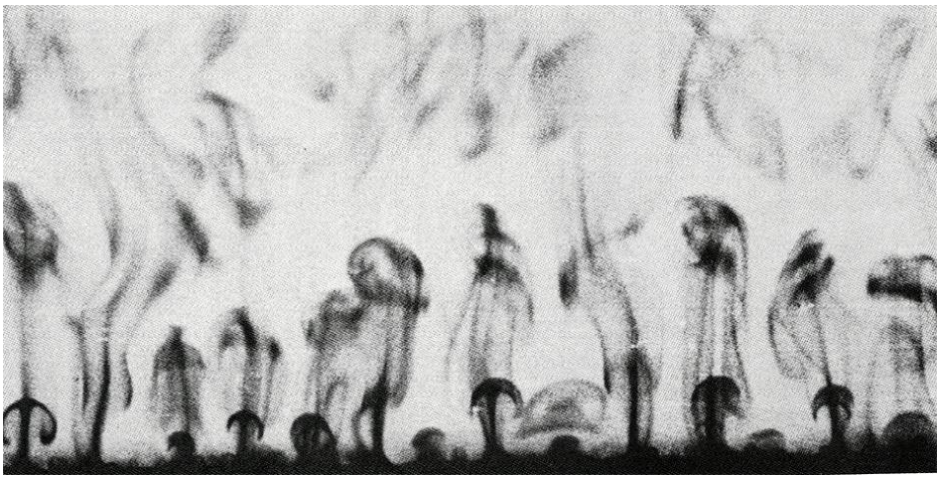

Figure 3: High-frequency thermal plume structures rising from a heated surface in turbulent conditions, caused by wind shear.

It is useful to model turbulence with parameters concerning the characteristics of its statistical nature. From a physical standpoint the refractive index structure parameter, C_n^2 (units of $m^{-2/3}$), is a measure of the strength of the fluctuations in the refractive index and therefore the magnitude of atmospheric turbulence [15]. It is directly related to the modulation transfer function (MTF) of the atmosphere, which is central to communication system investigation [14, 23]. The refractive index of air at optical wavelengths is known to follow the formula

$$n = 1 + 77.6\left[1 + \frac{7.52 \cdot 10^{-3}}{\lambda^3}\right]\frac{P}{T} \cdot 10^{-6}\,, \tag{2.9}$$

where λ is the wavelength of light in micrometers, P is the atmospheric pressure in millibars, and T is the atmospheric temperature in Kelvin [15].

When studying a randomly fluctuating refractive index, it is useful to model the index of refraction at a position $\boldsymbol{r}$ and time t as the sum of two parts,

$$n(\boldsymbol{r}, t) = n_0(\boldsymbol{r}, t) + n_1(\boldsymbol{r}, t), \tag{2.10}$$

where n_0 represents the deterministic, slowly changing contribution (such as variation with height above the ground), and n_1 represents the random fluctuations. In the case of atmospheric turbulence, n_1 is the term that the analysis center on. Structure functions may be utilized to properly describe the effects of atmospheric turbulence on optical wave propagation. The structure function of the index of refraction, $D_n(\boldsymbol{r})$, can be defined as

$$D_n(\boldsymbol{r}) \equiv \langle [n_1(\boldsymbol{r_1}, t) - n_1(\boldsymbol{r_2}, t)]^2 \rangle, \tag{2.11}$$

where the fluctuating parts of the refractive index are observed at positions $\boldsymbol{r_1}$ and $\boldsymbol{r_2}$, time t, and bracket notation $\langle \cdot \rangle$ represents the ensemble average [7, 15]. By use of dimension analysis,

Kolmogorov showed that the longitudinal structure function of wind velocity parallel to the vector $\boldsymbol{R}$ (connecting two observation points) in the inertial range satisfies the universal 2/3 power law and therefore can be modified to lead to the expression [7, 24]

$$D_n(\boldsymbol{r}) = \langle [n_1(\boldsymbol{r_1}, t) - n_1(\boldsymbol{r_2}, t)]^2 \rangle = \begin{cases} C_n^2 \boldsymbol{R}^{2/3} & l_0 \ll |\boldsymbol{R}| \ll L_0 \\ C_n^2 l_0^{-4/3} \boldsymbol{R}^2 & |\boldsymbol{R}| \ll l_0 \end{cases} \tag{2.12}$$

It is extremely difficult to predict the refractive index structure constant from Equation (2.12), a method based on the concept of temporal hour can approximately model C_n^2 utilizing macrometeorological parameters. This relationship is specified as

$$\begin{aligned} C_n^2 = {} & 3.8 \cdot 10^{-14} W_{TH} + 2 \cdot 10^{-15}\, T - 2.8 \cdot 10^{-15}\, RH + 2.9 \cdot 10^{-17}\, RH^2 \\ & - 1.1 \cdot 10^{-19}\, RH^3 - 2.5 \cdot 10^{-15}\, WS + 1.2 \cdot 10^{-15} WS^2 - 8.5 \\ & \cdot 10^{-17} WS^3 - 5.3 \cdot 10^{-13}, \end{aligned} \tag{2.13}$$

where W_{TH} is temporal hour weight, T is air temperature in units of Kelvin, RH is relative humidity as a percentage, and WS is wind speed in units of meters per second [6, 25]. It is important to note that this expression gives C_n^2 at a height of 15 meters, and therefore the Kopeika model must be scaled appropriately with height and time of day [25-27].

A simple model to scale C_n^2 between two near-ground heights h_0 and h_1 during daytime hours has been illustrated in literature to be

$$C_n^2(h_1) = C_n^2(h_0) \left(\frac{h_0}{h_1}\right)^{4/3}, \tag{2.14}$$

where the height $h_0 > h_1$. This height scaling model is only valid for ground-band measurements within the atmospheric surface layer [28]. It has been discovered a 2/3 power law may better describe behavior during evening hours, the relationship is given as

$$C_n^2(h_1) = C_n^2(h_0)\left(\frac{h_0}{h_1}\right)^{2/3}. \quad (2.15)$$

The change in power-law is postulated to be as such because the Earth's surface radiates the heat it absorbed during the daytime and becomes colder than the air (producing more stable conditions) [28, 29].

Typical values for C_n^2 are between $10^{-16}\ m^{-2/3}$ for weak fluctuations and $10^{-12}\ m^{-2/3}$ for strong fluctuations [30]. Figure 4 illustrates the behavior of C_n^2 throughout a typical day. The data were taken by the UCF WPRG team propagating a commercial scintillometer's beam over the 1km laser range at the Innovative Science and Technology Experimental Facility (ISTEF), located within the Kennedy Space Center, FL [26, 31]. When there is no sunshine, C_n^2 is low because there is no solar energy for the ground to absorb. As the sun begins to rise, C_n^2 increases until it reaches a maximum in the middle of the day indicating a maximum point of atmosphere induced turbulence. As the sun begins to set, C_n^2 decreases which indicates atmospheric turbulence is subsiding. An interesting trend to note on the plot is the sudden drop in C_n^2 before and after sunrise. These two dips are referred to in literature as the individual day's *quiescent periods* [28]. This drop in C_n^2 occurs due to the temperature gradient between the ground and atmosphere being minimal.

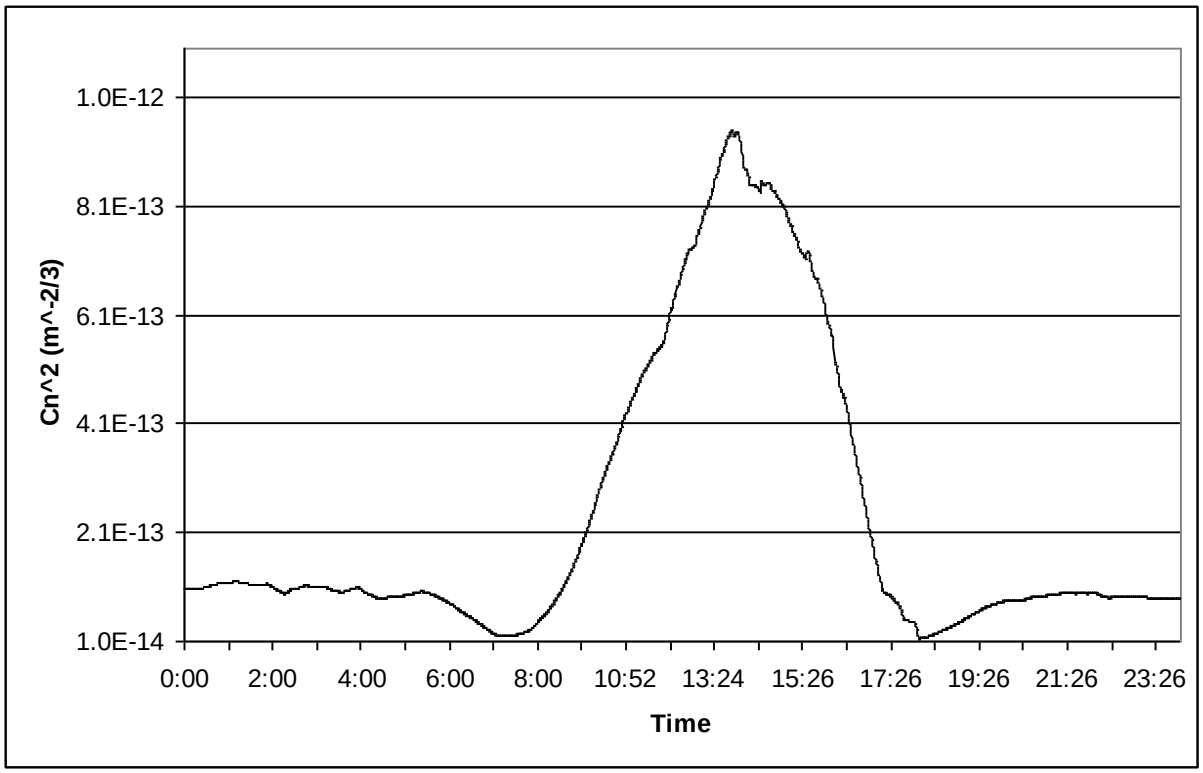

Figure 4: 24-hour C_n^2 profile of a typical summer day at the ISTEF laser range.

The atmosphere is thought to consist of a continuum of turbulent cells. The maximum size of which is usually on the order of one to one hundred meters, and is known as the outer scale of atmospheric turbulence L_0. These large cells act like weak positive lenses ($f \sim 1\text{km}$) and have a focusing effect on the propagating beam [7]. Due to inertial forces, these large cells will continually break up into smaller cells until reaching a minimum size on the order of millimeters, known as the inner scale of atmospheric turbulence l_0. These small cells act like negative lenses and cause the beam to diverge. The turbulent cells attenuate and redirect the energy of a propagating laser beam. The inner and outer scales of turbulence represent the range of scale sizes over which isotropic turbulence is formed [7].

Physically, the atmosphere can be visualized as a collection of randomly placed lenses diffracting and refracting the propagating light. A pictorial description of the process is shown in Figure 5 where it can be observed that the smallest of the turbulent cell sizes corresponds to the inner scale parameter l_0, and the largest of the cell sizes corresponds to the outer scale parameter L_0.

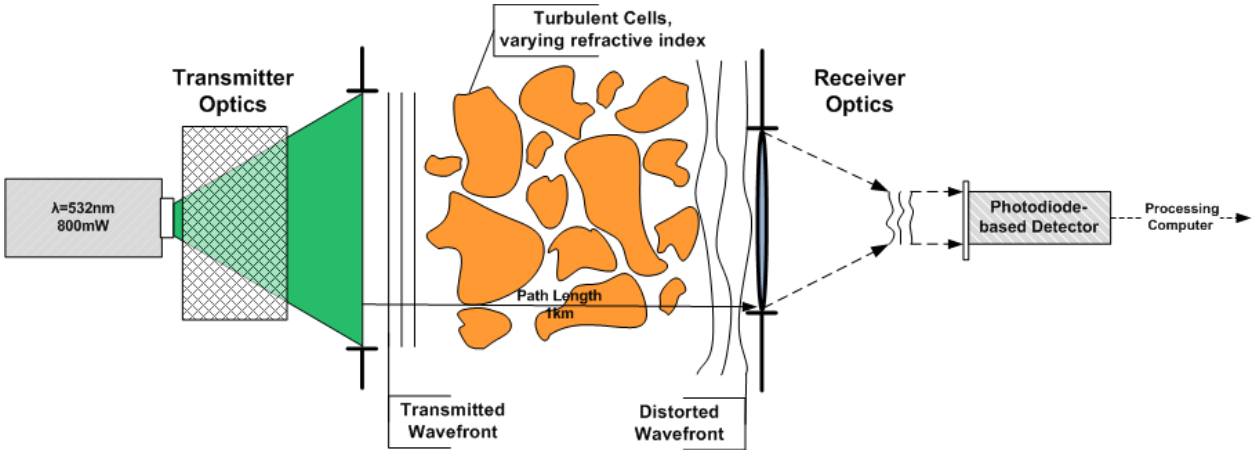

Figure 5: Laser beam propagation through atmospheric turbulence.

When discussing the effects that parameters such as C_n^2, l_0, and L_0 have on the channel behavior, and its implications on FSO communication system design, it is useful to develop tools for analysis of the irradiance signal detected by the receiver. The scintillation index describes the fluctuations of the received irradiance after propagating through the atmosphere. It is calculated through the normalized variance of the irradiance signal,

$$\sigma_I^2 = \frac{\langle I^2 \rangle}{\langle I \rangle^2} - 1, \tag{2.16}$$

where I is a signal that represents the irradiance of the optical wave and $\langle I^n \rangle$ denotes the n^{th} order ensemble average of the irradiance signal [7, 15]. A direct relationship between the magnitude of C_n^2, l_0, and L_0 can be demonstrated with the optical wave models described in

Section 2.1 Optical Wave Propagation [7]. There two major regimes of turbulence, each representing a degree of turbulence severity. Under the weak turbulence conditions the scintillation index is generally less than unity $\sigma_I^2 < 1$ [7, 10]. Weak turbulence implies a somewhat of a combination of a low C_n^2 value and/or small path length L. The irradiance fluctuations seen at the receiver are less severe and less detrimental to communication system operation [1, 7, 13]. As the scintillation index approaches unity, the statistics shift into a regime referenced as moderate to strong turbulence $\sigma_I^2 > 1$. Much of the developed theory is focused on the weak turbulence regime, however strong turbulence is based from the same principles [7, 10]. The strong turbulence regime implies a large irradiance signal variance, as well as a large C_n^2 and/or path length L.

2.4 Aperture Averaging

One other parameter that may be inferred from measurements of C_n^2 and l_0 is the correlation radius ρ_0 of the atmospheric turbulence [11, 32]. This parameter represents the 1/e point of the complex degree of coherence function (DOC) [7]. It provides a measure of the distance over which irradiance values will exhibit strong correlation. This analysis utilizes spherical wave theory, therefore the spherical wave spatial correlation radius is presented as [7]

$$\rho_{sp} = (0.55 C_n^2 k^2 L)^{-3/5}, \quad l_0 \ll \rho_{sp} \ll L_0, \tag{2.17}$$

where k is the wave number, L is the path length, and it is assumed that $L_0 = \infty$. Equation (2.17) effectively quantifies the amount of atmospheric turbulence induced by the channel with account of refractive-index structure constant and the inner-scale, but with the outer-scale dependence neglected.

A reduction in the fluctuations occurs as the radius of the receiving aperture is increased beyond the correlation radius ρ_0 of the atmospheric turbulence [11, 32]. The reduction is referred to as *aperture averaging* because the higher-frequency fluctuations are averaged (integrated), as would happen if a high-bandwidth signal is passed through a low-pass filter. As a general rule, aperture averaging effects are mostly present when the aperture diameter exceeds the spatial coherence length by three times or more ($D > 3\rho_{sp}$) [7, 13]. We will refer to this rule of thumb as the *aperture averaging criteria* in the proceeding analysis.

The scintillation index is also affected by both inner scale l_0 and outer scale L_0; these parameters also play an important role in aperture averaging [7, 33-35]. The inner scale effects are prominent in weak to moderate turbulence and cause an increase in scintillation index, while outer scale effects occur in strong turbulence and reduce the scintillation index [7]. Aperture averaging and its effects will be further investigated when experimental data is compared to the gamma-gamma model.

2.5 Optical Communication System Model

The main advantage of an optical communication system when compared to a radiofrequency communication system is the increase in channel capacity. Modern FSO systems operate on the order of gigabits per second, whereas RF systems operate on the order of megabits per second [7, 36]. If a portion of the transmitted signal cannot be detected by the receiver it will result in the loss of large amounts of data. The effect of such information losses must be mitigated or accounted for, however operation may be possible if a location sensitive approach is maintained [1]. A buffering scheme to queue important data may or may not be utilized when the received

signal fades below the detectable signal threshold. Additionally, in order to properly transmit information through the channel a time-synchronization must be maintained between transmitter and receiver [37]. If fades occur too frequently, time-synchronization will not be maintainable and neither will the communication link. It is therefore desirable to understand the statistics of fade time.

For a communication system to function properly, it must be able to transmit information across a *channel* in a reliable manner. The basic outline of a communication channel is demonstrated in Figure 6: Communication channel model [37]. Information must be formatted, modulated, and then transmitted across the channel. On the receiving end, the signal must be demodulated, detected, and a decision must then be made as to what the information content is. Noted in Figure 6 is the time-synchronization requirement, this must be maintained between the modulator at the *transmitter* and demodulator at the *receiver* to allow phase-alignment of bit-slots [36]. The analysis greatly centers on the channel portion of the communication system model, and the effect the channel has at the receiver.

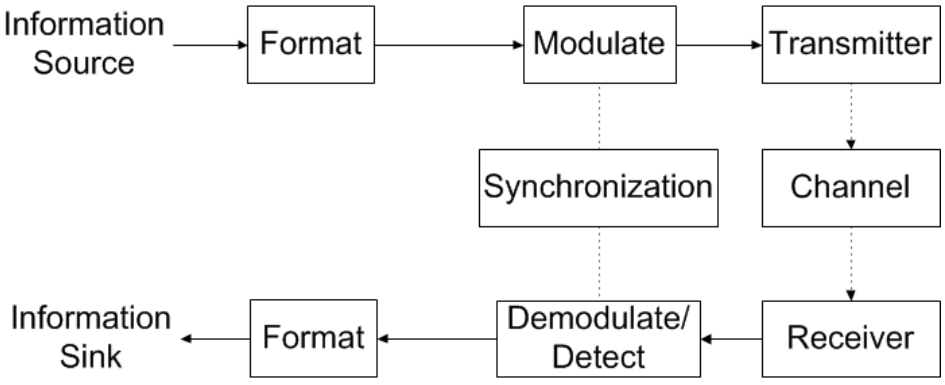

Figure 6: Communication channel model.

A key factor in free-space optical (FSO) communication systems is the communication link availability. To overcome noise sources within the system, transmission of data requires the signal level detected at the receiver to be above a specified level. The signal-to-noise ratio SNR can be related to probability of signaling error, and therefore plays a critical role in determining the amount of information that can be passed through the channel [36, 37]. In FSO communication system design, it is useful to define an irradiance threshold level I_T at which irradiance received by the detector I must exceed to successfully operate at a specified data rate [1, 7, 10, 13, 34]. We will initially define our link availability as the percentage of time that which the received irradiance I is greater than the minimum detectable threshold irradiance I_T, or $I \geq I_T$. If the received irradiance signal is below irradiance threshold, it is said to be *faded*. It is helpful to define the *probability of fade* as the integral relation

$$\Pr(I \leq I_T) = \int_0^{I_T} p(I)dI, \tag{2.18}$$

where $p(I)$ is the irradiance signal probability density function.

We are not only interested in the average amount of time the received irradiance signal fades, but also the variance in irradiance signal fade times. Average of received irradiance fade time has been approached for a number of channel models, therefore theory to analyze such scenarios is available [38-41].Variance in received irradiance signal fade time is somewhat less developed in FSO system analysis; although theory exists that facilitates analysis [7, 13, 38, 39]. The focus will be variance of fade time as it will provide insight as to how to predict the distribution fade times. The analysis is deemed useful and important to FSO communication system theory

because it provides upper and lower bounds to the fade time distribution based upon measurable atmospheric parameters [10].

The fade statistics of the received signal are practical in determining the channel's implications on a FSO communication system's SNR. Even if the transmitting system provides the required operable SNR at the receiver, fading induced by the atmospheric propagation channel on the received signal can cause the SNR to become temporarily deprecate. For example, suppose an optical communication link is operating at 10Gbit per second. If during a period of one second the channel were faded below the minimum detectable threshold for a time of 20 milliseconds, then, in the best scenario, the system would only be able to deliver 9.8Gbit of data during that particular second. This assumes that the optical channel is able to maintain time synchronization the entire time it is transmitting [1]. This problem evolves further when considering the fact that the transmitter/receiver will require time to resynchronize if the synchronization is lost. Frequency of fades (or inter-fade period) will then play an important role; the synchronization problem will not be addressed in this analysis. Instead, channel model characteristics will be developed.

Namely, the average amount of time and the variance in amount of time a received irradiance signal falls below (and stays below) the specified threshold irradiance. The amount of time an irradiance signal falls below the specified irradiance threshold level will be referred to hereto as *irradiance fade time*. The notion of irradiance fade time is demonstrated in Figure 7: Single incidence of a fade below a specified irradiance threshold (-5dB below the mean), with a half-

second sample of received irradiance data. If one looks at a distribution of irradiance signal fade times, then the attention will be on two major characteristics: average and variance of irradiance fade times. For this reason, the same data is shown in Figure 8 but with the ensemble of fade times marked for viewing ease. As can be observed, the fade times are not all the same. Some fades are shorter in duration, and some fades are longer in duration. The goal of this analysis is to not only quantify the average value of fade time, but also the variance in fade time.

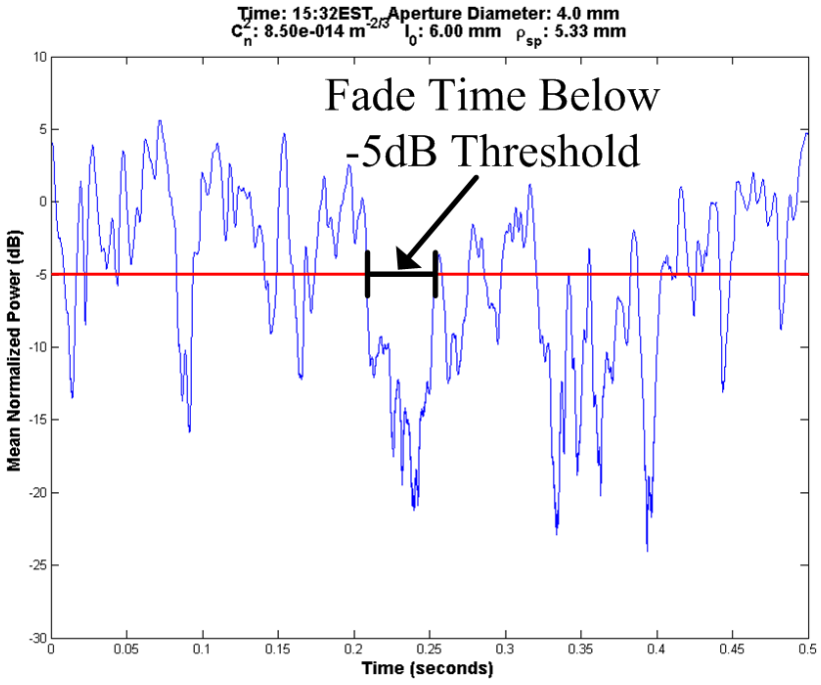

Figure 7: Single incidence of a fade below a specified irradiance threshold (5dB below the mean).

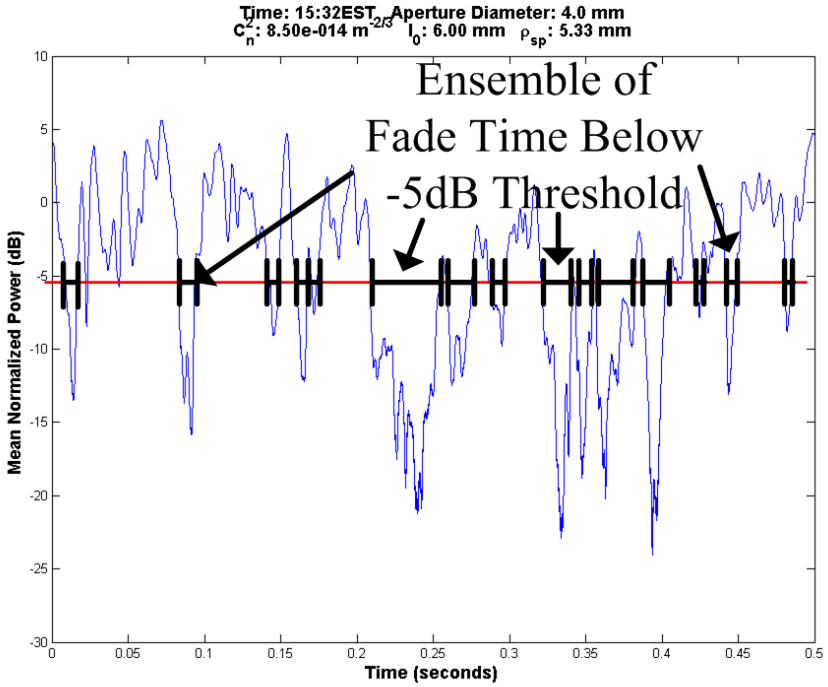

Figure 8: Ensemble of fades below a specified irradiance threshold (5dB below the mean).

Data cannot be transmitted when a fade occurs, and must then be buffered during fade periods. If the buffer size is based solely on the amount of data that would be withheld due to mean fade time, it may not adequately compensate for the longer fade times the system would experience due to the variance in fade time. Mean irradiance fade time models for FSO systems have been previously derived and analyzed [10, 38-41]. A lesser used metric of irradiance threshold level crossing statistics is the variance (or the more readily applicable standard deviation) in threshold level crossing time. The variance in fade time represents a measure of the fade distribution, as the mean fade time only provides an indication about which fade time value the fade time distribution is centered about. As a postulation, one could predict the fade distribution to be somewhat Gaussian (normal) in nature. We will define mean fade time (as a function of threshold irradiance) with the symbol $\langle t(I_T) \rangle$. Variance in fade time will then depend on the

mean square fade time as $VAR[t(I_T)] = \langle t^2(I_T)\rangle - \langle t(I_T)\rangle^2$, with the standard deviation in fade time being the square root of the variance expression[12, 13, 42].

If the fade distribution is Gaussian in behavior, it would imply roughly $\sim 99\%$ of the fade times would lay within three standard deviations of the mean fade time. This would imply that a larger buffer size would be needed to compensate for the communication channel. A channel model that incorporates a consideration of variance in fade time would also alleviate an additional concern. Optical systems operate at such a large data rates (implying large clock rates) and the fade times occur on scales many orders of magnitude larger than the clock rate ($\sim 10^3 - 10^6$).

The proceeding study will be used to determine an appropriate method to find the variance in fade time of an optical communication link. It is crucial to choose an appropriate channel model to evaluate the reliability of a communication channel. For this analysis, the gamma-gamma irradiance probability density function model will be utilized to evaluate channel conditions.

3. IRRADIANCE FADING OF COMMUNICATIONS CHANNEL

3.1 Probability Density Function (PDF) Models

3.1.1 Gamma Distribution

It is stated that a random variable X is gamma distributed if its probability density function (PDF) follows the form

$$p_X(X) = \frac{\alpha}{\langle X \rangle \Gamma(\alpha)} \left(\frac{\alpha X}{\langle X \rangle} \right)^{\alpha - 1} \exp\left(-\frac{\alpha X}{\langle X \rangle} \right), \quad \alpha > 0, X > 0. \tag{3.1}$$

where α represents the gamma model parameter, $\langle X \rangle$ denotes the average value of the random variable X, and $\Gamma(\cdot)$ denotes the gamma function. The gamma process is said to be unimodal with a mode at $\alpha - 1$ when $\alpha \geq 1$, and when $\alpha < 1$ it is a monotone function that approaches infinity as the α parameter approaches zero [43]. We will utilize this model as a modulation process between a pair of gamma distributed random variables to yield the gamma-gamma distribution. It is useful to note that the gamma model can be useful in scenarios where aperture averaging imparts a significant impact on the PDF [7, 13]. This concept will be briefly mentioned in the analysis, however not utilized in detail.

3.1.2 Gamma-Gamma Distribution

From the modified Rytov theory for moderate to strong fluctuations, the distinct large scale and small scale effects on the scintillation lead to the assumption that the atmosphere perturbed irradiance of an optical wave can be expressed as a modulation of the statistically independent large scale fluctuations and the small scale fluctuations [7]. Let irradiance be represented as a function of time $I(t)$, as well as the large time scale fluctuations $X(t)$ and the small time scale

fluctuations $Y(t)$. The received irradiance will be a modulation (product) of the large and small scale fluctuations, namely

$$I(t) = X(t)Y(t). \tag{3.2}$$

It is taken that the large and small scale fluctuations are normalized such that $\langle X(t)\rangle = 1$, and $\langle Y(t)\rangle = 1$. The second moment of the normalized intensity is

$$\langle I^2(t)\rangle = \langle X(t)^2\rangle\langle Y(t)^2\rangle = (1+\sigma_x^2)\big(1+\sigma_y^2\big), \tag{3.3}$$

where σ_x^2 and σ_y^2 are the large scale and small scale normalized variances (scintillation indices), respectively [7].

$$I(t) = X(t)Y(t) \tag{3.4}$$

For the moment, let us consider a stationary process to reduce the notation by removing the dependence on the time variable t. The random variables X and Y are explicitly restated in terms of the irradiance

$$I = XY. \tag{3.5}$$

With each fluctuation process assumed to be gamma distributed, we will denote the density distribution function for the large scale process as

$$p_X(X) = \frac{\alpha}{\langle X\rangle\Gamma(\alpha)}\left(\frac{\alpha X}{\langle X\rangle}\right)^{\alpha-1}\exp\left(-\frac{\alpha X}{\langle X\rangle}\right), \quad \alpha > 0, X > 0, \tag{3.6}$$

and the density distribution function for the small scale process as

$$p_Y(Y) = \frac{\beta}{\langle Y\rangle\Gamma(\beta)}\left(\frac{\beta Y}{\langle Y\rangle}\right)^{\beta-1}\exp\left(-\frac{\beta Y}{\langle Y\rangle}\right), \quad \beta > 0, Y > 0, \tag{3.7}$$

where $\Gamma(\gamma)$ is the gamma function, $K_p(\gamma)$ is the modified Bessel function of the second kind, α and β are the Gamma-Gamma PDF parameters which represent the effective numbers of large scale and small scale scatterers, respectively.

We attempt to determine a conditional PDF for the irradiance by replacing the small scale variable with its relationship to the large scale variable, namely $Y = I/X$. Since the small and large scale fluctuations are statistically independent, one may write

$$p_I(I|X) = \frac{\beta(\beta I/X)^{\beta-1}}{\mathrm{X}\,\Gamma(\beta)} \exp(-\beta I/X), \quad \beta > 0, Y > 0, \tag{3.8}$$

and the intensity density function may be determined by marginalizing out the large scale variable X,

$$p_I(I) = \int_0^\infty p_I(I|X)\, p_X(X)\, dX = \int_0^\infty p_Y(Y) \left.\frac{dY}{dI}\right|_{Y=\frac{I}{X}} p_X(X)\, dX. \tag{3.9}$$

The first part is readily found to be

$$p_Y(Y) \left.\frac{dY}{dI}\right|_{Y=\frac{I}{X}} = \frac{\beta}{\langle Y\rangle \Gamma(\beta) X} \left(\frac{\beta I}{\langle Y\rangle X}\right)^{\beta-1} e^{-\beta I/\langle Y\rangle X}, \quad I > 0. \tag{3.10}$$

The PDF of a gamma-gamma distributed irradiance can then be written as

$$p_I(I) = \int_0^\infty p_I(I|X)\, p_X(X)\, dX = \int_0^\infty p_Y(Y) \left.\frac{dY}{dI}\right|_{Y=\frac{I}{X}} p_X(X)\, dX \tag{3.11}$$

$$= \frac{\beta}{\langle Y\rangle \Gamma(\beta)} \left(\frac{\beta I}{\langle Y\rangle}\right)^{\beta-1} \frac{\alpha}{\langle X\rangle \Gamma(\alpha)} \left(\frac{\alpha}{\langle X\rangle}\right)^{\alpha-1}$$

$$\times \int_0^\infty X^{\alpha-\beta-1} \exp\left(-\frac{\beta I}{\langle Y\rangle X} + \frac{\alpha X}{\langle X\rangle}\right) dX.$$

Using the variable transformation $z = \alpha X/\langle X\rangle$ leads to

$$p_I(I) = \frac{\alpha\beta}{\langle X\rangle\langle Y\rangle\Gamma(\alpha)\Gamma(\beta)}\left(\frac{\alpha\beta I}{\langle X\rangle\langle Y\rangle}\right)^{\beta-1} \times \int_0^\infty z^{\alpha-\beta-1}\exp\left(-z+\frac{\alpha\beta I}{\langle X\rangle\langle Y\rangle z}\right)dz \tag{3.12}$$

$$= \frac{1}{\Gamma(\alpha)\Gamma(\beta)I}\left(\frac{\alpha\beta I}{\langle I\rangle}\right)^{\beta}\int_0^\infty z^{\alpha-\beta-1}\exp\left(-z+\frac{\alpha\beta I}{\langle I\rangle z}\right)dz,$$

where $\langle I\rangle = \langle X\rangle\langle Y\rangle$ has been utilized for simplification. The integration in the previous step can be evaluated. Assuming substitutions of the form $p = \beta - \alpha$ and $\gamma = 2(\alpha\beta I/\langle I\rangle)^{1/2}$ with note of the integral relation for the modified Bessel function of the second kind [44],

$$K_p(\gamma) = \frac{1}{2}\left(\frac{\gamma}{2}\right)^p \int_0^\infty e^{-\left(z+\frac{\gamma^2}{4z}\right)} z^{-(p+1)}dz, \tag{3.13}$$

leads to the result

$$p_I(I) = \frac{1}{\Gamma(\alpha)\Gamma(\beta)I}\left(\frac{\alpha\beta I}{\langle I\rangle}\right)^{\beta} 2\left(\frac{\alpha\beta I}{\langle I\rangle}\right)^{(\alpha+\beta)/2} K_{\beta-\alpha}\left(2\sqrt{\frac{\alpha\beta I}{\langle I\rangle}}\right) \tag{3.14}$$

$$= \frac{2}{\Gamma(\alpha)\Gamma(\beta)I}\left(\frac{\alpha\beta I}{\langle I\rangle}\right)^{(\alpha+\beta)/2} K_{\beta-\alpha}\left(2\sqrt{\frac{\alpha\beta I}{\langle I\rangle}}\right).$$

This equation can be again rewritten (for simplicity) by applying the property of the modified Bessel function, $K_{-p}(\gamma) = K_p(\gamma)$, leading to the gamma-gamma distributed irradiance PDF

$$p_I(I) = \frac{2}{\Gamma(\alpha)\Gamma(\beta)I}\left(\frac{\alpha\beta I}{\langle I\rangle}\right)^{(\alpha+\beta)/2} K_{\alpha-\beta}\left(2\sqrt{\frac{\alpha\beta I}{\langle I\rangle}}\right), \quad I > 0. \tag{3.15}$$

For the case of normalized irradiance ($\langle I\rangle = 1$) the gamma-gamma distributed irradiance PDF is then given as

$$p_I(I) = \frac{2(\alpha\beta)^{(\alpha+\beta)/2}}{\Gamma(\alpha)\Gamma(\beta)} I^{(\alpha+\beta)/2\,-1} K_{\alpha-\beta}(2\sqrt{\alpha\beta I}), \quad I > 0. \tag{3.16}$$

The large scale scattering parameter α and the small scale scattering parameter β may be related to the scintillation index by calculating the second moment of the gamma-gamma distributed irradiance,

$$\langle I^2 \rangle = \int_{-\infty}^{\infty} I^2 p_I(I)\, dI \tag{3.17}$$

$$= \frac{2}{\Gamma(\alpha)\Gamma(\beta)} \left(\frac{\alpha\beta}{\langle I \rangle}\right)^{(\alpha+\beta)/2} \int_0^{\infty} I^{\frac{(\alpha+\beta)}{2}+1} K_{\alpha-\beta}\left(2\sqrt{\frac{\alpha\beta I}{\langle I \rangle}}\right) dI.$$

Using again the following integral relation in Equation (3.13) leads to

$$\langle I^2 \rangle = \frac{1}{\Gamma(\alpha)\Gamma(\beta)} \left(\frac{\alpha\beta}{\langle I \rangle}\right)^{\alpha} \int_0^{\infty} I^{\alpha+1} \int_0^{\infty} \exp\left(-z - \frac{\alpha\beta I}{\langle I \rangle z}\right) z^{-(\alpha-\beta+1)} dz\, dI. \tag{3.18}$$

Changing the order of integration, making the substitution of variables $Y = \alpha\beta I/\langle I \rangle z$ in the integration over I and using the integral definition of the gamma function on both integrals yield [7, 12, 42]

$$\langle I^2 \rangle = \left(\frac{\alpha\beta}{\langle I \rangle}\right)^{-2} \frac{\Gamma(\alpha+2)\Gamma(\beta+2)}{\Gamma(\alpha)\Gamma(\beta)} \tag{3.19}$$

$$= \langle I \rangle^2 \left(1 + \frac{1}{\alpha}\right)\left(1 + \frac{1}{\beta}\right).$$

This may then be related to the scintillation index by the definition,

$$\sigma_I^2 = \frac{\langle I^2 \rangle}{\langle I \rangle^2} - 1 = \left(1 + \frac{1}{\alpha}\right)\left(1 + \frac{1}{\beta}\right) - 1. \tag{3.20}$$

From the modified Rytov theory for moderate to strong fluctuations

$$\langle I^2 \rangle = \langle X^2 \rangle \langle Y^2 \rangle = (1 + \sigma_X^2)(1 + \sigma_Y^2). \tag{3.21}$$

The large-scale and small-scale gamma-gamma scattering parameters may also be separated and written in terms of separate scintillation index contributions,

$$\alpha = \frac{1}{\sigma_X^2}, \tag{3.22}$$

$$\beta = \frac{1}{\sigma_Y^2}, \tag{3.23}$$

where σ_X^2 is the large-scale irradiance scintillation index contribution and σ_Y^2 is the small-scale irradiance scintillation index contribution.

A hint of what is referred to as *aperture averaging* is present within the gamma-gamma model parameters α and β. The gamma-gamma scattering parameter α relates to what would typically be the largest of turbulent scale sizes. This parameter mainly relates to the physical parameters: outer-scale L_0, refractive-index structure parameter C_n^2, and demonstrates a lesser dependence on inner-scale l_0. The small-scale scattering parameter β relates to what would be the scale sizes related to the physical parameters l_0 and C_n^2. Apertures will integrate over a larger number of small-scale scatterers than large-scale scatterers ($\beta > \alpha$). As aperture diameter D increases, we will typically expect the number of small-scale scattered β observed by the receiver aperture to increase. From Equation (3.23) we can expect an increase in β to decrease the small-scale scintillation index contribution σ_Y^2 [7, 13, 24, 27, 29]. Similarly, an increase in aperture diameter D will increase the number of observed large-scale scatterers α. However, the observed number of large-scale scatterers α will not grow as rapidly as the number of small-scale scatterers β observed by the aperture because of the scale size difference ($\beta/\alpha \sim 10$). Also note

that in some cases these parameters can also be approximately the same value [7, 13, 26, 29, 31, 33-35, 45].

Occasionally it is useful to define the log irradiance scintillation index in terms of the natural logarithm with the expression [7, 13]

$$\sigma_{\ln I}^2 = \ln(\sigma_I^2 + 1). \tag{3.24}$$

Also useful in the analysis is to note that a closed form solution for the cumulative distribution function (CDF) of a gamma-gamma distributed irradiance has been developed. This expression is equivalent to probability of fade and presented in terms of the hyper-geometric function ${}_1F_2(\cdot)$ as

$$P(I \le I_T) = \int_0^{I_T} p(I)dI \tag{3.25}$$

$$= \frac{\pi}{\sin[\pi(\alpha-\beta)]\,\Gamma(\alpha)\Gamma(\beta)}$$

$$\times \left\{ \frac{(\alpha\beta I_T)^\beta}{\beta\Gamma(\beta-\alpha+1)}\ {}_1F_2(\beta;\beta+1,\beta-\alpha+1;\alpha\beta I_T) \right\}$$

$$\times \left\{ \frac{(\alpha\beta I_0)^\alpha}{\alpha\Gamma(\alpha-\beta+1)}\ {}_1F_2(\alpha;\alpha+1,\alpha-\beta+1;\alpha\beta I_T) \right\},$$

with I_T representing the irradiance threshold level. The presented gamma-gamma model expressions will be utilized to develop gamma-gamma model fade statistic expressions and compare the results with experiment data.

3.2 Level-Crossing Statistics of an Irradiance Signal

3.2.1 Mean Level Crossing Rate

It has been demonstrated that characterization of signal level crossings moments may be derived with knowledge of the derivative joint density functions. This is done by examining a functional representation of the j^{th} ensemble realization of a random process $I^{(j)}(t)$ at an arbitrary intensity level I_T in the time interval (t_1, t_2). Analysis will be limited to stationary random processes and each ensemble realization will be considered representative of the entire ensemble [46]. A counting function is introduced for crossings at the level I_T via the following discussion [38, 39]. It is observed that the process $I(t)$ must be differentiable (mean square) to the first order, at least [38, 39].

We begin the analysis with having $u(t)$ represent the Heaviside step function defined by

$$u(t) = \begin{cases} 0, & t < 0 \\ 1/2, & t = 0 \\ 1, & t > 0. \end{cases} \tag{3.26}$$

Then considering $u\left[I^{(j)}(t) - I_T\right]$, and taking the derivative gives

$$\frac{du}{dt} = \dot{I}^{(j)}(t)\, \delta\left(I^{(j)}(t) - I_T\right), \tag{3.27}$$

where $\delta\left(I^{(j)}(t) - I_T\right)$ is the Dirac delta function. The Dirac delta function is commonly defined as

$$\delta(t) = \begin{cases} \infty, & t = 0 \\ 0, & t \neq 0, \end{cases} \tag{3.28}$$

and also satisfies the identity

$$\int_{-\infty}^{\infty} \delta(t)\, dt = 1. \tag{3.29}$$

Due to the Dirac delta function, the expression in Equation (3.27) vanishes except if the irradiance $I^{(j)}(t)$ is equal to the threshold irradiance I_T. When $I^{(j)}(t) = I_T$ a spike occurs (of unit area) directed positively or negatively depending on whether the sign of $\dot{I}^{(j)}(t)$ at I_T is positive or negative. The desired counting functional for the j^{th} member of the ensemble is then the number of crossings per second (at time t), and may be written [39]

$$n^{(j)}\left(I_T, \dot{I}; t\right) = \left|\dot{I}^{(j)}(t)\right| \delta\left(I^{(j)}(t) - I_T\right) \quad -\infty < I^{(j)} < \infty\,. \tag{3.30}$$

The total number of crossings in an interval $t_2 - t_1$ is written as the integral relationship

$$N^{(j)}\left(I_T, \dot{I}; t_2 - t_1\right) = \int_{t_1}^{t_2} n^{(j)}\left(I_T, \dot{I}; \tau\right) d\tau = \int_{t_1}^{t_2} \left|\dot{I}^{(j)}(\tau)\right| \delta\left(I^{(j)}(\tau) - I_T\right) d\tau. \tag{3.31}$$

Setting $I_T = \langle I \rangle$ gives the expected number of mean irradiance-level crossings in the interval, however I_T is left as an arbitrarily defined irradiance level. It is compared in ratio to the mean irradiance value in the experimental analysis.

First and higher-order moments for $n\left(I_T, \dot{I}; t\right)$ and $N\left(I_T, \dot{I}; t_2 - t_1\right)$ can be obtained from Middleton's discussions [38, 39]. By assuming a stationary random process, we may simplify notation by dropping dependence on the j^{th} member of the ensemble and consider each realization of the process to be equivalent. The mean number of level crossings is given to be

$$\overline{n\left(I_T, \dot{I}; t\right)} = \iint_{-\infty}^{\infty} \left|\dot{I}(t)\right| \delta(I(t) - I_T) p_1(I_T, \dot{I}, t)\, dt\, d\dot{I}, \tag{3.32}$$

where $p_1(I_T, \dot{I}, t)$ is the joint density of the irradiance signal at the irradiance threshold level I_T and the derivative of irradiance $\dot{I}$ at time t. Following through with the inside integration involving the time variable t, the expression in Equation (3.32) for the mean number of level crossings can be rewritten as

$$\overline{n(I_T, \dot{I}; t)} = \int_{-\infty}^{\infty} |\dot{I}(t)|\, p_1(I_T, \dot{I}, t)\, d\dot{I}. \tag{3.33}$$

The dependence of the developed statistical parameters on time t may be omitted if a stationary random process is considered [46]; this will be assumed to be true for the presented analysis in Section 4.4.2 Mean Number of Level Crossings of Experimental Data and Section 4.4.3 Mean Fade Time of Experimental Data.

The expected number of irradiance signal fades $\langle n(I_T, \dot{I}; t) \rangle$ is then found to be one half of the expected number of irradiance threshold level crossings $\overline{n(I_T, \dot{I}; t)}$, explicitly stated as [13]

$$\langle n(I_T, \dot{I}; t) \rangle = \frac{1}{2} \int_{-\infty}^{\infty} |\dot{I}(t)|\, p_1(I_T, \dot{I}; t)\, d\dot{I} = \frac{1}{2} \overline{n(I_T, \dot{I}; t)}. \tag{3.34}$$

We note the subtle difference in notation between the expected number of irradiance signal fades and the expected number of threshold level crossings. Additionally, the dependence on the time variable t may be dropped from notation if a stationary random process is assumed.

For simplicity in notation, we will notate the level crossing statistics only as a function irradiance threshold level

$$\langle n(I_T) \rangle \equiv \frac{1}{2} \overline{n(I_T)}, \tag{3.35}$$

with the time dependence considered inherent.

3.2.2 Mean Square Level Crossing Rate

Similar in statistical concept to the mean level crossing rate, the mean square level crossing rate shares some characteristics of the former. It is demonstrated that a simplified approach can be taken to obtain an estimate of the second moments of the level crossing distribution $\overline{n^2}$, $\overline{N^2}$ from expressions

$$\overline{n^2} = \iint_{-\infty}^{\infty} |\dot{I}_1|\,|\dot{I}_2|\, p_2(I_T, \dot{I}_1, t_1; I_T, \dot{I}_2, t_2)\, d\dot{I}_1 d\dot{I}_2, \tag{3.36}$$

where $p_2(I_T, \dot{I}_1, t_1; I_T, \dot{I}_2, t_2)$ is the joint density of irradiance at threshold level I_T and the derivative of the irradiance $\dot{I}$ at two moments in time t_1 and t_2. From this, the expected number of level crossings within the time interval $t = t_2 - t_1$ is

$$\overline{N^2} = \iint_{t_1}^{t_2} \overline{n^2(I_T, \dot{I}_1, \dot{I}_2; \tau_1, \tau_2)}\, d\tau_1 d\tau_2. \tag{3.37}$$

Once again, to clarify notation in Equation (3.36), the mean square irradiance threshold level crossing rate may be defined in terms expected value notation as

$$\langle n(I_T, \dot{I}_1; t_1) n(I_T, \dot{I}_2; t_2)\rangle \equiv \overline{n^2(I_T, \dot{I}_1, \dot{I}_2; t_1, t_2)}, \tag{3.38}$$

where $n(I_T, \dot{I}_n; t_n)$ represents the expected irradiance threshold level crossing rate at time t_n as defined in Equation (3.33). As previously stated, the dependence on the time variable t may be dropped from notation if a stationary random process is assumed. This assumption will be

prevalent in the proceeding analysis. We will then use the notation for the mean square irradiance threshold level crossing rate

$$\langle n(I_T)n(I_T)\rangle \equiv \overline{n^2(I_T)}. \tag{3.39}$$

For this analysis, the approach to find a closed form expression (or rather, an approximation to one) for $p_2\left(I_T, \dot{I}_1, t_1 \middle| I_T, \dot{I}_2, t_2\right)$ is as follows. Suppose the joint density at two moments in time t_1 and t_2 is written in terms of the conditional density distribution as

$$p_2\left(I_T, \dot{I}_1, t_1; I_T, \dot{I}_2, t_2\right) = p_1\left(I_T, \dot{I}_1, t_1\right) p_2\left(I_T, \dot{I}_1, t_1 \middle| I_T, \dot{I}_2, t_2\right). \tag{3.40}$$

If considering two instances that largely separated in time, the conditional density distribution may written [39]

$$\lim_{t_2 - t_1 \to \infty} p_2\left(I_T, \dot{I}_1, t_1 \middle| I_T, \dot{I}_2, t_2\right) = p_1\left(I_T, \dot{I}_2, t_2\right). \tag{3.41}$$

It is then inferred that

$$\lim_{t_2 - t_1 \to \infty} p_2\left(I_T, \dot{I}_1, t_1; I_T, \dot{I}_2, t_2\right) = p_1\left(I_T, \dot{I}_1, t_1\right) p_1\left(I_T, \dot{I}_2, t_2\right). \tag{3.42}$$

Equation (3.41) states that there is no memory or statistical dependence of the random process observed at two different times sufficiently separated in time. It is also known that correlation will approach zero for any natural phenomena as time difference approaches a large value [40, 46]. Generally the time correlations of irradiance fluctuations are not independent within 50 millisecond timescales [4, 5, 7, 13]. However, it is reasonably that there would likely be no correlation on minute time scales. This approximation is deemed appropriate for this analysis as atmospheric parameters are generally considered to be stationary over long periods of time (on order of a half an hour) [4, 5]. As a side note, if one were to consider two points separated an

infinitesimal small distance in time then we would have $\lim_{t_2-t_1\to 0} p_2(I_T, \dot{I}_1, t_1 | I_T, \dot{I}_2, t_2) = \delta(I_2 - I_1)$.

From this notion, the joint density of a finite set of n independently distributed joint density functions can then be written as

$$p_n(I_T, \dot{I}_1, t_1; I_T, \dot{I}_2, t_2; \dots; I_T, \dot{I}_n, t_n) = \prod_{\acute{n}=1}^{n} p_1(I_T, \dot{I}_{\acute{n}}, t_{\acute{n}}). \qquad (3.43)$$

Assuming the time t_{n+1} occurs much later than the time t_n, successive derivative joint density functions may be considered independently distributed [38, 39]. From this the sought joint density may be written as the multiplication of the derivative joint density function at two separate instances in time

$$p_2(I_T, \dot{I}_1, t_1; I_T, \dot{I}_2, t_2) = p_1(I_T, \dot{I}_1, t_1) p_1(I_T, \dot{I}_2, t_2). \qquad (3.44)$$

With expression (3.44) it is then possible to find the value of mean square irradiance threshold level crossing of the received irradiance signal from Equation (3.36). It is the joint density distribution of I and $\dot{I}$ that is needed at one or more instants $(t_1, t_2, \dots, t_m)$ for calculation of $\overline{n^m}$ and $\overline{N^m}$, where m represents the order of the desired statistical level crossing moment.

3.2.3 Fade Time Statistics

The average time (in seconds) which the received irradiance signal I stays below a specified irradiance level I_T is found with knowledge of the expected number of fades $\langle n(I_T) \rangle$ and the probability of fade $\Pr(I \leq I_T)$. Probability of fade was previously defined in Section 2.5 Optical Communication System Model as

$$\Pr(I \leq I_T) = \int_0^{I_T} p(I)dI, \tag{3.45}$$

where $p(I)$ is the probability density of irradiance I.

With expressions for probability of fade and expected number of fades, the expected fade time is the ratio of these two calculations. Explicitly stated as [10, 11, 13]

$$\langle t(I_T)\rangle = \frac{\Pr(I \leq I_T)}{\langle n(I_T)\rangle}, \tag{3.46}$$

where $\Pr(I \leq I_T)$ represents the probability that the irradiance $I(t)$ falls below the irradiance threshold level I_T and $\langle n(I_T)\rangle$ is the expected number of fades per second.

Higher order moments such as the mean square fade time $\langle t^2(I_T)\rangle$ (units of seconds squared) of irradiance signal $I(t)$ below the irradiance threshold level I_T may be concurrently developed by Equation (3.46). To find the mean square fade time, we consider taking the square root of second moment of level crossings $\langle n^2(I_T)\rangle$ to proceed with the analysis and maintain consistent units. From here, we proceed as with mean fade time

$$\sqrt{\langle t^2(I_T)\rangle} = \frac{\Pr(I \leq I_T)}{\sqrt{\langle n^2(I_T)\rangle}}, \tag{3.47}$$

and we must square the result shown in Equation (3.47) to reach the desired expression for mean square fade time $\langle t^2(I_T)\rangle$. Similarly, higher order moments can be obtained through use of this method as units will maintain the desired consistency. For this analysis, the probability of fade $\Pr(I \leq I_T)$ will be computed numerically through experimental data by the cumulative distribution function (CDF). This will allow numerical data to maintain tractable in the analysis.

With the expressions for mean fade time and mean square fade time, variance of fade time and standard deviation of fade time may then be readily found. As with regular statistical moments, the variance in fade time may be expressed in terms of the mean fade time $\langle t(I_T)\rangle$ and mean square fade time $\langle t^2(I_T)\rangle$ as

$$VAR[t(I_T)] = \langle t^2(I_T)\rangle - \langle t(I_T)\rangle^2, \tag{3.48}$$

and this again has units of seconds to the square power. In addition, the standard deviation in fade time may be found by taking the square root of Equation (3.48) and readily stated

$$StDEV[t(I_T)] = (VAR[t(I_T)])^{1/2}. \tag{3.49}$$

Standard deviation of fade time has the same units as the average value, seconds.

3.3 Joint Density of a Random Variable and its Temporal Derivative

Calculation of the expressions presented in Section 3.2 Level-Crossing Statistics of an Irradiance Signal requires formulation of joint density functions involving the irradiance and the derivative of irradiance term. The joint PDF of the irradiance and its time derivative for any irradiance distribution may be written as [7, 12, 13, 39, 42]

$$p_1(I, \dot{I}, t) = p_I(I)p_{\dot{I}}(\dot{I}|I), \tag{3.50}$$

where

$$\dot{I} = \left.\frac{dI(t)}{dt}\right|_t. \tag{3.51}$$

This concept stems from the elementary probability density function relationships, however the proceeding analysis of a joint derivative process is much more difficult when non-Gaussian distributed random variables are considered [39]. This is due primarily to the temporal derivative joint density function $p_I(\dot{I}|I)$ in Equation (3.50). Section 3.3.1 demonstrates that finding an appropriate method to model the joint density of an irradiance signal and its temporal derivative

signal will require approximation. The joint PDF of irradiance I and the time derivative of the irradiance $\dot{I}$ at a multiple moments in time $(t_1, t_2, \dots, t_n)$ will be defined in the proceeding sections as $p_n(I, \dot{I}_1, t_1; I, \dot{I}_2, t_2; \dots; I, \dot{I}_n, t_n)$ to compact notation.

3.3.1 Joint Density of Gamma-Gamma Irradiance and Temporal Derivative

No closed form expression exists for the joint PDF of a gamma-gamma distributed irradiance and its time derivative [13]. However, the joint PDF can be expressed as the product of the gamma-gamma PDF and the conditional PDF of the time derivative. The functional form of the conditional PDF for $\dot{I}$ is not exactly Gaussian, although it has been argued that it will reduce to a zero-mean Gaussian PDF if either $\alpha \to \infty$ or $\beta \to \infty$ (when the gamma-gamma PDF reduces to a gamma PDF) [13]. If this approximation is chosen, the conditional PDF of $\dot{I}$ with respect to I is a zero-mean Gaussian distribution with an irradiance depending variance equal to $4b^2I^2$ and can be written as

$$p_1(I, \dot{I}, t) = \frac{1}{\sqrt{8\pi I b^2}} \exp\left[-\frac{\dot{I}^2}{8Ib^2}\right], \tag{3.52}$$

where b^2 is the variance of the time derivative of a stationary Gaussian random process [13]. It is again useful to mention that the joint PDF of irradiance and the time derivative of irradiance at a moment in time t will be utilized in the proceeding sections as $p_1(I, \dot{I}, t)$ to simplify notation.

As a side note a closed form expression for the joint density of a gamma distributed random variable and its time derivative process has been found to be [13]

$$p_1(I, \dot{I}, t) = \frac{1}{\sqrt{8\pi b^2}} \frac{\alpha^\alpha}{\Gamma(\alpha)} I^{\alpha-3/2} e^{-\alpha x} \exp\left[-\frac{\dot{I}^2}{8b^2 I}\right], \quad I > 0. \tag{3.53}$$

Equation (3.53) is written here only for mathematical interest and will not be utilized in this analysis. Instead, the focus will be on the gamma-gamma result presented beforehand.

3.4 Gamma-Gamma Distributed Irradiance Fading

The following sections will analyze the statistics of gamma-gamma distributed irradiance fade time. Our analysis will be mostly focused on mean and variance in fade time of an irradiance signal whose wave front has been distorted by atmospheric turbulence. The gamma-gamma model parameters will be utilized in order to relate model parameters to physically measureable parameters.

3.4.1 Mean Level Crossing Rate of Gamma-Gamma Distributed Irradiance

It has been previously found that the joint PDF of a gamma-gamma distributed irradiance and its time derivative is

$$p_1(I_T, \dot{I}, t) = \frac{1}{\sqrt{8\pi}} \frac{\alpha^\alpha \beta^\beta}{\Gamma(\alpha)\Gamma(\beta)} I_T^{\beta-3/2} \int_0^\infty \frac{w^{\alpha-\beta-1/2}}{\sqrt{b_x^2 I_T + b_y^2 w^2}} \exp\left[-\alpha w - \frac{\beta I_T}{w} - \frac{\dot{I}^2 w}{8I_T\left(b_x^2 I_T + b_y^2 w^2\right)}\right] dw. \tag{3.54}$$

Inserting Equation (3.54) into Equation (3.34) yields the expression for the expected number of irradiance threshold crossings as

$$\langle n(I_T)\rangle = \frac{1}{2}\frac{1}{\sqrt{8\pi}} \frac{\alpha^\alpha \beta^\beta}{\Gamma(\alpha)\Gamma(\beta)} I_T^{\beta-\frac{3}{2}} \int_0^\infty \frac{w^{\alpha-\beta-\frac{1}{2}}}{\sqrt{b_x^2 I_T + b_y^2 w^2}} \times \exp\left[-\alpha w - \frac{\beta I_T}{w}\right] \int_{-\infty}^\infty \left|\dot{I}(t)\right| \exp\left[-\frac{\dot{I}^2 w}{8I_T\left(b_x^2 I_T + b_y^2 w^2\right)}\right] d\dot{I}\, dw. \tag{3.55}$$

The integral over $\dot{I}$ in Equation (3.55) has been found to be [10]

$$\int_{-\infty}^{\infty} \left|\dot{I}(t)\right| \exp\left[-\frac{\dot{I}^2 w}{8I_T\left(b_x^2 I_T + b_y^2 w^2\right)}\right] d\dot{I} = \frac{8I_T\left(b_x^2 I_T + b_y^2 w^2\right)}{w}, \tag{3.56}$$

and the expected number of fades can then be written as

$$\langle n(I_T)\rangle = \sqrt{\frac{2I_T}{\pi}} \frac{\alpha^\alpha \beta^\beta}{\Gamma(\alpha)\Gamma(\beta)} I_T^{\beta-1} \int_0^\infty w^{\alpha-\beta-3/2} \sqrt{b_x^2 I_T + b_y^2 w^2} \exp\left[-\alpha w - \frac{\beta I_T}{w}\right] dw, \tag{3.57}$$

where b_x^2 and b_y^2 are respectively the large-scale and the small-scale variance of the time derivative of a stationary Gaussian random process. This integral has no known solutions; an approximation will therefore be made to facilitate the mathematical analysis. Define the expected number of fades by the relationship

$$\langle n(I_T)\rangle = \sqrt{\frac{2I_T}{\pi}} \frac{\alpha^\alpha \beta^\beta}{\Gamma(\alpha)\Gamma(\beta)} I_T^{\beta-1} A(\alpha, \beta, I_T), \tag{3.58}$$

where

$$A(\alpha, \beta, I_T) = \int_0^\infty w^{\alpha-\beta-3/2} \sqrt{b_x^2 I_T + b_y^2 w^2} \exp\left[-\alpha w - \frac{\beta I_T}{w}\right] dw. \tag{3.59}$$

Developing approximations to this integral is essential as it is a somewhat difficult, if not completely impossible, integration to solve in closed form. Approximations have been developed for evaluating this integration [10]. As outlined in APPENDIX A

INTEGRAL APPROXIMATION OF GAMMA-GAMMA MEAN FADE TIME

the asymptotic approximation is given as [10]

$$A(\alpha,\beta,I_T)_{Approx\ 1} = b\int_0^\infty w^{\alpha-\beta-1/2}\exp\left[-\alpha w-\frac{\beta I_T}{w}\right]dw \tag{3.60}$$

$$= 2b\left(\frac{\beta I_T}{\alpha}\right)^{\frac{\alpha-\beta}{2}+\frac{1}{4}} K_{\alpha-\beta+1/2}\left(2\sqrt{\alpha\beta I_T}\right).$$

The expected number of fades for gamma-gamma distributed irradiance signal is obtained by insertion of Equation. (3.60) into Equation (3.58), leading to the result

$$\langle n(I_T)\rangle_{Approx\ 1} = 2b\sqrt{\frac{2}{\pi\alpha\beta I_T}}\frac{(\alpha\beta I_T)^{\frac{\alpha-\beta}{2}+\frac{1}{4}}}{\Gamma(\alpha)\Gamma(\beta)}K_{\alpha-\beta+1/2}\left(2\sqrt{\alpha\beta I_T}\right). \tag{3.61}$$

We introduce the quasi frequency ν_0 to describe the temporal bandwidth of the fade distribution, defined with units of Hertz as

$$\nu_0 = \frac{b}{\pi\sigma_{\ln I}}, \tag{3.62}$$

where b is the standard deviation of the time derivative Gaussian random process and $\sigma_{\ln I}$ is the square root of the log irradiance scintillation index. With use of Equation (3.62) the first approximation is then given to be [10]

$$\langle n(I_T)\rangle_{Approx\ 1} = \frac{2\nu_0\sigma_{\ln I}\sqrt{2\pi\alpha\beta}}{\Gamma(\alpha)\Gamma(\beta)}(\alpha\beta I_T)^{\frac{\alpha-\beta}{2}-\frac{1}{4}}K_{\alpha-\beta+1/2}\left(2\sqrt{\alpha\beta I_T}\right). \tag{3.63}$$

A second expression is presented in literature as (with unity normalized irradiance $\langle I\rangle = 1$) [13]

$$\langle n(I_T)\rangle_{Approx\ 2} = \frac{2\sqrt{2\pi\alpha\beta}\nu_0\sigma_I}{\Gamma(\alpha)\Gamma(\beta)}(\alpha\beta I_T)^{\frac{\alpha+\beta-1}{2}}K_{\alpha-\beta}\left(2\sqrt{\alpha\beta I_T}\right). \tag{3.64}$$

For this analysis, the second approximation for the expected number of fades shown in Equation (3.64) will be utilized in data comparison as it is the most widely known of the two presented gamma-gamma model approaches within the published literature [13].

It is useful to redefine the level crossing parameter I_T by an alternative expression,

$$F_T = 10 \log\left(\frac{\langle I \rangle}{I_T}\right). \tag{3.65}$$

This parameter may be approximated by the expression

$$I_T \approx \exp(-0.23F_T), \tag{3.66}$$

where F_T is hereby referred to as the *fade threshold parameter* [7, 10, 13]. With the redefinition in Equation (3.66), the expected number of fades may then be written in terms of the fade threshold parameter as

$$\langle n(F_T) \rangle = \frac{2\nu_0 \sigma_{\ln I}\sqrt{2\pi\alpha\beta}}{\Gamma(\alpha)\Gamma(\beta)} [\alpha\beta \exp(-0.23F_T)]^{\frac{(\alpha+\beta-1)}{2}} \tag{3.67}$$

$$\times K_{\alpha-\beta}\left[2\sqrt{\alpha\beta \exp(-0.23F_T)}\right].$$

Equation (3.67) is utilized in Section 4.4.2 Mean Number of Level Crossings of Experimental Data to compare with experimental data. Additionally, Equation (3.67) is used to compute standard deviation in irradiance signal fade time in Section 4.4.5 Standard Deviation of Fade Time of Experimental Data.

3.4.2 Mean Square Level Crossing Rate of Gamma-Gamma Distributed Irradiance

The major focus of this analysis is the variance in fade time below an arbitrarily specified irradiance threshold I_T. In order to obtain the variance and standard deviation in fade time, the mean square number of level crossings must be determined in addition to the mean number of level crossings. The mean squared number of level crossings for the time irradiance signal $I(t)$ is found by the expression given in Equation (3.36)

$$\overline{n_0^2} = \iint_{-\infty}^{\infty} |\dot{I}_1|\,|\dot{I}_2|\, p_2(I_T, \dot{I}_1, t_1; I_T, \dot{I}_2, t_2)\, d\dot{I}_1 d\dot{I}_2, \tag{3.68}$$

where I_T is the irradiance crossing threshold, $\dot{I}_n$ is the time derivative of the irradiance signal at the n^{th} moment in time (t_n), and $p_2(I_T, \dot{I}_1, t_1; I_T, \dot{I}_2, t_2)$ is the joint density of the irradiance and the time derivative of irradiance at two separate instances in time, t_1 and t_2. From the discussions of Middleton, the expression $p_2(I_T, \dot{I}_1, t_1; I_T, \dot{I}_2, t_2)$ can be written in terms of the conditional density distribution as [39]

$$p_2(I_T, \dot{I}_1, t_1; I_T, \dot{I}_2, t_2) = p_1(I_T, \dot{I}_1, t_1) p_2(I_T, \dot{I}_1, t_1 | I_T, \dot{I}_2, t_2). \tag{3.69}$$

In consideration of two instances in time, t_1 and t_2, we examine an assumption presented by Middleton. If the instances are separated by a sufficiently large amount of time (such that the cross-wind speed $v_\perp$ and path length L satisfy $t_2 - t_1 \gg \frac{v_\perp}{L}$), the conditional density distribution can be written as [4, 5, 7, 39]

$$\lim_{t_2 - t_1 \to \infty} p_2(I_T, \dot{I}_1, t_1; I_T, \dot{I}_2, t_2) = p_1(I_T, \dot{I}_1, t_1) p_1(I_T, \dot{I}_2, t_2). \tag{3.70}$$

It is postulated that since atmospheric conditions represent a process which remains stationary for a time period long enough for Equation (3.71) to be valid, the joint density of the irradiance

and the time derivative of the irradiance at two moments separated by a large amount of time can be expressed as

$$p_2(I_T, \dot{I}_1, t_1; I_T, \dot{I}_2, t_2) = p_1(I_T, \dot{I}_1, t_1)p_1(I_T, \dot{I}_2, t_2). \tag{3.71}$$

We will hold that this approach presents an approximation to the actual random process of study; it is documented in literature that the atmosphere presents itself as stationary about half hour increments [4, 5]. Therefore it is appropriate to use the notation

$$p_2(I_T, \dot{I}_1, t_1; I_T, \dot{I}_2, t_2) \cong p_1(I_T, \dot{I}_1, t_1)p_1(I_T, \dot{I}_2, t_2). \tag{3.72}$$

An approximation for the probability density function of a gamma-gamma distributed irradiance at level I_T and its time derivative $\dot{I}_n$, at a moment in time t_n, is given in Section 3.3 Joint Density of a Random Variable and its Temporal Derivative to be

$$\begin{aligned} p_1(I_T, \dot{I}_n, t_n) \cong \frac{2(\alpha\beta)^{\frac{\alpha+\beta}{2}}}{\Gamma(\alpha)\Gamma(\beta)I_T}\left(\frac{I_T}{\langle I\rangle}\right)^{\frac{\alpha+\beta}{2}} K_{\alpha-\beta}\left(2\sqrt{\frac{\alpha\beta I_T}{\langle I\rangle}}\right) \\ \times \frac{1}{2\sqrt{2\pi b I_T}}\exp\left(-\frac{\dot{I}_n^2}{8bI_T}\right), \end{aligned} \tag{3.73}$$

where α and β are the gamma-gamma PDF parameters (related directly to the scintillation index σ_I^2), and b is the derivative process contributed parameter (a parameter that may be redefined in terms of the quasi frequency ν_0 and scintillation index σ_I^2) [13]. The expression for b is given in terms of the quasifrequency as [13]

$$\nu_0 = \frac{1}{\pi\sigma_I}\sqrt{\frac{b}{\langle I\rangle}}, \tag{3.74}$$

and this then can be rearranged to find

$$b = \langle I \rangle (\nu_0 \pi \sigma_I)^2. \tag{3.75}$$

The expression for the joint density of a gamma-gamma distributed irradiance and its derivative, at two moments separated sufficiently in time, may be estimated as

$$\begin{aligned} p_2(I_T, \dot{I}_1, t_1; I_T, \dot{I}_2, t_2) &\cong p_1(I_T, \dot{I}_1, t_1) p_1(I_T, \dot{I}_2, t_2) \\ &\cong \left[\frac{2(\alpha\beta)^{\frac{\alpha+\beta}{2}}}{\Gamma(\alpha)\Gamma(\beta) I_T} \left(\frac{I_T}{\langle I \rangle} \right)^{\frac{\alpha+\beta}{2}} K_{\alpha-\beta}\left(2\sqrt{\frac{\alpha\beta I_T}{\langle I \rangle}} \right) \times \frac{1}{2\sqrt{2\pi b I_T}} \exp\left(-\frac{\dot{I}_1^2}{8 b I_T} \right) \right] \\ &\times \left[\frac{2(\alpha\beta)^{\frac{\alpha+\beta}{2}}}{\Gamma(\alpha)\Gamma(\beta) I_T} \left(\frac{I_T}{\langle I \rangle} \right)^{\frac{\alpha+\beta}{2}} K_{\alpha-\beta}\left(2\sqrt{\frac{\alpha\beta I_T}{\langle I \rangle}} \right) \times \frac{1}{2\sqrt{2\pi b I_T}} \exp\left(-\frac{\dot{I}_2^2}{8 b I_T} \right) \right] \\ &\cong \frac{1}{2\pi b I_T} \left[\frac{\alpha\beta I_T}{\langle I \rangle} \right]^{\alpha+\beta} \left[\frac{K_{\alpha-\beta}\left(2\sqrt{\frac{\alpha\beta I_T}{\langle I \rangle}} \right)}{\Gamma(\alpha)\Gamma(\beta) I_T} \right]^2 \exp\left(-\frac{\dot{I}_1^2 + \dot{I}_2^2}{8 b I_T} \right) \end{aligned} \tag{3.76}$$

where I_T is the normalized threshold irradiance, $\dot{I}_1$ and $\dot{I}_2$ are the derivative of the normalized irradiance at times t_1 and t_2, α and β are the effective number of large scale and small scale scatterers, b is the standard deviations of the time derivative of a Gaussian random process associated with the large scale and small scale irradiances. By inserting Equation (3.76) into Equation (3.68) it is found that the mean square number of crossings for a gamma-gamma distributed irradiance becomes approximately

$$\overline{n^2} = \int_{-\infty}^{\infty} \int |\dot{I}_1| \, |\dot{I}_2| \, p_2(I_T, \dot{I}_1, t_1; I_T, \dot{I}_2, t_2) \, d\dot{I}_1 d\dot{I}_2 \tag{3.77}$$

$$\cong \int_{-\infty}^{\infty}\int_{-\infty}^{\infty} |\dot{I}_1|\,|\dot{I}_2|\,\frac{1}{2\pi b I_T}\left[\frac{\alpha\beta I_T}{\langle I\rangle}\right]^{\alpha+\beta}\left[\frac{K_{\alpha-\beta}\left(2\sqrt{\frac{\alpha\beta I_T}{\langle I\rangle}}\right)}{\Gamma(\alpha)\Gamma(\beta)I_T}\right]^2 \exp\left(-\frac{\dot{I}_1^2+\dot{I}_2^2}{8bI_T}\right)d\dot{I}_1 d\dot{I}_2$$

The integrations involving the derivative irradiance are recognized such that one is able to rearrange the expressions in Equation (3.77) as

$$\overline{n^2} \cong \frac{1}{2\pi b I_T}\left[\frac{\alpha\beta I_T}{\langle I\rangle}\right]^{\alpha+\beta}\left[\frac{K_{\alpha-\beta}\left(2\sqrt{\frac{\alpha\beta I_T}{\langle I\rangle}}\right)}{\Gamma(\alpha)\Gamma(\beta)I_T}\right]^2 \tag{3.78}$$

$$\times \int_{-\infty}^{\infty} |\dot{I}_1| \exp\left(-\frac{\dot{I}_1^2}{8bI_T}\right)d\dot{I}_1$$

$$\times \int_{-\infty}^{\infty} |\dot{I}_2| \exp\left(-\frac{\dot{I}_2^2}{8bI_T}\right)d\dot{I}_2.$$

The sought integrations of Equation (3.78) are identical and may written in terms of the improvised function

$$M_I(b, I_T) = \int_{-\infty}^{\infty} |\dot{I}_n|\ \exp\left[-\frac{\dot{I}_n^2}{8bI_T}\right]d\dot{I}_n, \tag{3.79}$$

where $\dot{I}_n$ denotes the derivative with respect to the n^{th} moment in time t_n.The mean square number of crossings is then found to be

$$\overline{n^2} \cong \frac{1}{2\pi b I_T}\left[\frac{\alpha\beta I_T}{\langle I\rangle}\right]^{\alpha+\beta}\left[\frac{M_I(b, I_T)\ K_{\alpha-\beta}\left(2\sqrt{\frac{\alpha\beta I_T}{\langle I\rangle}}\right)}{\Gamma(\alpha)\Gamma(\beta)I_T}\right]^2 \tag{3.80}$$

It is recognized that the integral $M_I(b, I_T)$ involving the derivative terms, $\dot{I}_1$ and $\dot{I}_2$, is tractable with the elementary integral relation

$$\int_{-\infty}^{\infty} |\gamma| e^{-\gamma^2} d\gamma = 1, \tag{3.81}$$

where γ is a dummy variable of integration. From Equation (3.79) it is identified that one should make use of the substitution

$$\gamma^2 = \frac{\dot{I}_n^2}{8bI_T}, \tag{3.82}$$

then, assuming the positive root of

$$\pm\gamma = \dot{I}_n \sqrt{\frac{1}{8bI_T}}, \tag{3.83}$$

it is found that

$$d\gamma = d\dot{I}_n \sqrt{\frac{1}{8bI_T}}. \tag{3.84}$$

From this, the integration can be evaluated as

$$M_I(b, I_T) = \sqrt{8bI_T} \int_{-\infty}^{\infty} |\gamma|\, e^{-\gamma^2} d\gamma, \tag{3.85}$$

$$= \sqrt{8bI_T}.$$

With substitution of the relationship from Equation (3.85) into Equation (3.80), the mean square number of level crossings becomes

$$\overline{n^2} \cong \frac{1}{2\pi b I_T}\left[\frac{\alpha\beta I_T}{\langle I\rangle}\right]^{\alpha+\beta}\left[\frac{M_I(b, I_T)\, K_{\alpha-\beta}\left(2\sqrt{\frac{\alpha\beta I_T}{\langle I\rangle}}\right)}{\Gamma(\alpha)\Gamma(\beta) I_T}\right]^2 \tag{3.86}$$

$$\cong \frac{1}{2\pi b I_T}\left[\frac{\alpha\beta I_T}{\langle I\rangle}\right]^{\alpha+\beta}\left[\frac{\sqrt{8bI_T}\, K_{\alpha-\beta}\left(2\sqrt{\frac{\alpha\beta I_T}{\langle I\rangle}}\right)}{\Gamma(\alpha)\Gamma(\beta) I_T}\right]^2$$

$$\cong \frac{4}{\pi}\left[\frac{\alpha\beta I_T}{\langle I\rangle}\right]^{\alpha+\beta}\left[\frac{K_{\alpha-\beta}\left(2\sqrt{\frac{\alpha\beta I_T}{\langle I\rangle}}\right)}{\Gamma(\alpha)\Gamma(\beta) I_T}\right]^2.$$

The approximate expression for the mean square number of level crossings can then be written as

$$\overline{n^2} \cong \frac{4}{\pi}\left[\frac{\alpha\beta I_T}{\langle I\rangle}\right]^{\alpha+\beta}\left[\frac{K_{\alpha-\beta}\left(2\sqrt{\frac{\alpha\beta I_T}{\langle I\rangle}}\right)}{\Gamma(\alpha)\Gamma(\beta) I_T}\right]^2. \tag{3.87}$$

Equation (3.87) is the derived expression with which experimental data is used to validate in Section 4.4.4 Mean Square Number of Level Crossings of Experimental Data.

3.4.3 Gamma-Gamma Fade Time Statistics

The average time (in seconds) which the gamma-gamma distributed irradiance signal $I(t)$ stays below a specified irradiance level I_T is found with knowledge of the expected number of fades and the probability of fade. As presented in Section 3.2.3, the expected fade time is the ratio [13]

$$\langle t(I_T)\rangle = \frac{\Pr(I \le I_T)}{\langle n(I_T)\rangle}, \tag{3.88}$$

with $\Pr(I \leq I_T)$ representing the probability that the irradiance $I(t)$ falls below the irradiance threshold level I_T and $\langle n(I_T)\rangle$ being the expected number of fades per second.

Higher order moments such as the mean square fade time $\langle t^2(I_T)\rangle$ (units of seconds squared) of irradiance signal $I(t)$ below the irradiance threshold level I_T may be concurrently developed by Equation (3.46). To find the mean square fade time, we consider taking the square root of second moment of level crossings $\langle n^2(I_T)\rangle$ to proceed with the analysis and maintain consistent units. From here, we proceed as with mean fade time

$$\sqrt{\langle t^2(I_T)\rangle} = \frac{\Pr(I \leq I_T)}{\sqrt{\langle n^2(I_T)\rangle}}, \tag{3.89}$$

we must square the result obtained in Equation (3.47) to reach the desired expression for mean square fade time $\langle t^2(I_T)\rangle$. Similarly, higher order moments may be obtained through use of this method as units will maintain the desired consistency. For this analysis, the probability of fade $\Pr(I \leq I_T)$ will be computed numerically through experimental data by the cumulative distribution function (CDF). This will allow numerical data to maintain a tractable analysis.

With the expressions for mean fade time and mean square fade time, variance of fade time and standard deviation of fade time may then be readily found. As with regular statistical moments, the variance in fade time may be expressed in terms of the mean fade time $\langle t(I_T)\rangle$ and mean square fade time $\langle t^2(I_T)\rangle$ as

$$VAR[t(I_T)] = \langle t^2(I_T)\rangle - \langle t(I_T)\rangle^2, \tag{3.90}$$

this has units of seconds to the square power. In addition, the standard deviation in fade time may be found by taking the square root of Equation (3.48) and readily stated

$$StDEV[t(I_T)] = (VAR[t(I_T)])^{1/2}. \quad (3.91)$$

Standard deviation of fade time has the same units as the average value, seconds.

4. EXPERIMENTATION

The purpose of this section is to detail the experimental data instrumentation, its setup, and the processing of collected data.

4.1 Overview of Measurements and Data Processing

532nm laser irradiance data were collected over a path length of 980 meters at the Innovative Science and Technology Experimentation Facility (ISTEF) located within the Kennedy Space Center at Cape Canaveral, Florida. Irradiance data were collected in moderate-to-strong turbulence conditions with different sized aperture over a fixed duration of 2 minutes each. Before each collection of laser signal data, background data were collected over a fixed duration of 20 seconds. The collected data were analyzed for stationarity and defects. Valid data were processed after the experimentation had completed in the MATLAB programming environment with 64-bit Windows and 64-bit Linux computer architectures. PDF of the irradiance data were computed and compared with lognormal, gamma, and gamma-gamma PDF models to allow execute comparison. Gamma-gamma model comparisons will be the main presentation of this analysis as it mirrors the theory that is presented in the previous sections.

4.1.1 Innovative Science and Experimentation Facility (ISTEF)

The Innovative Science and Experimentation Facility (ISTEF) is located within the Kennedy Space Center (KSC) at Cape Canaveral, Florida. The facility has a 1km laser range, a path that predominately consists of light vegetation with a row of groomed trees on each side. A photograph of the facility is shown in Figure 9.

Figure 9: The Innovative Science and Experimentation Facility (ISTEF)

In addition, a photograph illustrating a typical experimental setup for the SLS-20 and BLS-900 scintillometers 1km down range from the ISTEF main facility is shown in Figure 10. Vegetation is maintained regularly to prevent shrub blockage during laser experimentation and shrubbery extends to a height of roughly on each side of the range. The laser range is approximately level in elevation; however it has been observed by the author to not be completely flat for the entire 1km path length.

Figure 10: Equipment setup at ISTEF

4.1.2 Measured Macrometeorological Atmospheric Parameters

The ISTEF range was instrumented with several weather instruments. Instrumentation included two Scintec SLS-20 scintillometers, one Scintec BLS-900 scintillometer, and three Applied Technologies three-axis sonic anemometers [47-49]. Scintillometer measurements provided real time values of the refractive index structure constant C_n^2 and the inner scale l_0 at a rate of one measurement per minute (~.0167 Hz). Sonic anemometers provided three-dimensional wind speed measurements, as well as temperature data, at a rate of 10Hz. The values were measured for comparison with theoretical models. Knowledge of path averaged channel conditions C_n^2 and l_0 may be utilized to predict additional models used to study FSO communication systems.

The gamma-gamma model parameters representing the large-scale scatterers α and small-scale scatterers β can be calculated from C_n^2, l_0, and L_0 (see APPENDIX B RELATION OF GAMMA-GAMMA MODEL PARAMETERS TO MEASURED PARAMETERS

). Another such parameter that may be inferred from measurements of C_n^2, l_0, and L_0 is the spherical wave spatial coherence length ρ_{sp}. The expression for this parameter is given in Section 2.4 Aperture Averaging as

$$\rho_{sp} = (0.55C_n^2 k^2 L)^{-3/5}, \quad l_0 \ll \rho_{sp} \ll L_0, \tag{4.1}$$

where k is the wave number, L is the path length, and it is assumed that $L_0 = \infty$ [7]. This number generally describes the amount of atmospheric turbulence induced by the channel in account of the refractive-index structure constant and the inner-scale, but with outer-scale dependence neglected. When the aperture diameter exceeds the spatial coherence length by three times or more, aperture averaging effects are said to then be present.

4.2 Transmitter Experimental Set-Up

For these experiments, a continuous-wave 532nm diode-pumped solid state laser with a maximum output power of approximately 800mW was utilized. The transmitter system was setup on an optical bench within the ISTEF laboratory, and aimed downrange through an open window such that the receiver imaged an unobstructed laser signal. As the DPSS laser was operated at maximum power levels, the output mode structure evolved from fundamental to a TEM_{20} mode. To remove undesired spatial modes, a spatial filter of about 1mm was positioned at the center of the beam. The center portion of the beam was then passed through a defocused beam expander in effort to obtain an approximately spherical wave front at the receiver. The output divergence was tuned such that the spot radius at the receiver was measured with an imaging system to be about 2 meters (indicating a full-angle divergence of approximately 4mrad) [50]. To find an indication that a spherical wave would be obtained at the receiver, it is necessary to use the refractive beam parameter given in literature as

$$\Lambda_0 = \frac{2z}{kW_0^2} \tag{4.2}$$

where z is the path length, k is the wave number, and W_0 is the beam spot radius [7, 50, 51]. The refractive beam parameter Λ_0 was calculated at the receiver to be a value of approximately ~ 75, implying that the receiver was in the far-field (signifying an approximately spherical wave at the receiver) [7].

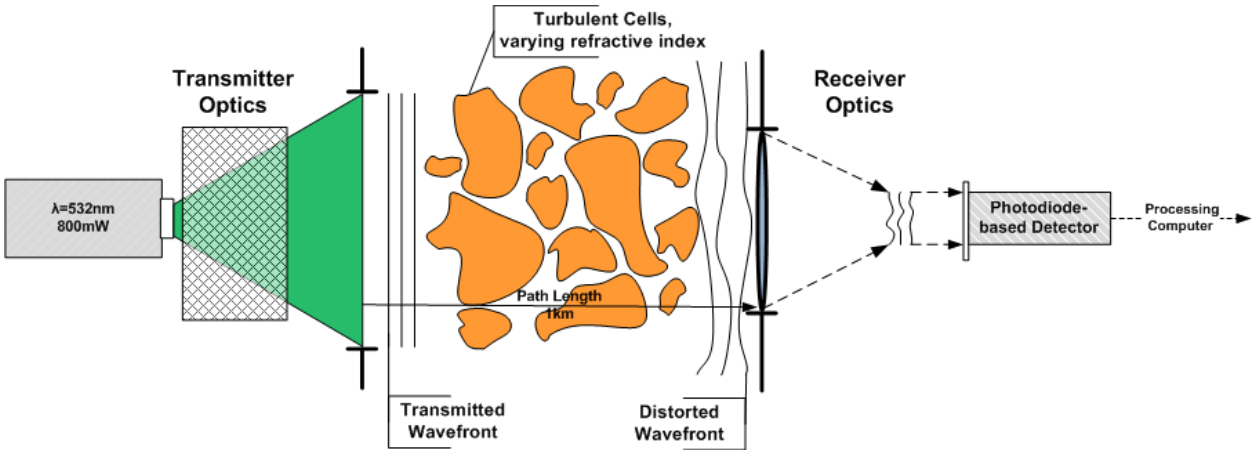

Figure 11: Experimentation overview, transmitter and receiver set-up.

4.3 Receiver Experimental Set-Up

The receiving telescope was previously utilized in experiments under the Optical RF Communications Adjunct (ORCA) project funded by the Defense Advanced Research Projects Agency (DARPA). The telescope had been configured as a pupil plane imaging system. The primary lens was a 6 inch diameter refracting lens. A relay lens was positioned in the focal plane of the primary lens in order to project an image of the pupil plane onto the detector array. The New Focus 2101 power meter was utilized as the detector in this experiment for its high dynamic range, roughly 70dB, and its high sampling frequency 25kHz [18]. The detector surface is 5mm diameter silicon photodiode, which due to its large area, allowed for an easier alignment in the

focal place of the relay lens. The relay lens had a magnification such that a 2mm image of the pupil plane was created at the focal distance. Also, this relay lens is the aperture stop of the optical system and therefore defines the field of view. This system gives the advantage of minimal dependence on the focus of the receiving telescope, as the telescope can change focus and there will be a minimal effect on the amount of light received by the detector. Setup of lens and telescope are shown in Figure 12.

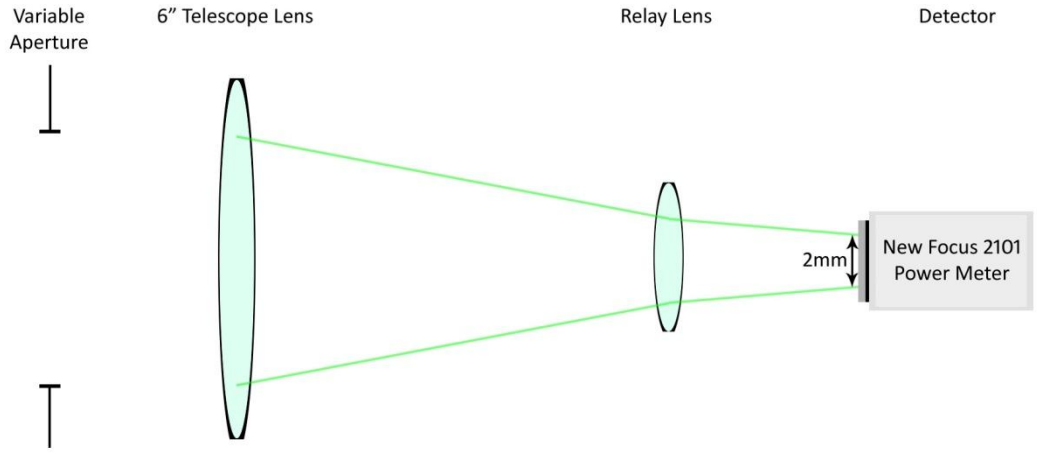

Figure 12: Experiment aperture, lens, and detector setup.

Power meter data were recorded on computer hardware with the use of a National Instruments NI9234 digitizer, utilizing a National Instruments NI ENET 9163 Ethernet carrier. The digitizer was operated at 51.5kS/s and it has a 24-bit resolution [52]. This combination transformed the power meter voltage output into a 24-bit digitized signal that was received over Ethernet by a computer utilizing the National Instruments LabVIEW Signal Express software.

4.4 Experimental Data Analysis

This section outlines the results of the data collected during experimentation, and details a comparison with the theoretical models introduced by the previous sections. The presented data were collected from about 13:00EST to 16:30EST on October 2nd, 2009 at the ISTEF laser range located within the Kennedy Space Center. The data were hastily recorded such that the statistics of the received irradiance fluctuations for various aperture diameters could be compared under somewhat similar atmospheric conditions.

Measurement from the three-axis sonic anemometers at the transmitter revealed path characteristics very similar to those measured at the receiver. At the transmitter, average magnitude of wind speed was roughly 0.05 m/s with wind gusts of about 1.5 m/s. On the receiver side, the magnitude of wind speed measurements was about 0.1 m/s on average with occasional 1.5 m/s gusts. One SLS-20 scintillometer was positioned at the transmitter and another was positioned near the receiver. The SLS-20's were used to record the refractive index structure constant C_n^2 and the inner scale of turbulence l_0. Table 1 provides a summary of the atmospheric conditions of C_n^2, l_0, and ρ_{sp} at the times of data collection. Data is presented in order of increasing aperture size. As a generalization, it is expected for apertures that are smaller than the spatial coherence length $D < \rho_{sp}$ to match the gamma-gamma models better than apertures that are larger than the spatial coherence length $D > \rho_{sp}$ [7, 13, 33, 35]. Aperture averaging effects are said to prevalent when the aperture diameter exceeds the spatial coherence length by three times or more ($D > 3\rho_{sp}$) [7, 13].

It is noted that during the 1.5mm diameter data collection the SNR was at the experiment's minimum since it is the experimentation's smallest diameter aperture ($SNR{\sim}D$). Conversely, the experiment's maximum theoretical SNR occurred during the data collection with 154mm diameter aperture as it represents the largest area of collection for the received irradiance signal.

Table 1: Summary of atmospheric conditions during experimentation

Aperture Size (mm)	C_n^2 ($m^{-2/3}$) (measured)	l_0 (mm) (measured)	ρ_{sp} (mm) (calculated)	Time (EST)
1.5	$5.00 \cdot 10^{-14}$	5.69	6.89	16:01
4.0	$8.50 \cdot 10^{-14}$	6.00	5.33	15:32
4.0	$9.00 \cdot 10^{-14}$	6.02	5.19	16:19
7.0	$7.50 \cdot 10^{-14}$	5.93	5.67	16:15
10.0	$9.00 \cdot 10^{-14}$	4.98	2.53	13:15
10.0	$5.50 \cdot 10^{-14}$	4.91	6.41	15:26
20.6	$3.70 \cdot 10^{-14}$	4.86	2.47	13:11
20.6	$8.89 \cdot 10^{-14}$	5.54	5.15	15:21
20.6	$7.00 \cdot 10^{-14}$	5.90	5.86	15:56
55.0	$2.65 \cdot 10^{-13}$	5.43	2.97	13:07
55.0	$1.05 \cdot 10^{-13}$	6.23	4.83	15:51
101.6	$1.40 \cdot 10^{-13}$	5.74	4.12	15:47
154.0	$3.47 \cdot 10^{-13}$	5.46	2.60	13:04

In addition, the gamma-gamma large-scale and small-scale scattering parameters are estimated from the measurement of atmospheric parameters C_n^2, l_0, and L_0. The procedure of related atmospheric measurements to the gamma-gamma model parameters is given in APPENDIX B

RELATION OF GAMMA-GAMMA MODEL PARAMETERS TO MEASURED PARAMETERS

. The gamma-gamma model parameters calculated by atmospheric measurements are notated in the plots as α_{thry} and β_{thry}. A scintillation index based from the atmospheric measurement of α_{thry} and β_{thry} may be developed using Equation (3.20) as

$$\sigma_{I\,thry}^2 = \left(1 + \frac{1}{\alpha_{thry}}\right)\left(1 + \frac{1}{\beta_{thry}}\right) - 1. \tag{4.3}$$

The received signal is an intensity signal (with units of Watts) as the aperture integrates the irradiance signal received by the detector. Data for each aperture were collected at the ISTEF range while being examined in realtime for stationarity. The experiment's data was then post processed such that it was confidently reduced to stationary segments of approximately one minute in length.

Comparison of experimental data and gamma-gamma model PDF plots are presented with an emphasis on aperture averaging characteristics, and we use *irradiance* to denote the power received by the detector as it is common in the literature [7, 13]. Then the mean number of level crossings and mean fade time of the received irradiance fluctuations are compared with the results of the gamma-gamma model. Finally, mean square number of level crossings and standard deviation of fade time are analyzed and compared with the results of the gamma-gamma model. Data will be presented in order of increasing aperture size (the smallest aperture size of 1.5mm being the first). The parameters used to model the gamma-gamma distribution will be tabulated in each section for convenience.

4.4.1 PDF of Experimental Data

Probability density data were computed from the irradiance data received with each of the apertures. This data were then compared with the gamma-gamma model presented in Section 3.1.2 Gamma-Gamma Distribution. Best fit gamma-gamma model parameters were determined from the data. The large-scale scattering parameter is notated as $\alpha_{gg\ pdf}$ and the small-scale scattering parameter is notated as $\beta_{gg\ pdf}$. Similarly, a scintllation index may be developed from the parameters using Equation (3.20) as

$$\sigma^2_{I\,gg\ pdf} = \left(1 + \frac{1}{\alpha_{gg\ pdf}}\right)\left(1 + \frac{1}{\beta_{gg\ pdf}}\right) - 1. \tag{4.4}$$

The scintillation index calculated from the experimentally collected irradiance data $\sigma^2_{I\,meas}$ is compared with the scintillation indices computed from PDF modeled gamma-gamma parameters $\sigma^2_{I\,gg\ pdf}$ and the atmosphere inferred gamma-gamma parameters $\sigma^2_{I\,thry}$.

The gamma-gamma PDF models are obtained by first taking the received irradiance signal, and normalizing the irradiance signal such that the new normalized irradiance signal has a mean of unity. Forth with the received irradiance signal $I(t)$, we formulate a *mean normalized irradiance signal* $I_{norm}\ (t)$ by the definition

$$I_{norm}\ (t) = \frac{I(t)}{\langle I(t)\rangle}. \tag{4.5}$$

It is observed that this normalization will lead to a irradiance distributed about a mean of unity ($\langle I_{norm}\ (t)\rangle = 1$). Normalization of the received irradiance signal by the mean irradiance value will allow the PDF plots to be more readily compared with one another. PDF plots are presented with the ordinance containing irradiance given in units of decibels (dB), with the respect to mean

irradiance. The relationship between the received irradiance signal, the irradiance mean value, and the utilized irradiance ordinance in decibels is

$$I_{dB}(t) = 10\log_{10}\left(I_{norm}(t)\right) = 10\log_{10}\left[\frac{I(t)}{\langle I(t)\rangle}\right]. \quad (4.6)$$

Additionally this normalization will place the peak of the PDF typically near but not exactly at the value of unity irradiance (0dB) [7, 50]. It is normally observed that the PDF resembles a *wide horseshoe shape*, and with the characteristic that the dynamic range of the received irradiance exhibits a dependence on the receiver aperture diameter D [7, 13, 33, 50].

The information in Section 2.4 Aperture Averaging provides an introduction to the influence aperture size has on the received irradiance fluctuations. Aperture averaging is expected to play the least role in reducing fluctuations when analyzing an aperture of diameter $D < \rho_{sp}$, previous examinations of experimentally collected PDF irradiance data confirm this notion [7, 12, 13, 31, 33-35]. As the receiver diameter increases it is known that the irradiance fluctuations, quantified through the irradiance scintillation index σ_I^2, will reduce. As the aperture diameter begins to increase beyond the spatial coherence radius, effects of aperture averaging in the received irradiance PDF become more prevalent and the gamma-gamma model becomes a less accurate approximation (see Section 2.4 Aperture Averaging) [10, 33]. Aperture averaging is established to be present when the aperture diameter exceeds the spatial coherence length by three times or more ($D > 3\rho_{sp}$) [7, 13].

Comparison of PDF data confirm that irradiance fluctuations reduce as aperture diameter increases. A decrease in the scintillation index will cause the received irradiance signal

fluctuations to exhibit a reduced dynamic range [7, 13, 50]. The results of the presented gamma-gamma PDF model and experimental data are tabulated for convenience in Table 2: Summary of gamma-gamma PDF model data.

Table 2: Summary of gamma-gamma PDF model data

Aperture Size (mm)	$\alpha_{gg\ pdf}$	$\beta_{gg\ pdf}$	$\sigma^2_{I\ gg\ pdf}$	α_{thry}	β_{thry}	$\sigma^2_{I\ thry}$	$\sigma^2_{I\ meas}$	Time (EST)
1.5	1.74	4.02	0.968	1.40	1.60	1.786	1.296	16:01
4.0	1.71	1.71	1.511	0.90	1.30	2.735	2.253	15:32
4.0	1.85	1.85	1.374	0.90	1.30	2.735	1.934	16:19
7.0	1.99	1.99	1.254	1.00	1.70	2.176	1.820	16:15
10.0	2.36	2.36	1.029	1.30	2.20	1.573	1.312	15:26
10.0	1.93	1.93	1.305	0.60	5.10	2.190	2.418	13:15
20.6	3.14	3.15	0.737	1.30	4.90	1.130	0.857	15:56
20.6	2.60	2.61	0.917	1.10	5.20	1.276	1.071	15:21
20.6	2.29	2.28	1.065	0.60	19.30	1.805	1.500	13:11
55.0	2.29	11.36	0.564	1.10	89.30	0.930	0.588	13:07
55.0	2.48	34.90	0.413	1.90	34.90	0.570	0.247	15:51
101.6	5.29	151.30	0.197	4.30	150.40	0.241	0.161	15:47
154.0	4.80	67.60	0.226	4.80	950.40	0.210	0.178	13:04

Figure 13 shows the PDF of the irradiance data received under somewhat weak-atmospheric conditions ($C_n^2 \sim 10^{-14}$), with an aperture diameter of 1.5mm, and a spatial coherence length ρ_{sp} of 6.89mm. The received irradiance signal displays a comparatively large dynamic range, with a considerable amount of probability density of the received irradiance signal falling into the lower

end of detection range. As such, the entire mean-normalized irradiance range width of the PDF is difficult to be accurately represented and we will only analyze the portion considered to be valid in measurement. This larger fluctuation about the mean value translates to a greater signal variance (smaller apertures exhibit a larger scintillation index than larger apertures). It is also known that the 1.5mm aperture exhibits the poorest SNR of the experimentation due to the wide dynamic range of intensity (irradiance integrated across the aperture). This leads to the expectation that the received signal will also exhibit a strong presence of low power levels. Given that the ISTEF range is cleared for eye-hazardous laser operation, a useable SNR was able to be achieved by transmitting at the laser's maximum output power. Since the smallest aperture also generally corresponds to the largest irradiance dynamic range in the PDF of received irradiance signal, the PDF will be wider in appearance with lower and upper irradiance tail appearing to be more flat in slope [7, 31, 50].

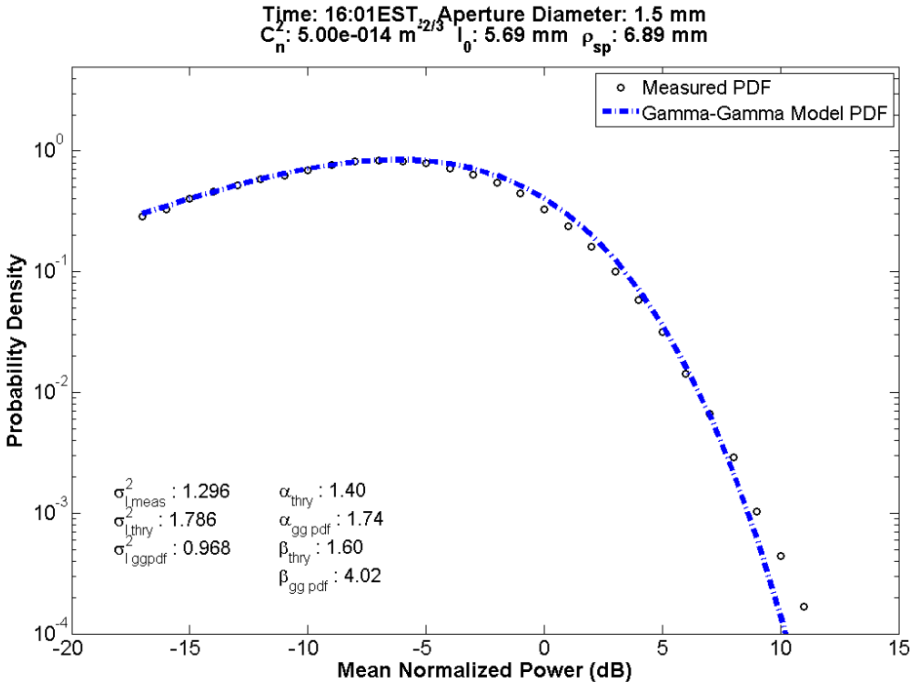

Figure 13 Experimental data PDF, 1.5mm aperture diameter

The irradiance data collected with the 4mm aperture is presented in Figure 14. During this run, the atmospheric turbulence conditions were still somewhat weak in magnitude. Aperture diameter D is slightly less than the spherical wave spatial coherence length ρ_{sp} of 5.33mm. This implies that there will not be significant aperture averaging ($D < 3\rho_{sp}$), although the trend will begin to display its characteristics as the aperture diameter D increases above the spatial coherence length ($D > 3\rho_{sp}$). As aperture size increases, the PDF shape becomes narrower with the upper and lower tails exhibiting a steeper slope. A second collection of 4mm aperture data is presented in Figure 15, with atmospheric conditions remaining almost exact. The results of the similar diameter and atmospheric characteristics mirror one another.

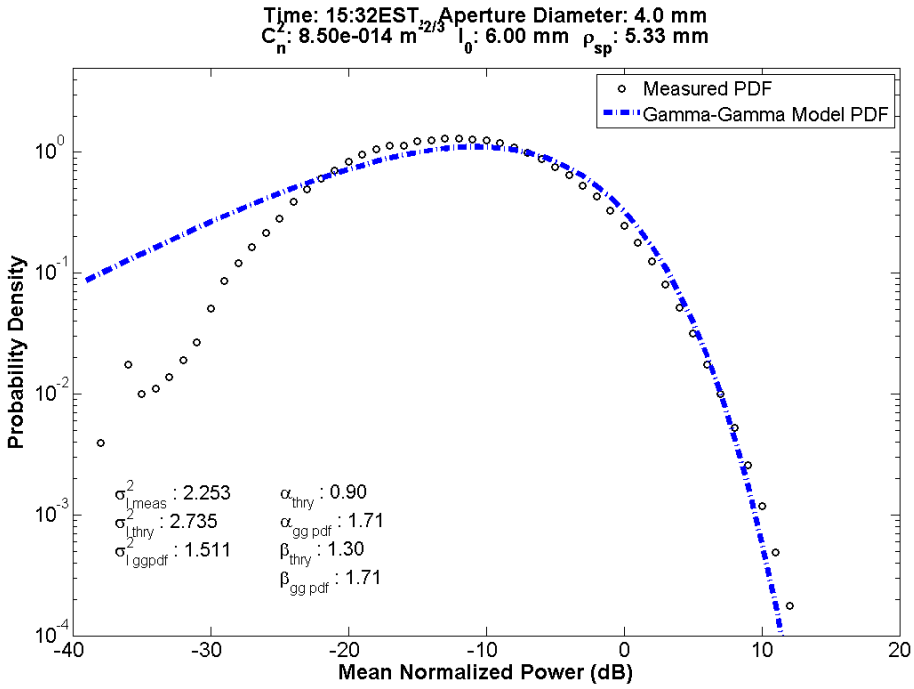

Figure 14: Experimental data PDF, 4.0mm aperture diameter.

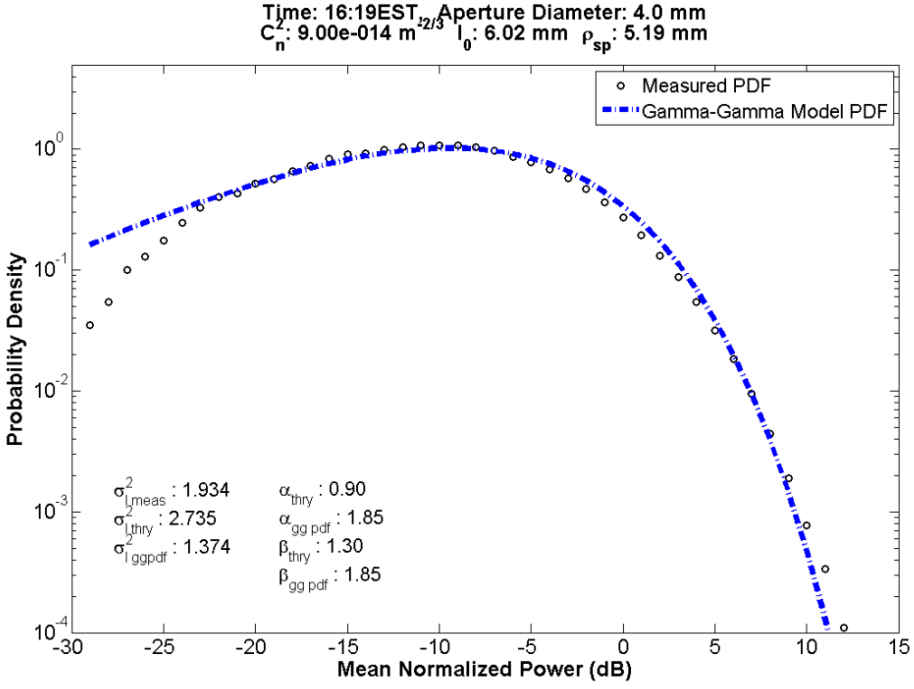

Figure 15: Experimental data PDF, 4.0mm aperture diameter.

The irradiance data collected with the 7mm aperture is presented in Figure 14. During this run, the atmospheric turbulence conditions were still somewhat weak in magnitude. Aperture diameter D is approximately a millimeter or two greater than the spherical wave spatial coherence length ρ_{sp} of 5.67mm. The onset of aperture averaging effects is starting to become more apparent than they were with the 4mm aperture, however the result will be more drastic as diameter is further increased. At this point, the mean-normalized irradiance dynamic range is approximately 40dB in width.

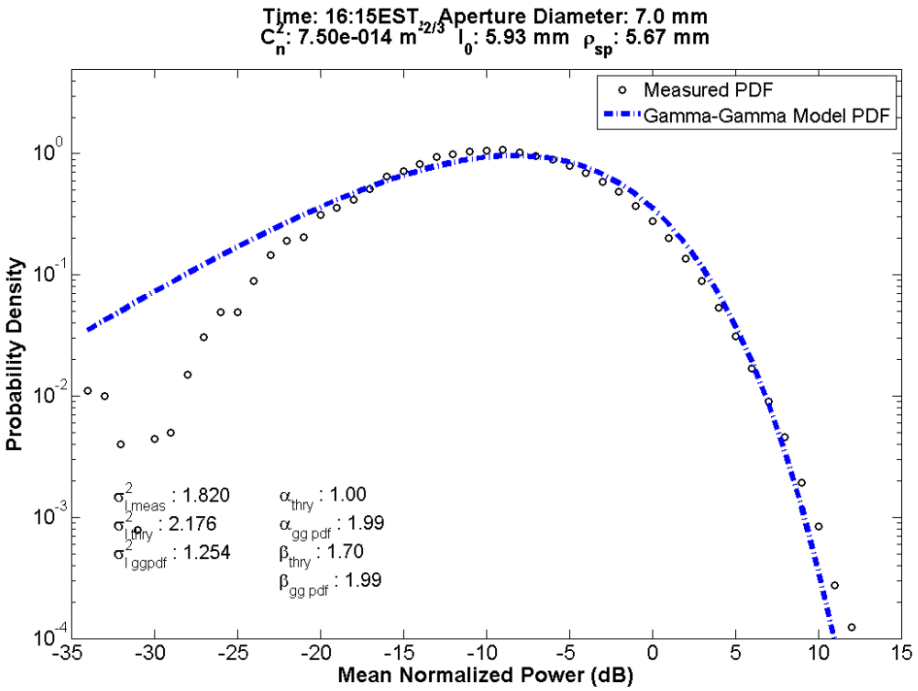

Figure 16: Experimental data PDF, 7.0mm aperture diameter.

The irradiance data collected with the 10mm aperture is presented in Figure 17. For comparison, Figure 18 has exemplified the effect of increasing the atmospheric turbulence (C_n^2 approximately one order of magnitude larger in Figure 18 than demonstrated in Figure 17). At the time of

13:15EST, atmospheric turbulence conditions were moderate in magnitude whereas it was becoming somewhat weaker by 15:26EST. A greater dynamic range in received irradiance fluctuations can be observed in Figure 18 exhibiting the greater turbulence. In this PDF, the aperture diameter D is considerably more ($D > 3\rho_{sp}$) than the spherical wave spatial coherence length ρ_{sp} of 2.53mm. Again, the effects of aperture averaging are becoming more prevalent but will exaggerate as diameter is increased.

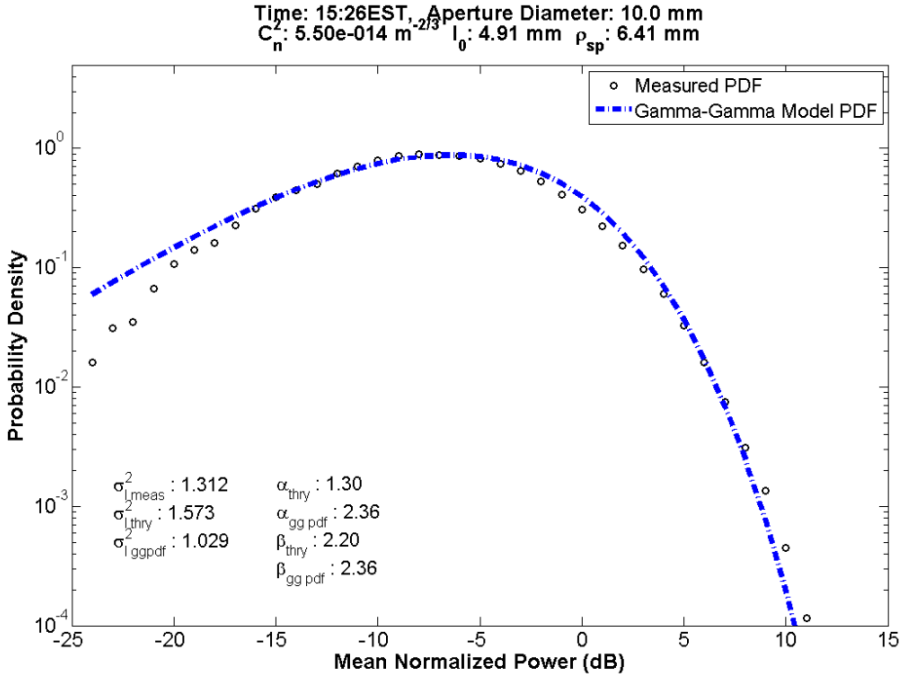

Figure 17: Experimental data PDF, 10.0mm aperture diameter.

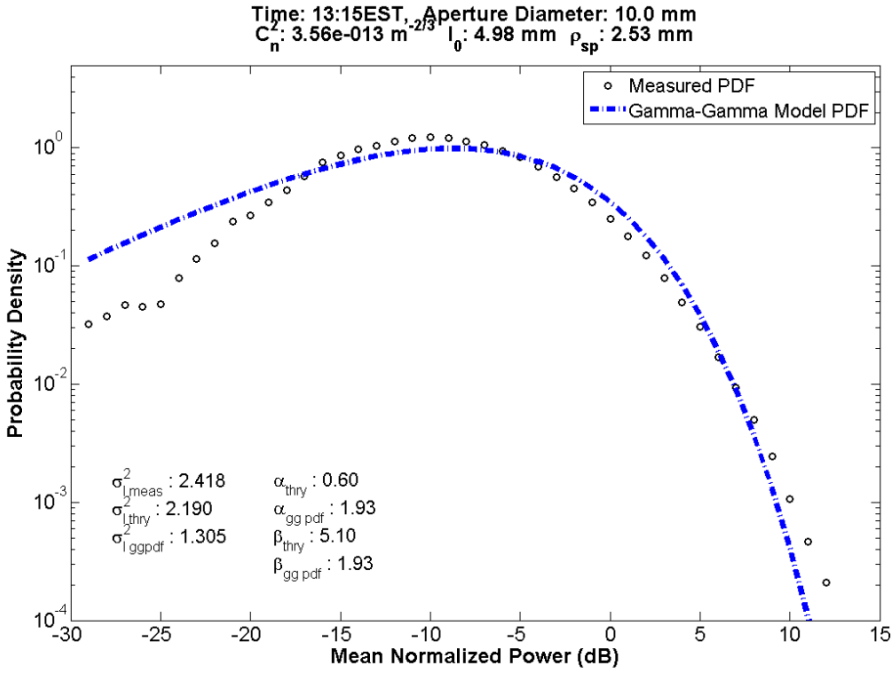

Figure 18: Experimental data PDF, 10.0mm aperture diameter.

The irradiance data collected with the 20.6mm aperture PDF data under weak turbulence is shown in Figure 19 (taken at 15:56EST) and a repeated measurement made at 15:21EST is shown in Figure 20. As before, the effect of increased turbulence is demonstrated with Figure 21 as the atmosphere at 13:11EST is slightly stronger than the 15:21EST and 15:56EST data collections.

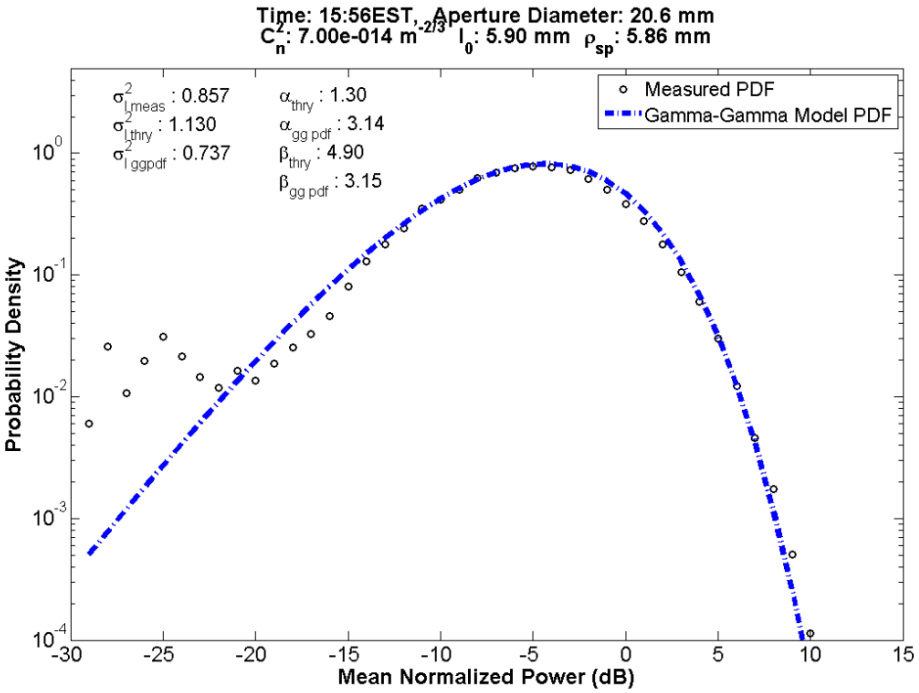

Figure 19: Experimental data PDF, 20.6mm aperture diameter

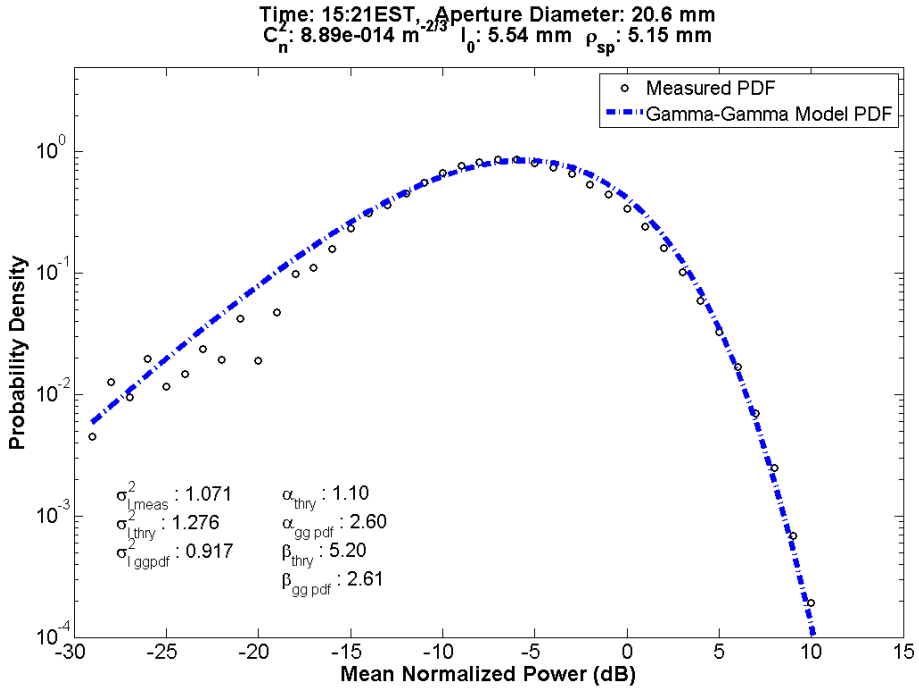

Figure 20: Experimental data PDF, 20.6mm aperture diameter.

The dynamic range of received irradiance fluctuations again appears to reduce as aperture size increases. In addition, it is observed the dynamic range of received irradiance fluctuations decreases as turbulence decreases. In these PDF measurements, the aperture diameter D of 20.6mm is significantly greater than the spherical wave spatial coherence length ρ_{sp} of about 5mm. As before, the aperture averaging condition relating aperture diameter D is spherical spatial coherence length ρ_{sp} is met ($D > 3\rho_{sp}$).

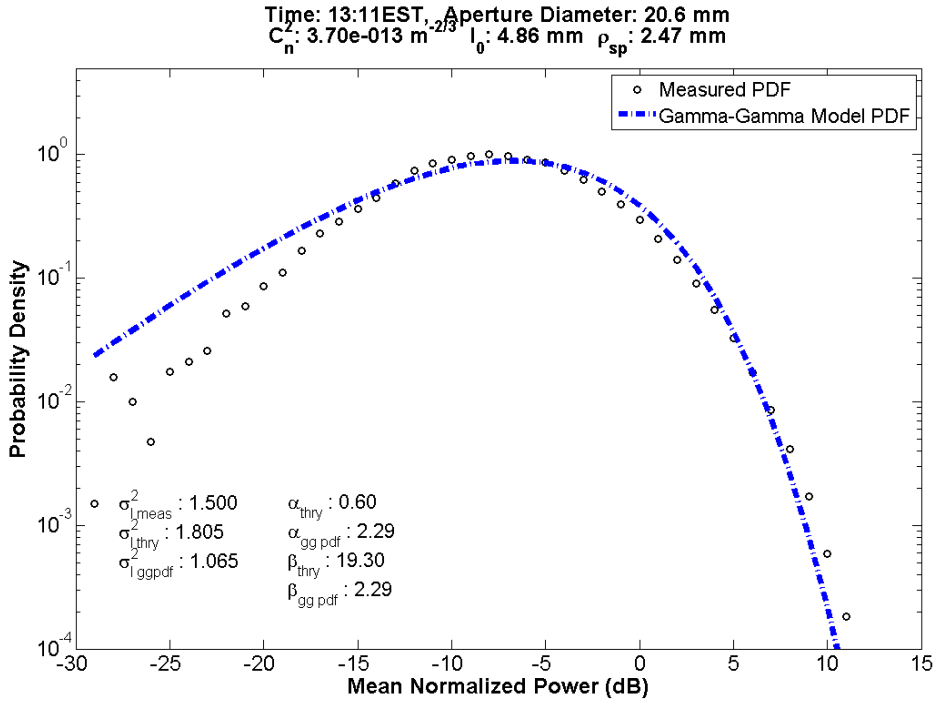

Figure 21: Experimental data PDF, 20.6mm aperture diameter.

The apertures presented in Figure 48, Figure 49, Figure 50, and Figure 51 are considerably larger than those previously presented (ranging 55mm and greater in diameter). With the increase in aperture size, it is expected that the gamma-gamma model parameter representing the number of small-scale scatterers β will become increasingly larger [10, 33, 34]. Additionally, atmospheric

turbulence during these collection times is somewhat moderate ($C_n^2 \sim 10^{-13}$). For these data collections, the spherical wave spatial coherence length ρ_{sp} ranges between 2-5mm. The apertures are all considerably larger than this length so one expects aperture averaging characteristics to be especially prevalent (the $D > 3\rho_{sp}$ condition is met).

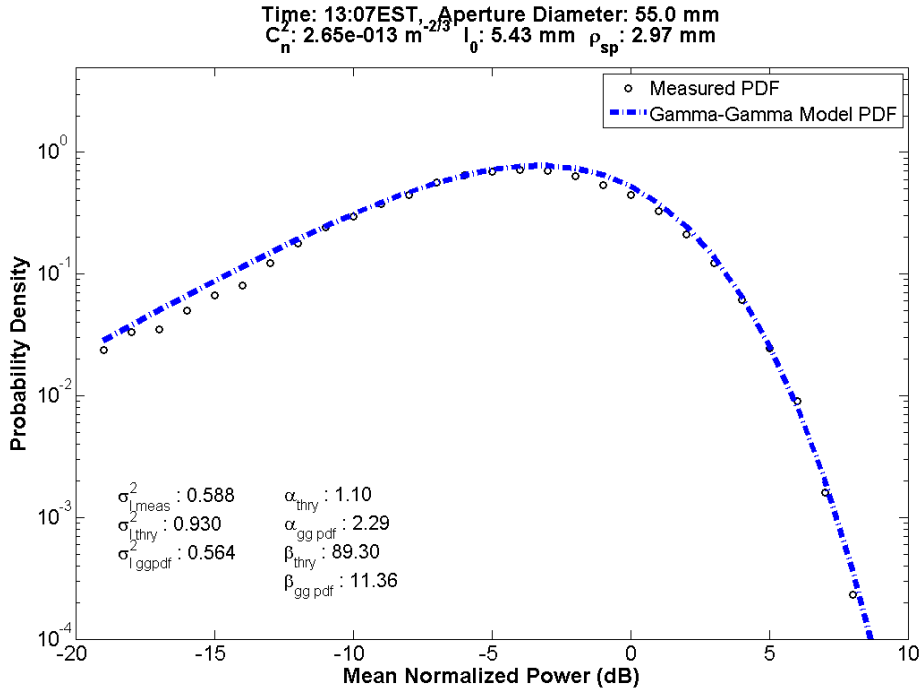

Figure 22: Experimental data PDF, 55.0mm aperture diameter.

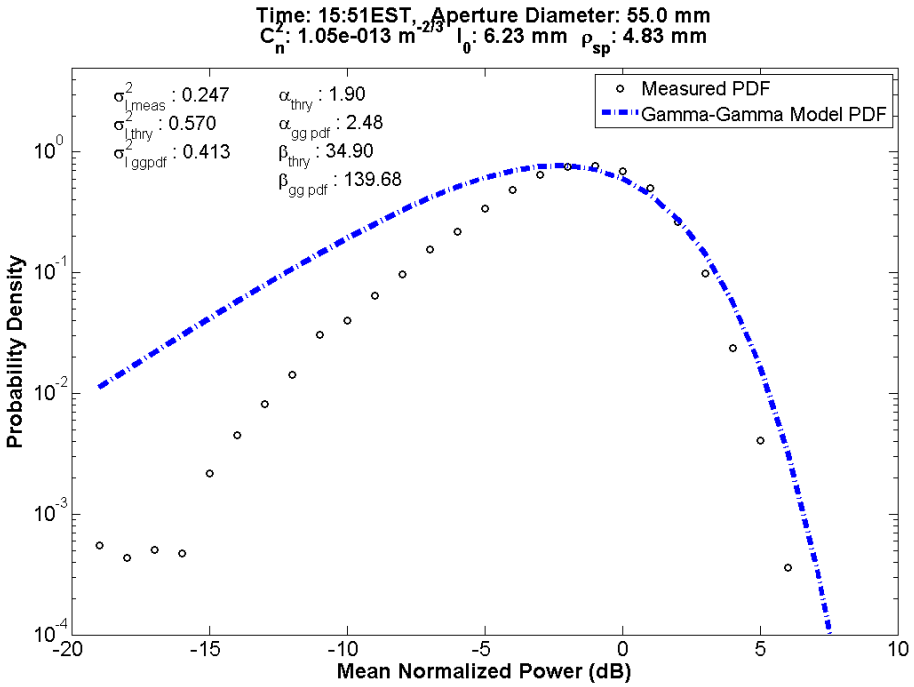

Figure 23: Experimental data PDF, 55.0mm aperture diameter.

The apertures presented in Figure 24 and Figure 25 display the most amount of aperture averaging. This can readily observed with the dynamic range of the received irradiance fluctuations, as it is only about 20dB wide. This is a considerable reduction when compared to the 40dB wide PDF seen with the smaller apertures such as in Figure 15: Experimental data PDF, 4.0mm aperture diameter.

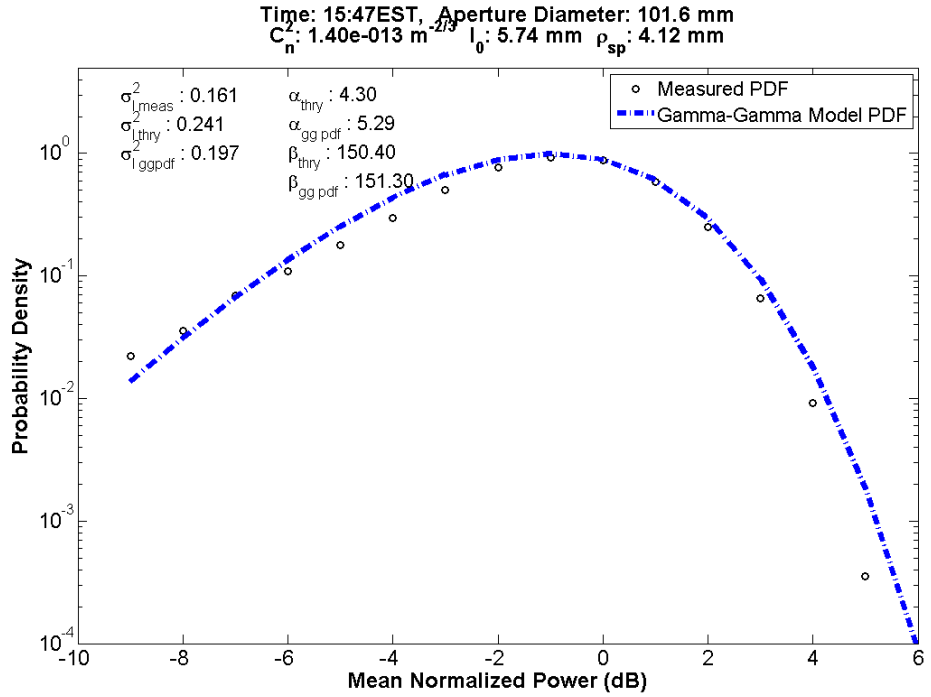

Figure 24: Experimental data PDF, 101.6mm aperture diameter.

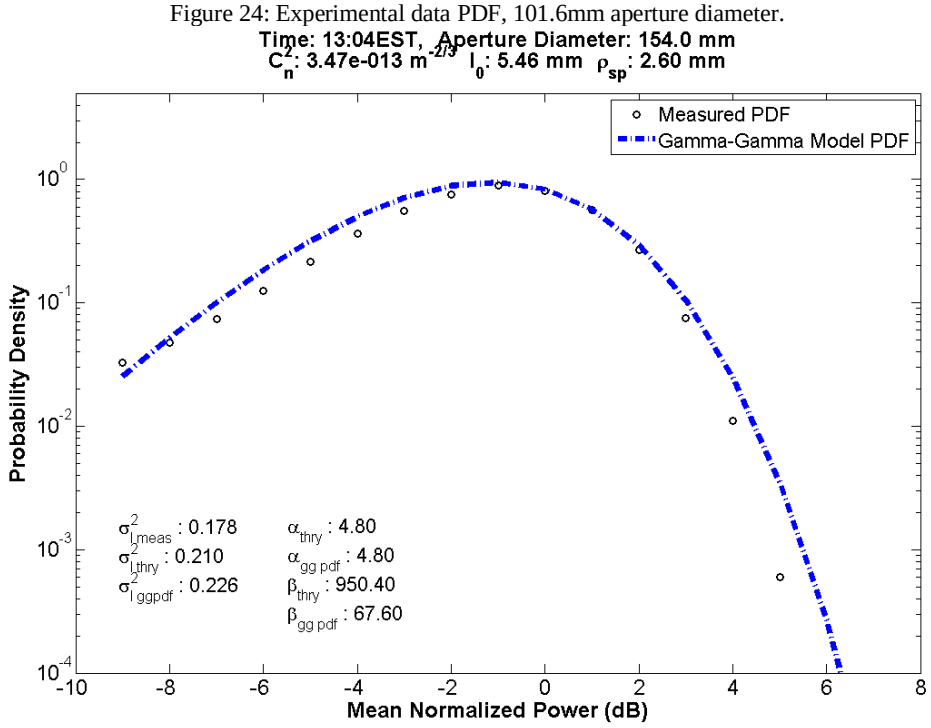

Figure 25: Experimental data PDF, 154.0mm aperture diameter.

Irradiance data collected and presented match the gamma-gamma model to a satisfactory extent. This is expected as previous results and models have confirmed these results [7, 13]. The focus of the following sections will involve analysis of irradiance threshold fading within the data segments used to compute PDF measurements.

4.4.2 Mean Number of Level Crossings of Experimental Data

In this section the experimental data are compared with the gamma-gamma mean number of level crossings model. Level crossings are counted in terms of fades per second. Fades per second is essentially one half the number of level crossings per second, as the signal must traverse the threshold level once to be considered faded and traverse the threshold level once more to come out of the fade. The analysis to calculate the level crossing rate is summarized in Section 3.2.1 Mean Level Crossing Rate, and in Section 3.4.1 Mean Level Crossing Rate of Gamma-Gamma Distributed Irradiance. Overall, data presented is shown to compare well with the data and analysis seen in the literature [7, 10, 13, 34, 45]. The calculated gamma-gamma parameter values and the best-fit gamma-gamma mean number of level crossing parameter values are tabulated in Table 3. Note that the value of $\beta_{gg\ meanfd}$ is capped at 50 for the last three collections shown in Table 3 due to numerical stability because $\alpha_{gg\ meanfd}$ is also slightly greater. This allows for the plots to be reliably generated via an automated scheme.

Table 3: Summary of gamma-gamma mean fade model data

Aperture Size (mm)	$\alpha_{gg\ meanfd}$	$\beta_{gg\ meanfd}$	$\sigma^2_{I\,gg\ meanfd}$	α_{thry}	β_{thry}	$\sigma^2_{I\,thry}$	$\sigma^2_{I\,meas}$	Time EST
1.5	1.19	1.36	2.194	1.40	1.60	1.786	1.296	16:01
4.0	1.95	2.25	1.185	0.90	1.30	2.735	2.253	15:32
4.0	1.95	2.25	1.185	0.90	1.30	2.735	1.934	16:19
7.0	2.50	2.55	0.949	1.00	1.70	2.176	1.820	16:15
10.0	2.71	3.30	0.784	1.30	2.20	1.573	1.312	15:26
10.0	1.50	7.65	0.885	0.60	5.10	2.190	2.418	13:15
20.6	2.83	7.35	0.537	1.30	4.90	1.130	0.857	15:56
20.6	2.26	7.80	0.627	1.10	5.20	1.276	1.071	15:21
20.6	1.50	28.95	0.724	0.60	19.30	1.805	1.500	13:11
55.0	2.39	133.95	0.429	1.10	89.30	0.930	0.588	13:07
55.0	2.86	50.0	0.377	1.90	34.90	0.570	0.247	15:51
101.6	6.76	50.0	0.171	4.30	150.40	0.241	0.161	15:47
154.0	5.80	50.0	0.196	4.80	950.40	0.210	0.178	13:04

Considering that the mean value of the irradiance signal is held constant (which will automatically happen for a mean-normalized irradiance signal), we generally expect the number of fades per second to reduce as the irradiance threshold parameter I_T decreases well beyond the mean irradiance value [10, 33, 34]. A decrease in irradiance threshold parameter I_T is equivalent to an increase in the fade threshold parameter F_T. The initial increase in fades per second with the low values of F_T (3dB of less) is contributed to by the characteristics of the gamma-gamma PDF irradiance model. Generally speaking it is in this range when the fades per second decrease

because the irradiance threshold I_T is approaching the mean irradiance value $\langle I \rangle$, and the PDF of irradiance signal is heavily weighted toward the lower irradiance values (Section 4.4.1 PDF of Experimental Data) [7, 13]. Therefore when analyzing larger irradiance thresholds I_T it is more probable for a signal to fade, and stay in a faded state, as opposed to returning back above the irradiance threshold.

As discussed in Section 3.2.1 Mean Level Crossing Rate, the gamma-gamma mean fade model requires three shape parameters; the large-scale scattering parameter α, the small-scale scattering parameter β, and the quasi frequency ν_0. These parameters will be denoted in the data presented for mean fade time characterization as $\alpha_{gg\ meanfd}$, $\beta_{gg\ meanfd}$, and $\nu_{gg\ meanfd}$. Once again, the scintillation index σ_I^2 can be calculated from the large-scale and small-scale scattering parameters using Equation (3.20) and this is presented as $\sigma_{I\ ggmeanfd}^2$ for the mean fade time analysis.

Analysis of the data again starts with the smallest of the apertures, 1.5mm. The minimum aperture scenario represents the minimum SNR for this experiment therefore making measurements somewhat difficult in stronger atmospheric-turbulence [7]. As stated in 4.4.1 PDF of Experimental Data, data presented for the 1.5mm aperture were recorded under somewhat benign atmospheric conditions ($C_n^2 \sim 10^{-14}$) to allow for a better estimation of the probability density function. The trend in the data presented for the 1.5mm aperture in Figure 26 fits the expected, with the number of fades per second showing a decrease as fade threshold parameter reaches its maximum value. The PDF of the irradiance for the 1.5mm aperture was demonstrated

to be the largest in dynamic range of irradiance as in Figure 13. It is noted here that the gamma-gamma mean fade time model predicts a larger scintillation index for the received irradiance than what is measured. Indeed the calculated value of $\sigma^2_{I\,thry} = 1.786$ is not drastically larger than $\sigma^2_{I\,ggmeanfd} = 2.194$ however is enough of a difference to take note of and this can likely be attributed to minimization difficulty.

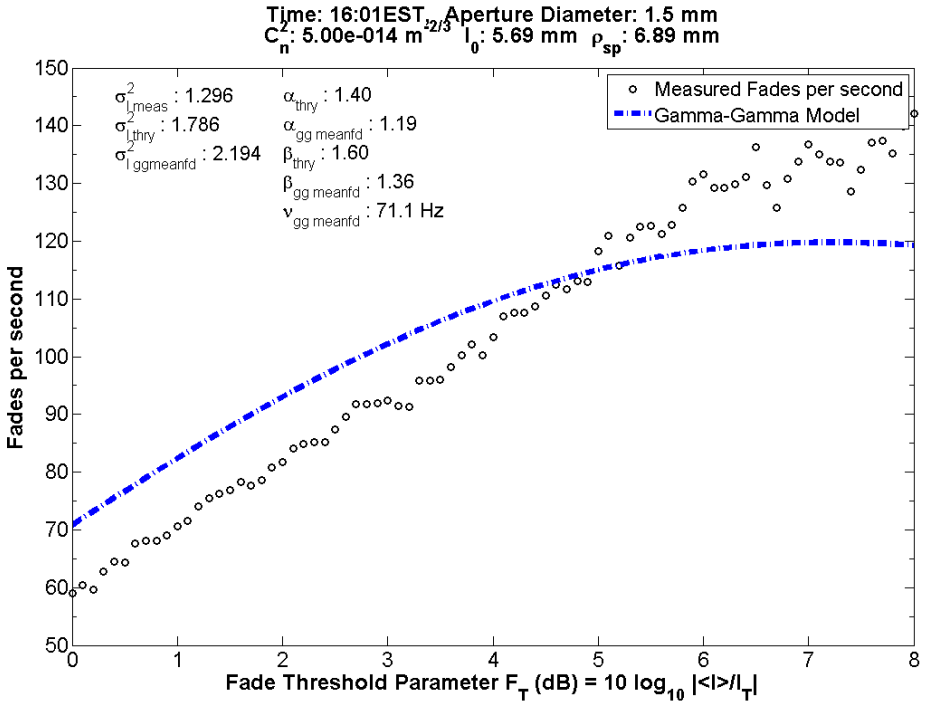

Figure 26: Experimental data mean number of fades per second, 1.5mm aperture diameter.

The results obtained for the 4mm aperture are shown in Figure 27 and Figure 28. As discussed in Section 4.4.1 PDF of Experimental Data, the apertures where $D < \rho_{sp}$ exhibits the scenario where we would expect minimal aperture averaging. As aperture size is increased, fade time statistics will begin to change as the PDF changes. Typically $D > 3\rho_{sp}$ indicates that there will

be a large amount of aperture averaging present, and the PDF of received irradiance will reflect this aspect [7, 13]. This will cause for an increase in the number of fades seen when F_T is small, and decrease the number of fades when F_T is large.

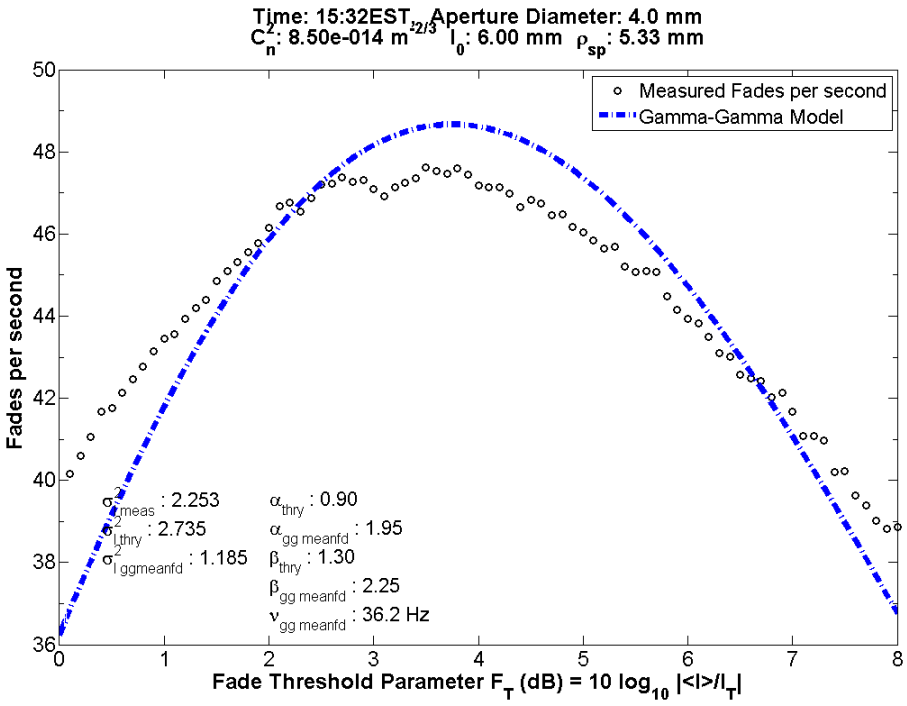

Figure 27: Experimental data mean number of fades per second, 4.0mm aperture diameter.

It is noted that, in both 4mm aperture plots, the scintillation index calculated from the gamma-gamma mean fade time model is noticeably smaller than what is experimentally measured. Turbulence was semi-moderate during the collection of 4mm aperture data ($\sim 10^{-13}$). The scintillation index becomes somewhat sensitive to changes in α and β as these scattering parameters become small. It is postulated that this is the mean factor in contributing to this error, as the parameters themselves seem somewhat accurate and representative of collected data. It

will be shown in the mean fade plots for larger apertures that the gamma-gamma mean fade model scintillation index follows experimental data to a better extent.

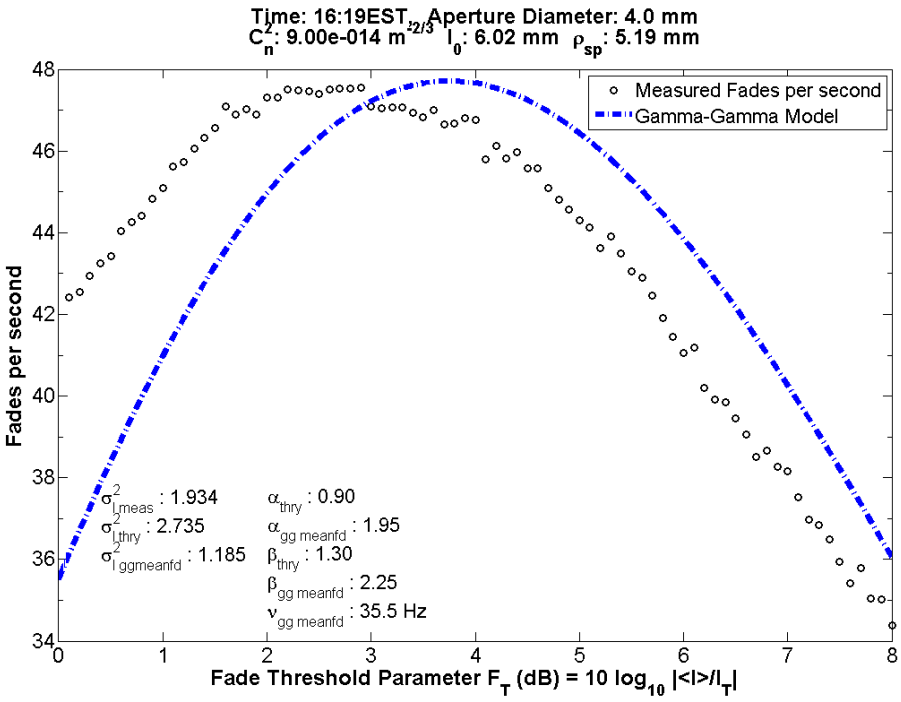

Figure 28: Experimental data mean number of fades per second, 4.0mm aperture diameter.

As aperture size is increased to 7mm, similar trends are observed as with the two smaller apertures. Figure 29 shows the data collected under very similar conditions as the 4mm data with C_n^2 being about 10^{-13} in magnitude. The aperture diameter D is beginning to exceed the spatial coherence length ρ_{sp} but aperture averaging effects are not yet immediately obvious. Again, the scintillation index predicted with the gamma-gamma mean fade model does not quite match with the experimentally measured scintillation index. The best fit to experimental data gamma-gamma model parameters $\alpha_{gg\ meanfd}$ and $\beta_{gg\ meanfd}$ exhibit a fair amount of agreement with the theoretically obtained gamma-gamma model parameters α_{thry} and β_{thry}. The mismatch in

theoretically predicted and best fit scintillation index can be attributed to the sensitivity in gamma-gamma modeled scintillation index to small values of α and β [7].

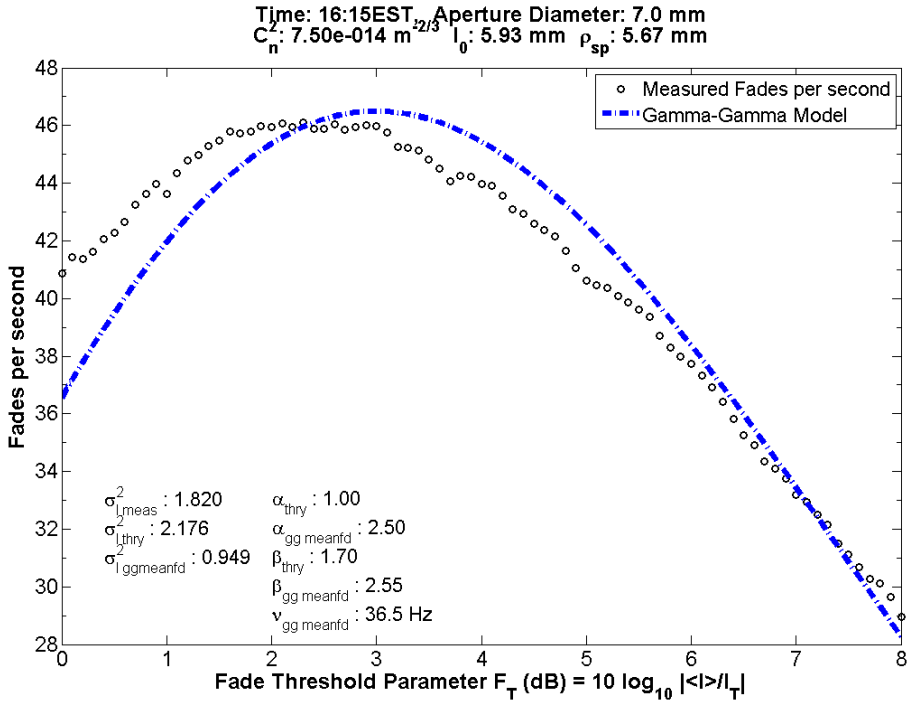

Figure 29: Experimental data mean number of fades per second, 7.0mm aperture diameter.

Figure 30 demonstrates the 10mm aperture data collection under relatively weaker turbulence ($C_n^2 \sim 10^{-14}$), and Figure 31 shows the 10mm aperture data collection under slightly stronger turbulence ($C_n^2 \sim 10^{-13}$). It is observed that there does not a significant difference in the three 10mm aperture data collections when analyzing mean fade statistics. At this point, aperture averaging effects are beginning to be observed as the curve exhibits a steeper roll off as F_T is increased when compared with mean number of fade plots for the smaller aperture. However, the effects are not yet as demonstrative as is the case with larger apertures where $D > 3\rho_{sp}$.

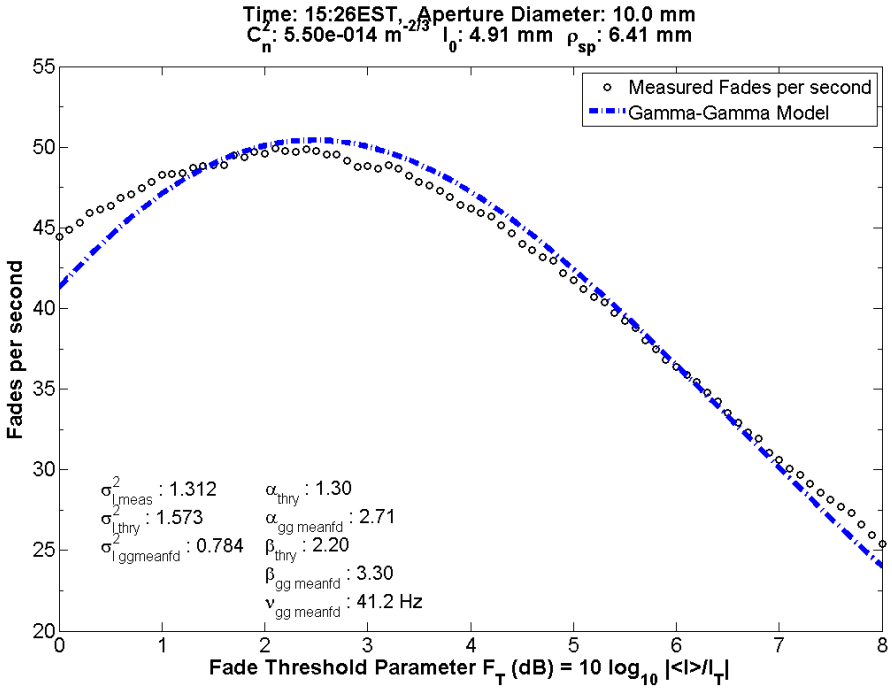

Figure 30: Experimental data mean number of fades per second, 10.0mm aperture diameter.

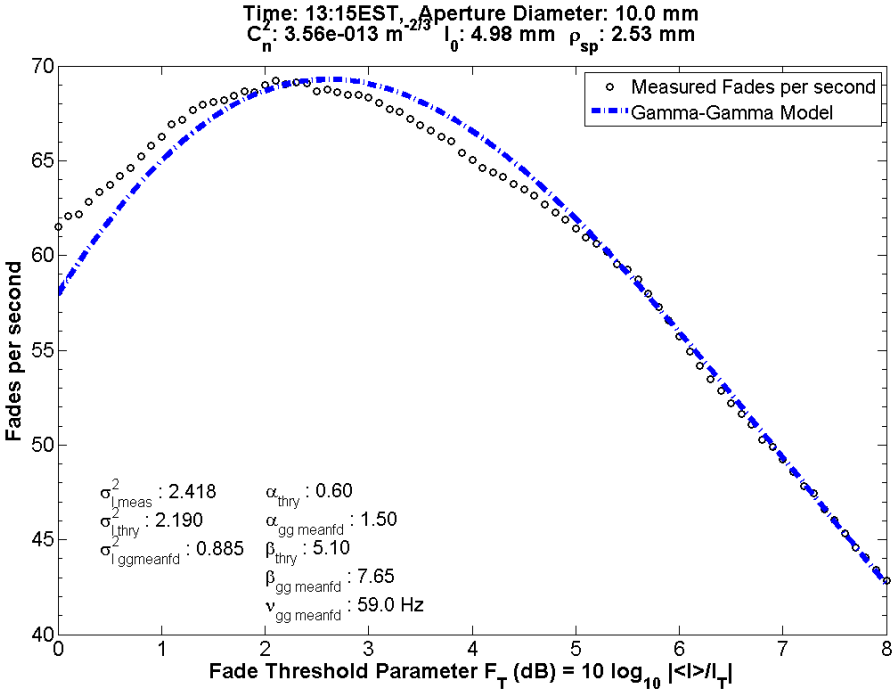

Figure 31: Experimental data mean number of fades per second, 10.0mm aperture diameter.

We will next look into the 20.6mm aperture data collected under conditions of semi-moderate turbulence ($C_n^2 \sim 10^{-13}$). Spatial coherence length ρ_{sp} is exceeded by aperture diameter D by more than three times and we expected aperture averaging effects to be more prevalent in the received irradiance data ($D > 3\rho_{sp}$). The data collected with the 20.6mm is shown in Figure 32, Figure 33, and Figure 34. As seen in the plots, data appear to be similar to the smaller aperture plots however with a steeper roll off at larger values of F_T. Additionally, the plots exhibit a flatter roll off at the lower values of F_T. It will be seen that this trend continues as the aperture diameter is further increased.

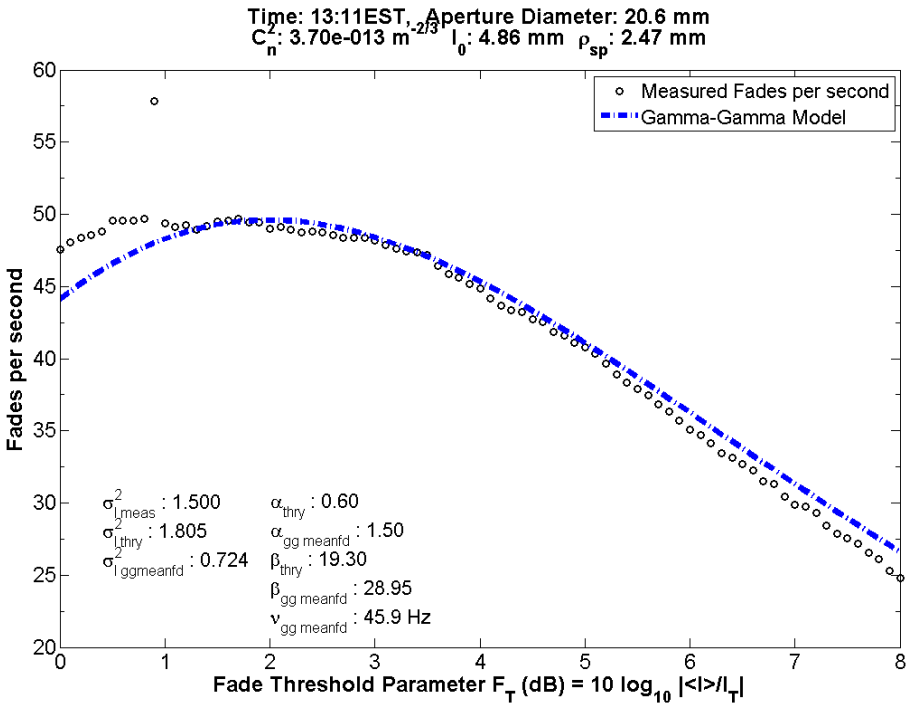

Figure 32: Experimental data mean number of fades per second, 20.6mm aperture diameter.

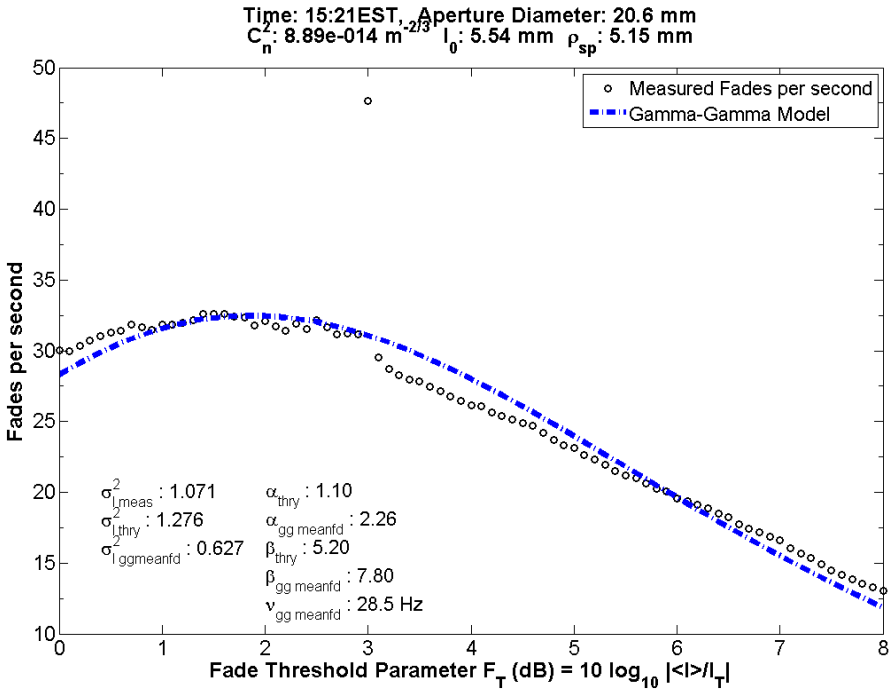

Figure 33: Experimental data mean number of fades per second, 20.6mm aperture diameter.

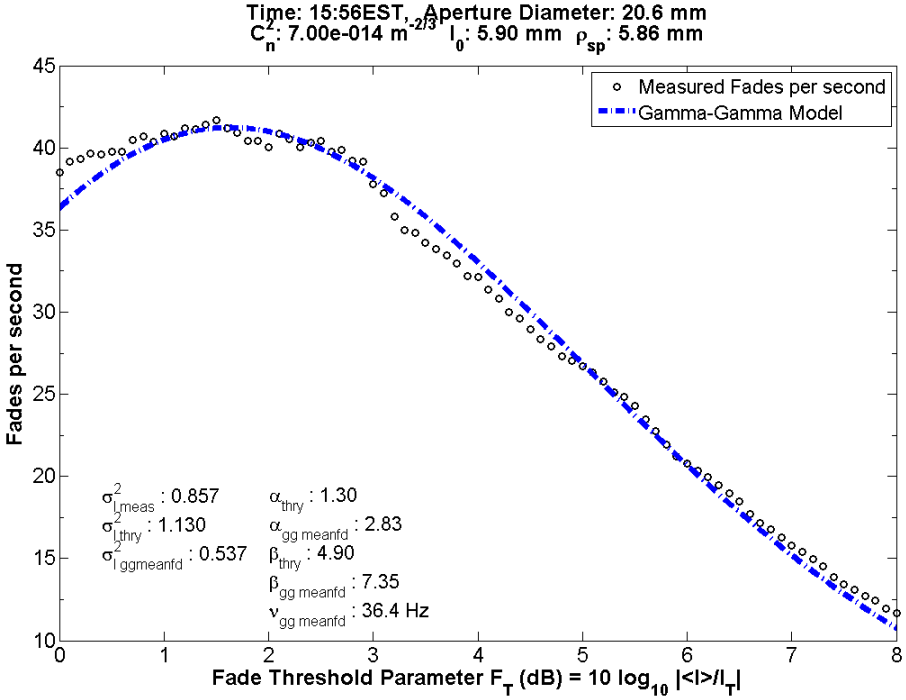

Figure 34: Experimental data mean number of fades per second, 20.6mm aperture diameter.

We last analyze the larger set of apertures consisting of the 55mm, 101.6mm, and 154mm aperture diameter data collections. In these cases, the spatial coherence length ρ_{sp} is much smaller than these aperture diameters (with the $D > 3\rho_{sp}$ condition is met) therefore signifying that a strong influence of aperture averaging will be present. From the gamma-gamma irradiance PDF, that the gamma-gamma small-scale scattering parameter is much larger and therefore scintillation index is less sensitive to its exact value. This is demonstrated in the modeled and compared values of α and β. We that find the measured scintillation index $\sigma_{I\,meas}^2$ and the theoretically inferred scintillation index $\sigma_{I\,thry}^2$ agree with the modeled gamma-gamma mean fade time scintillation index $\sigma_{I\,gg\ meanfd}^2$.

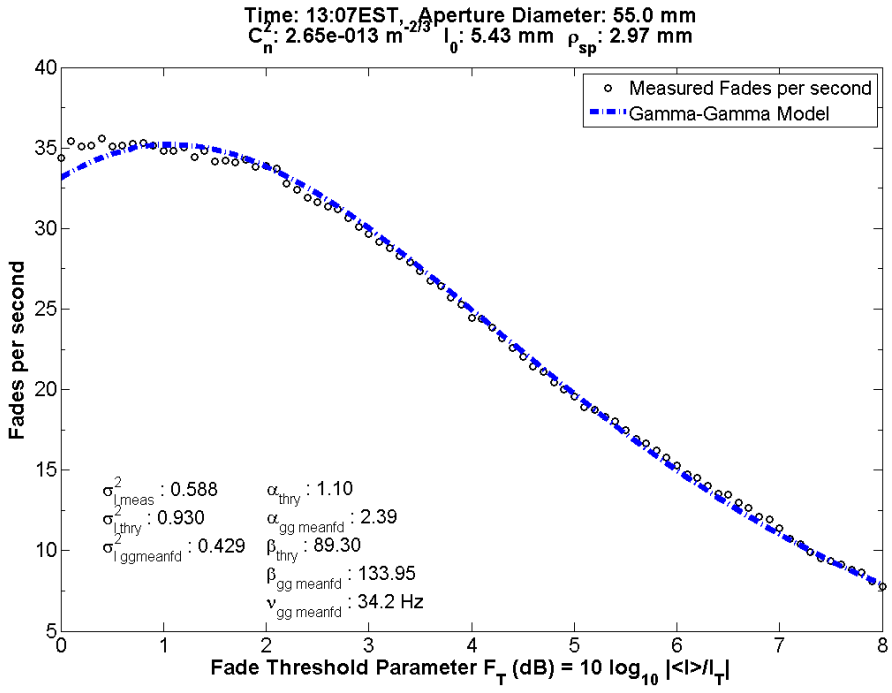

Figure 35: Experimental data mean number of fades per second, 55.0mm aperture diameter.

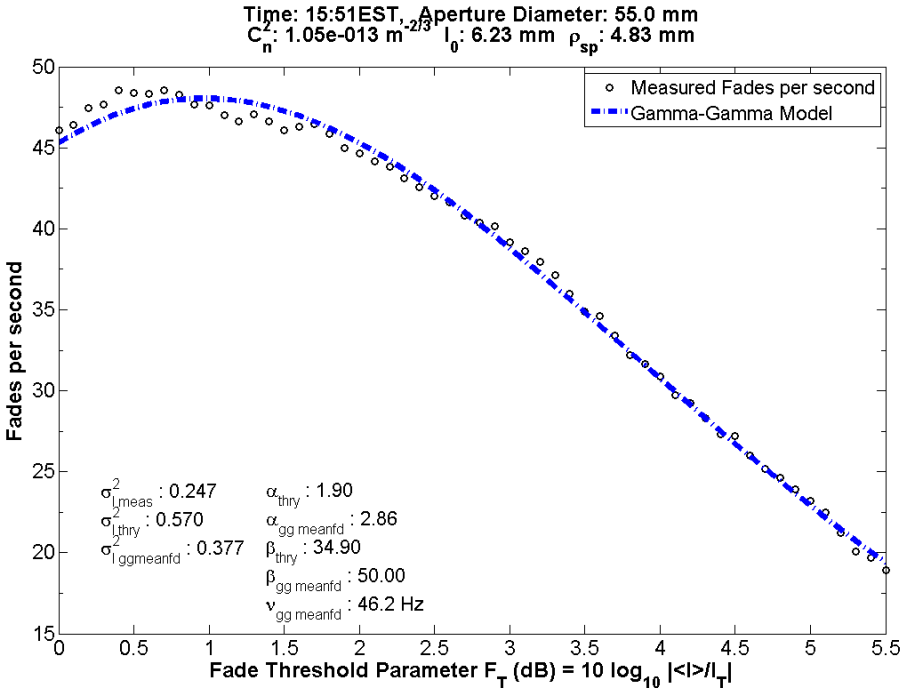

Figure 36: Experimental data mean number of fades per second, 55.0mm aperture diameter.

The data for these collections is presented from Figure 35 to Figure 38. Atmospheric turbulence is about the same in these four plots, with $C_n^2 \sim 10^{-13}$ denoting semi-moderate turbulence conditions. Again, these curves exhibit a stronger roll off as F_T is increased, and tend to become more flat as F_T is decreased.

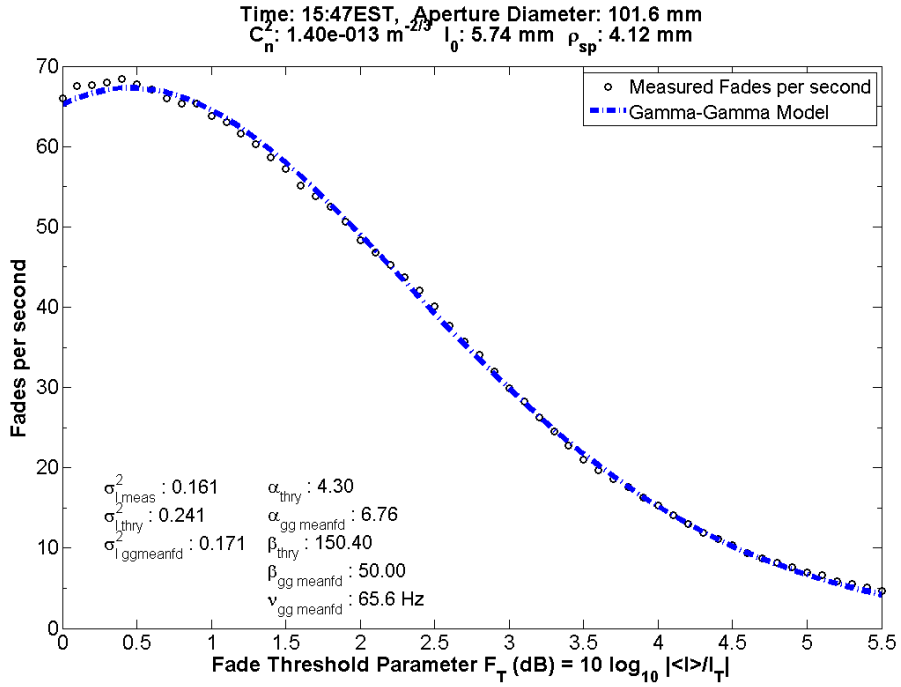

Figure 37: Experimental data mean number of fades per second, 101.6mm aperture diameter.

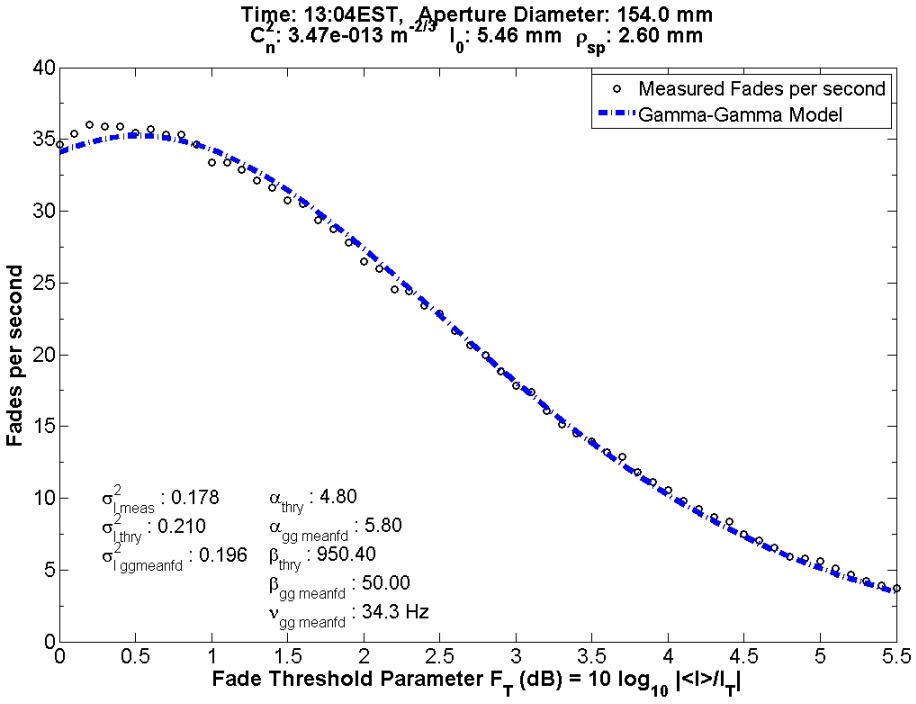

Figure 38: Experimental data mean number of fades per second, 154.0mm aperture diameter.

4.4.3 Mean Fade Time of Experimental Data

This section examines mean fade time statistics of the data collected at the ISTEF range. The previously developed expression in Equation (3.67) of Section 3.4.1 will be utilized. The results presented in this section burrow heavily from the results in Section 4.4.2 Mean Number of Level Crossings of Experimental Data and those presented in 4.4.1 PDF of Experimental Data. The interplay between mean number of level crossings and the cumulative distribution function (CDF) given in Equation (3.46). As stated in the analysis for the mean number of level crossings, it is expected that the number of fades per second will decrease at the fade threshold parameter F_T is increased. This will remain true for mean fade time, as one would expect the fade time to decrease as the irradiance threshold level I_T is decreased. Additionally, as aperture size is increased well beyond the spatial coherence length ($D > 3\rho_{sp}$) the fade-time should exhibit a trend in decrease [10, 33, 34].

The results shown from Figure 39 to Figure 51 confirm these notions. Placed again for convenience, the calculated parameters are shown in Table 3: Summary of gamma-gamma mean fade model data.

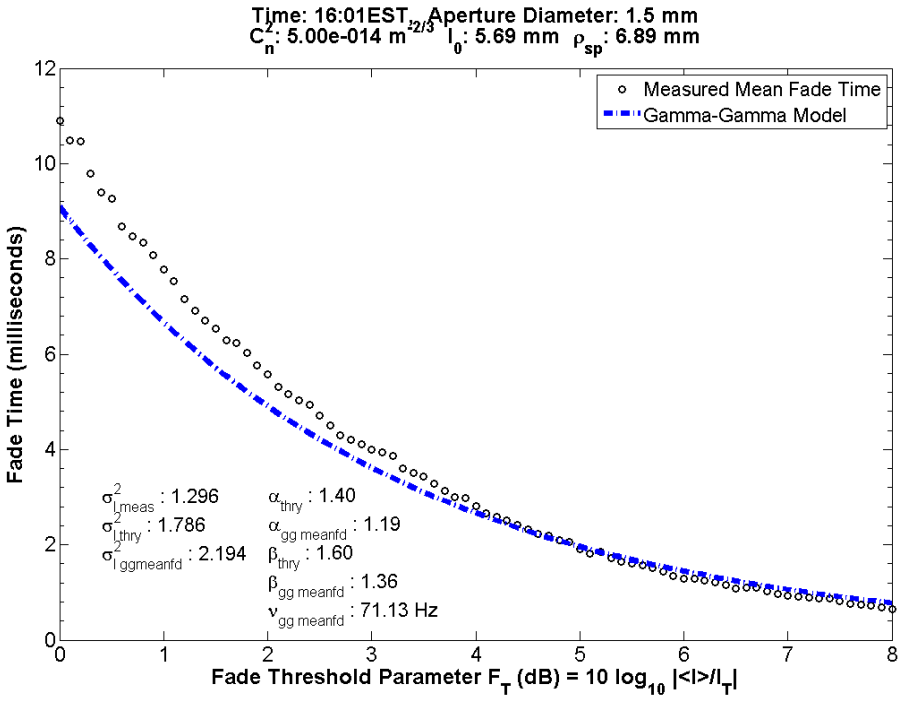

Figure 39: Experimental data mean fade time, 1.5mm aperture diameter.

The mean fade time data for the 1.5mm aperture are presented in Figure 39. In the plots for the smaller apertures we will see the mean fade curve exhibiting a slower roll off when compared to the plots for larger apertures. The effect of aperture averaging on this roll off is inherent from the PDF plots shown in Section 4.4.1 PDF of Experimental Data. It will be noted from data collection that the smaller apertures as exhibit a somewhat larger mean fade time at lower values of F_T.

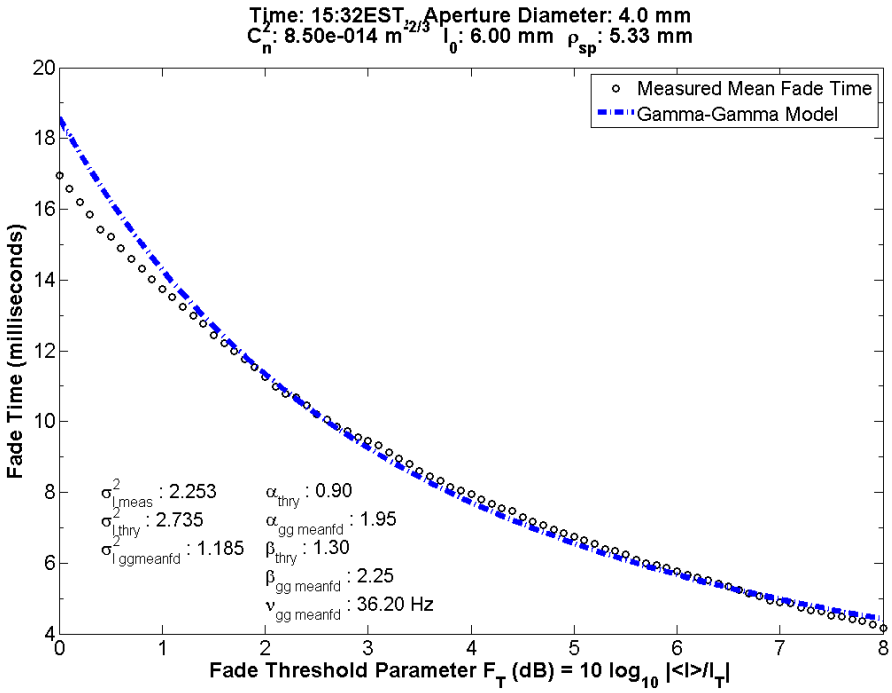

Figure 40: Experimental data mean fade time, 4.0mm aperture diameter.

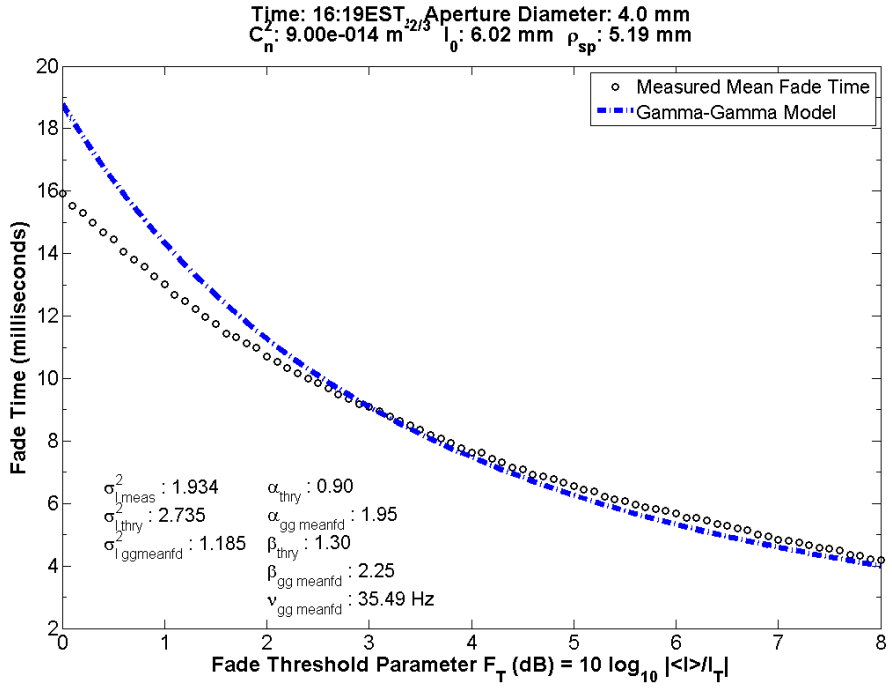

Figure 41: Experimental data mean fade time, 4.0mm aperture diameter.

The plots shown in Figure 40 to Figure 44 show the mean fade time data collected for the middle-sized apertures. Here the curve roll off is becoming slightly greater than what is shown for the smaller apertures.

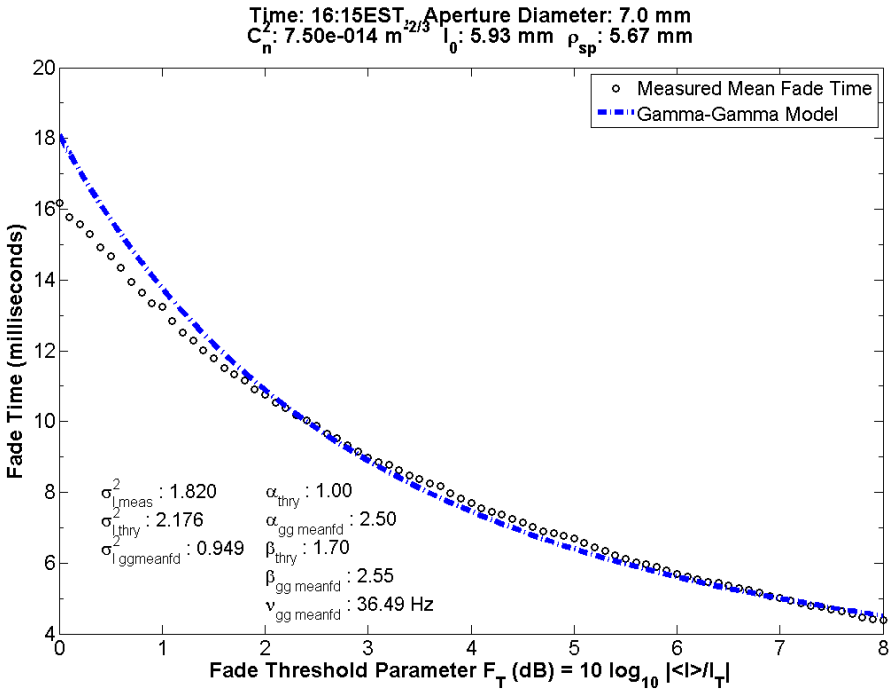

Figure 42: Experimental data mean fade time, 7.0mm aperture diameter.

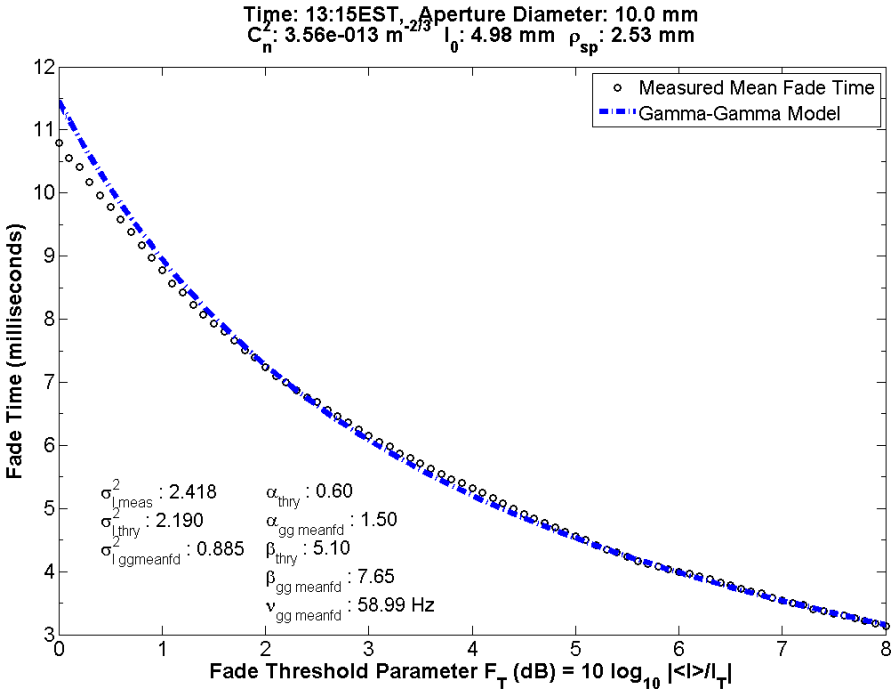

Figure 43: Experimental data mean fade time, 10.0mm aperture diameter.

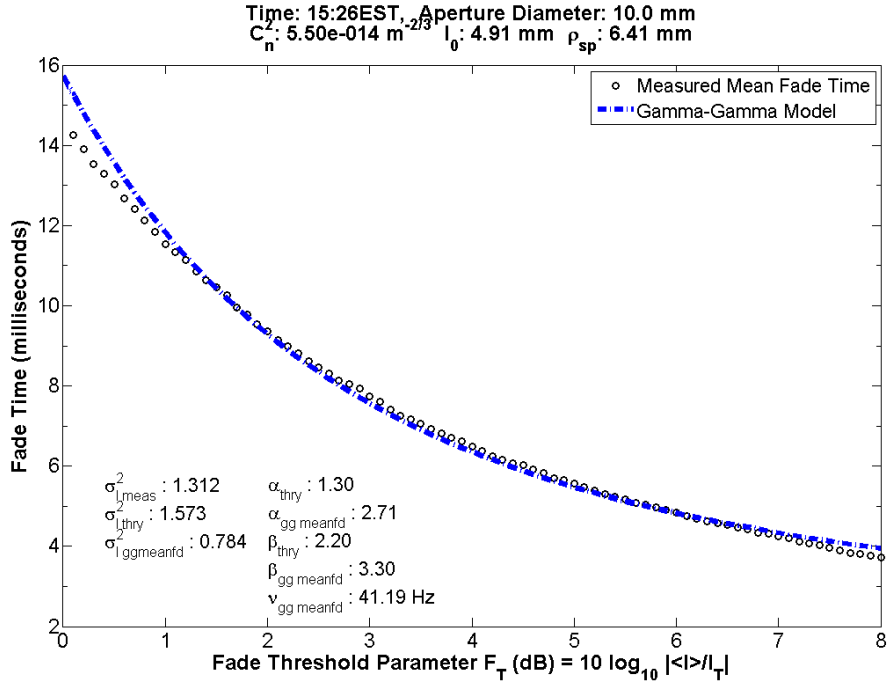

Figure 44: Experimental data mean fade time, 10.0mm aperture diameter.

The plots shown in Figure 45, Figure 46 and Figure 47 demonstrate the mean fade time data collected with the 20.6mm aperture. As aperture diameter gets much greater than the spatial coherence length ρ_{sp} (more than three times greater in this case), the mean fade time begins to decrease more rapidly with an increase of F_T.

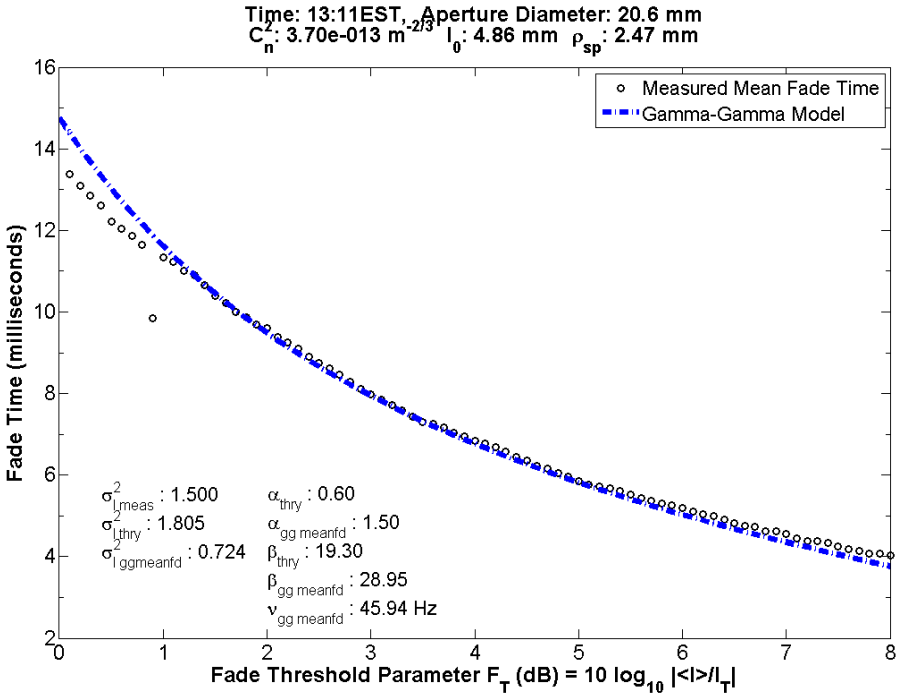

Figure 45: Experimental data mean fade time, 20.6mm aperture diameter.

This effect can be subtle to note as the mean fade time data itself presents variance. For this reason, the mean fade time plots are postulated to not be a tell-all of fade-statistics. It will be with coordination of Section 4.4.5 Standard Deviation of Fade Time of Experimental Data that an understanding of fade characteristics will be developed.

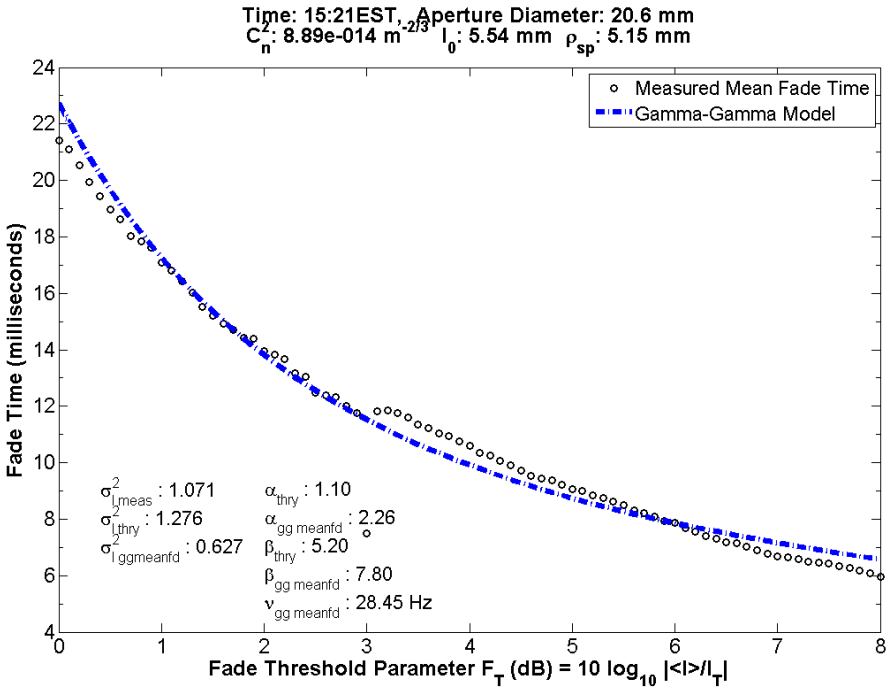

Figure 46: Experimental data mean fade time, 20.6mm aperture diameter.

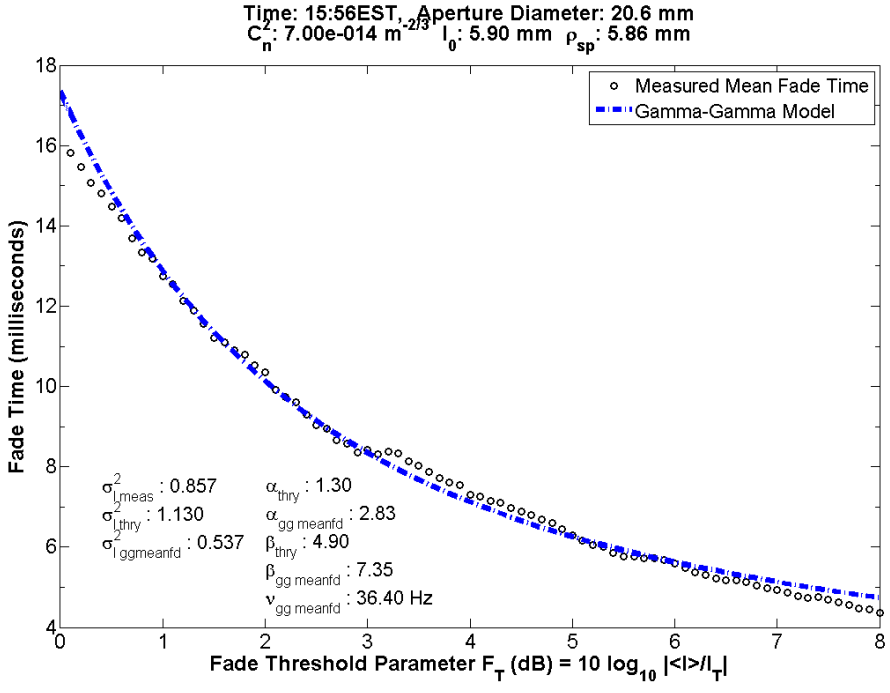

Figure 47: Experimental data mean fade time, 20.6mm aperture diameter.

The 55mm aperture diameter data is presented in Figure 48 and Figure 49. These plots exhibit a larger value for the gamma-gamma small-scale parameter β when compared to the smaller diameters. The exact effect of this parameter on the overall shape of the gamma-gamma average fade time curve in this case may be difficult to discern given the additional presence of the inferred quasi-frequency term $\nu_{gg\ meanfd}$.

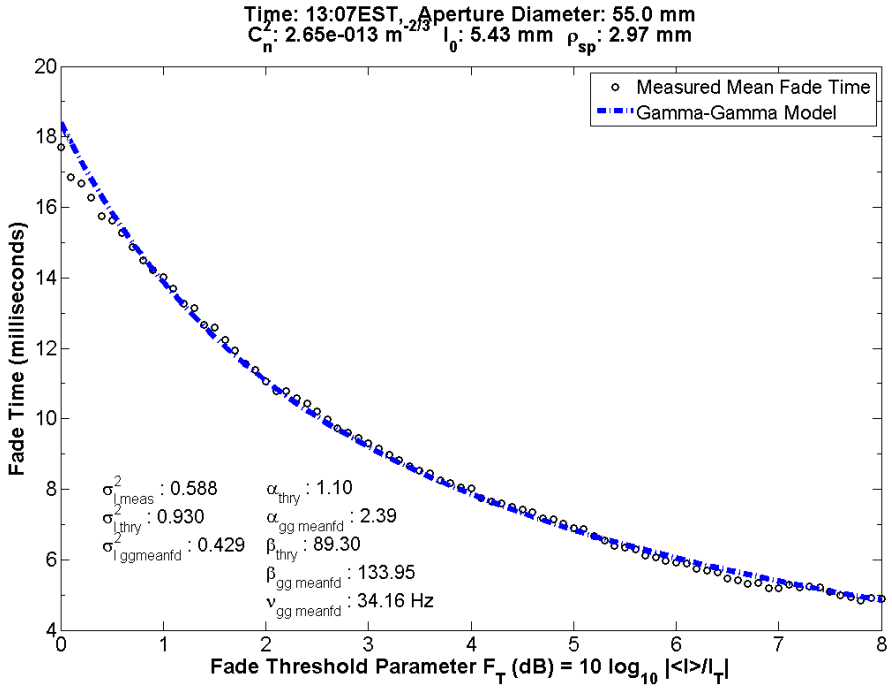

Figure 48: Experimental data mean fade time, 55.0mm aperture diameter.

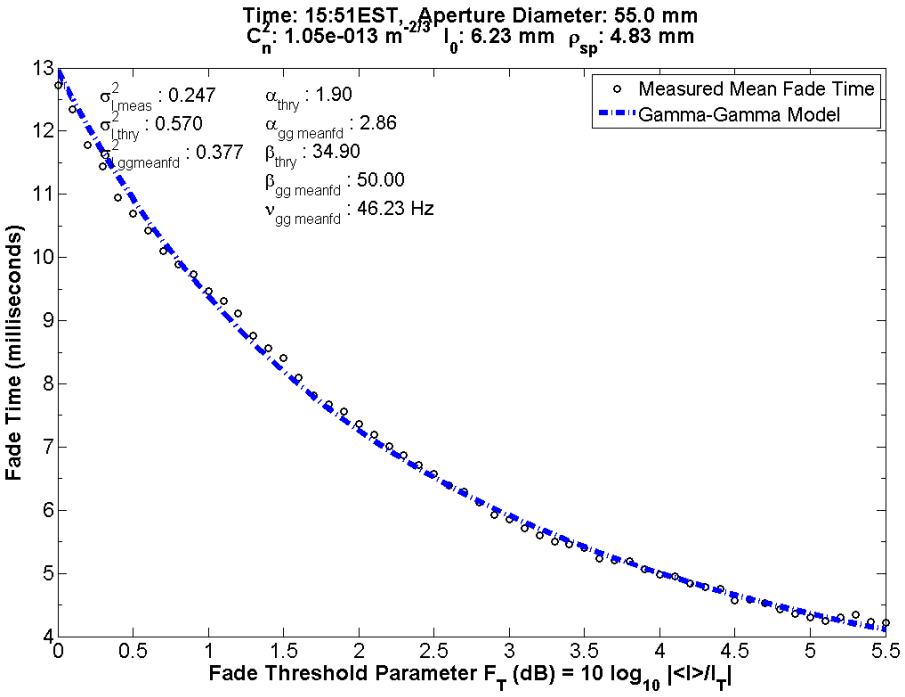

Figure 49: Experimental data mean fade time, 55.0mm aperture diameter.

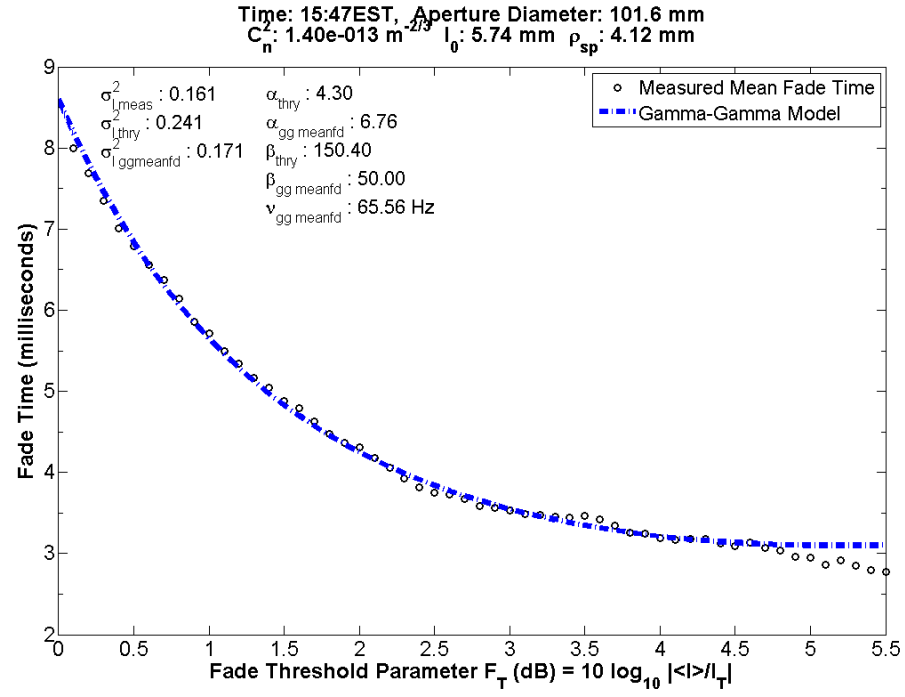

Figure 50: Experimental data mean fade time, 101.6mm aperture diameter.

Last presented is the mean fade time data for the 154mm aperture. Figure 51 shows the plot of the data, and we again note the large value of β that is present.

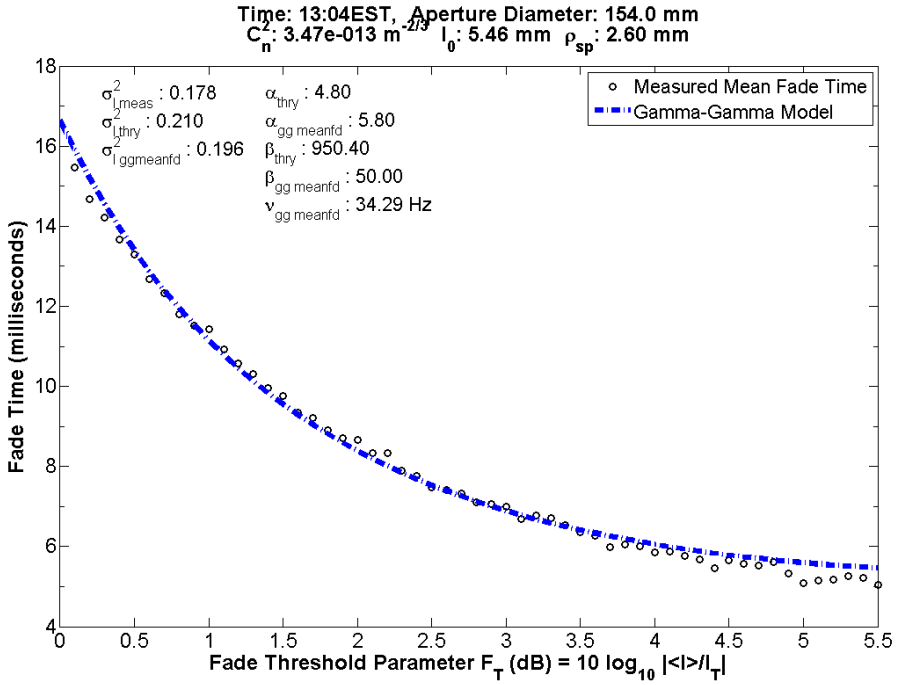

Figure 51: Experimental data mean fade time, 154.0mm aperture diameter.

Data agree reasonably well with the theoretical model for the various sized apertures. The dependence on aperture diameter implies a more appropriate model should be utilized to encompass the aperture averaging effects when analyzing irradiance threshold fades.

4.4.4 Mean Square Number of Level Crossings of Experimental Data

The developed theoretical expressions for the mean square number of level crossings of a gamma-gamma distributed irradiance signal will be compared with the experimental data collected at the ISTEF range. Mean square number of level crossings per second are presented, and compared with the newly developed theory from Section 3.4.2 Mean Square Level Crossing Rate of Gamma-Gamma Distributed Irradiance. The expression derived in Equation (3.87) will

be utilized, and compared with the experimental results for the various aperture sizes. The behavior of the developed gamma-gamma mean square number of crossings expression is based heavily upon the same expressions as the mean number of crossings. As such, it is expected that the shape of the mean square crossing curves will remain somewhat similar to the average crossing curves.

As with the gamma-gamma PDF and mean fade time models, the gamma-gamma model parameters will be found by a best fit to data. We will use $\alpha_{gg\ msq}$ and $\beta_{gg\ msq}$ to denote the respective mean square gamma-gamma model parameters. With the model parameters, a scintillation index σ_I^2 may be developed with Equation (3.20) to be

$$\sigma_{I\,gg\ msq}^2 = \left(1 + \frac{1}{\alpha_{gg\ msq}}\right)\left(1 + \frac{1}{\beta_{gg\ msq}}\right) - 1. \tag{4.7}$$

As before, both the modeled parameters and the scintillation index will be compared for apertures of different size. We expect that as aperture size increases, the additional averaging will attribute to a reduction in signal fluctuation. The exact effects of aperture averaging on mean square number of level crossings may be out of the scope of this analysis with consideration that the gamma-gamma irradiance PDF model is not heavily based upon aperture averaging. This however does not stop one from investigating such effects in determination of model parameters. A summary of the gamma-gamma mean square fade time parameters is given in Table 4, and presented alongside the experimentally measured parameters.

Table 4: Summary of gamma-gamma mean fade model data

Aperture Size (mm)	$\alpha_{gg\ msq}$	$\beta_{gg\ msq}$	$\sigma^2_{I\ gg\ msq}$	α_{thry}	β_{thry}	$\sigma^2_{I\ thry}$	$\sigma^2_{I\ meas}$	Time (EST)
1.5	0.68	8.42	1.775	1.40	1.60	1.786	1.296	16:01
4.0	0.59	7.22	2.078	0.90	1.30	2.735	2.253	15:32
4.0	0.58	7.00	2.108	0.90	1.30	2.735	1.934	16:19
7.0	0.57	6.70	2.168	1.00	1.70	2.176	1.820	16:15
10.0	0.60	6.47	2.082	1.30	2.20	1.573	1.312	15:26
10.0	0.60	6.49	2.082	0.60	5.10	2.190	2.418	13:15
20.6	0.52	5.72	2.449	1.30	4.90	1.130	0.857	15:56
20.6	0.48	6.01	2.599	1.10	5.20	1.276	1.071	15:21
20.6	0.54	6.08	2.339	0.60	19.30	1.805	1.500	13:11
55.0	0.47	5.36	2.727	1.10	89.30	0.930	0.588	13:07
55.0	0.56	5.40	2.311	1.90	34.90	0.570	0.247	15:51
101.6	0.57	3.33	2.600	4.30	150.40	0.241	0.161	15:47
154.0	0.40	4.02	3.379	4.80	950.40	0.218	0.178	13:04

Numerical instability within the solution for the mean square fade time expression is outlined in APPENDIX C. In a summary statement, it is known that large values of the small-scale scattering parameter β will be difficult to compute with readily available methods due to the numerical limit imposed by 64-bit Windows architecture. A workaround can be developed to handle the numerical difficulty; however this method is not explored in the included analysis. An alternative way of characterizing this behavior is simply stating that the contribution from the

additional scale in gamma-gamma distribution becomes negligible and therefore behavior approaches (single) gamma distributed irradiance [7, 13].

The analysis of mean square fade times begins with the 1.5mm aperture diameter data. Figure 52 plots the experimentally obtained data alongside the theoretical gamma-gamma mean square irradiance threshold crossing model. As expected, the shape of the model and the trend of the collected data are somewhat similar to those found for mean level crossings in Section 4.4.2 Mean Number of Level Crossings of Experimental Data. We find that the model parameters $\alpha_{gg\ msq}$ and $\beta_{gg\ msq}$ are comparable to those measured theoretically via C_n^2 and l_0. Additionally, the scintillation index calculated from the model parameters $\sigma^2_{I\ gg\ msq}$ compares reasonably well with that of the received irradiance data $\sigma^2_{I\ meas}$.

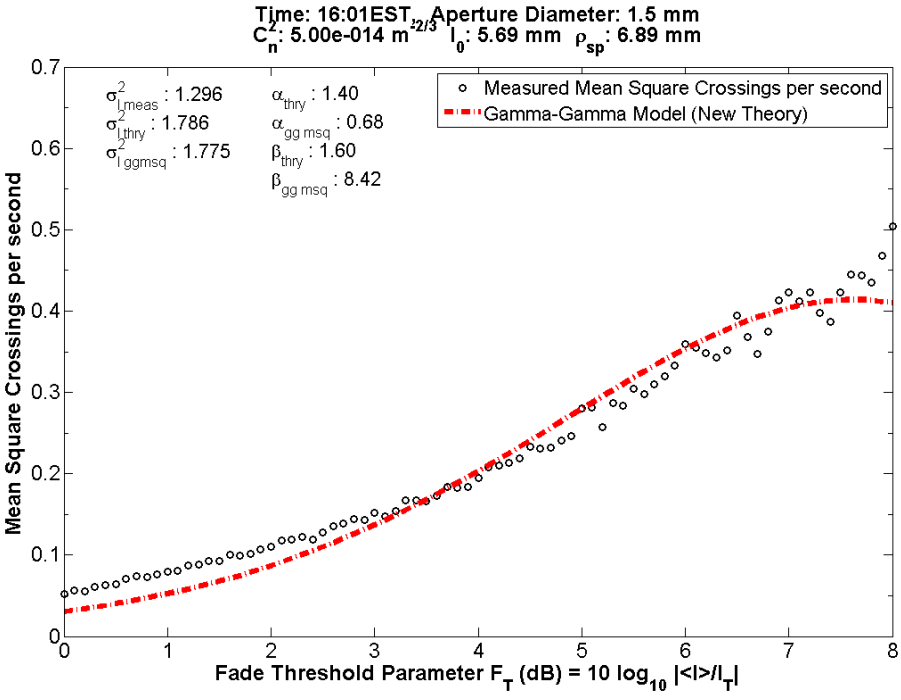

Figure 52: Experimental data mean square number of crossings per second, 1.5mm aperture diameter.

Figure 53 and Figure 54 show the mean square level crossing data taken with the 4mm aperture. We observe that the model parameters $\alpha_{gg\ msq}$ and $\beta_{gg\ msq}$ are comparable to those measured theoretically, α_{thry} and β_{thry}. And in suit, the scintillation index calculated from the model parameters $\sigma_{I\ gg\ msq}^2$ stands well with that of the received irradiance data $\sigma_{I\ meas}^2$. We will generally observe the peak 'hump' to move toward lower values of F_T as the receiver aperture size is increased. As has been mentioned, this will become more prevalent at larger aperture sizes where $D > 3\rho_{sp}$.

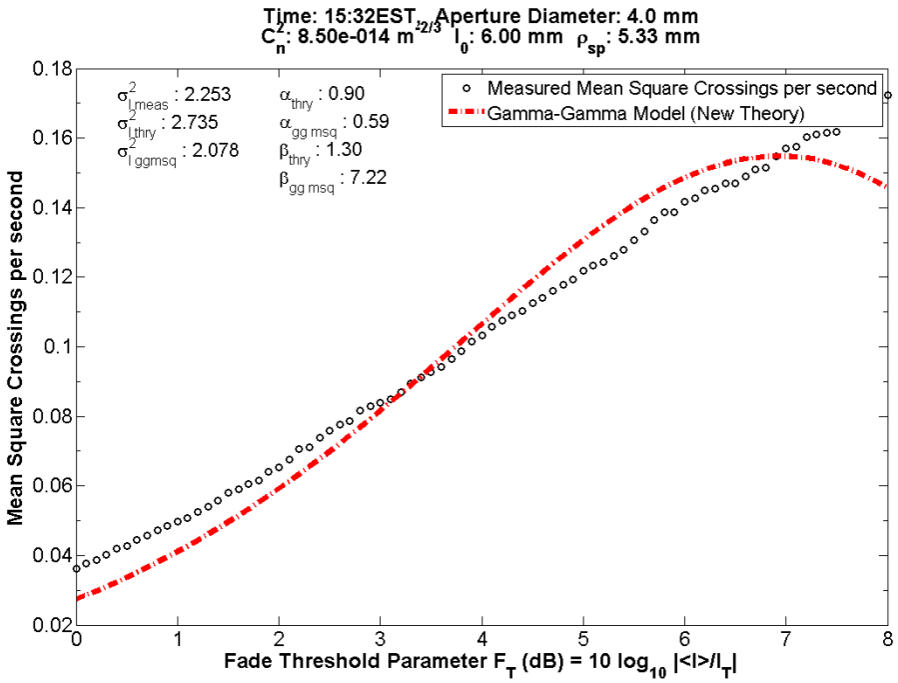

Figure 53: Experimental data mean square number of crossings per second, 4.0mm aperture diameter.

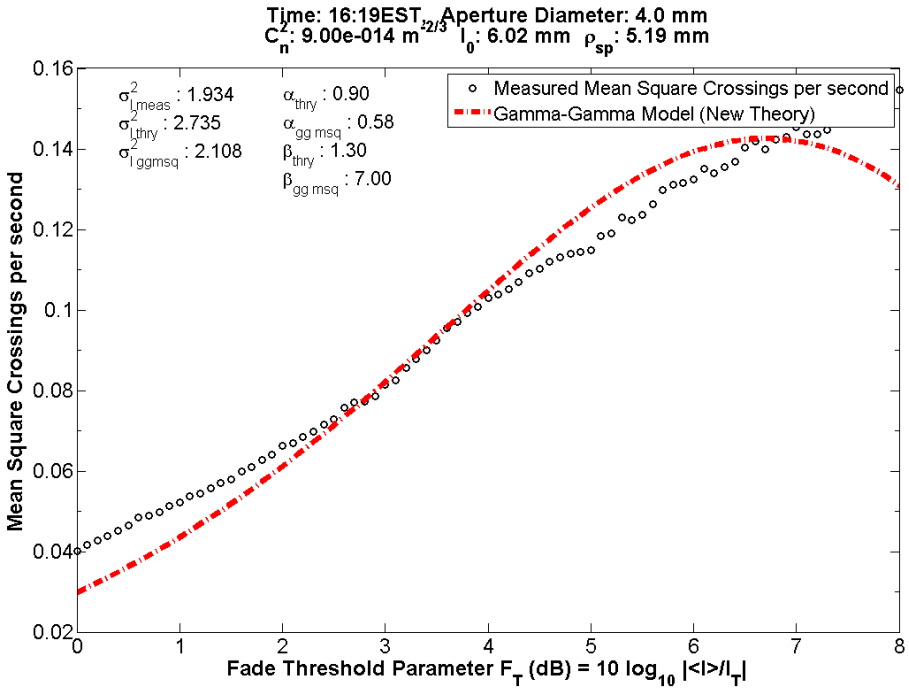

Figure 54: Experimental data mean square number of crossings per second, 4.0mm aperture diameter.

Figure 55 demonstrates the gamma-gamma mean square threshold crossing model with an aperture of 7mm diameter. Again, the modeled parameters compare well with those theoretically observed. The scintillation indices also agree to an acceptable extent.

Figure 56 and Figure 57 show the irradiance data collected with the 10mm aperture. We begin to see the hump moving toward lower values of F_T, and we note that the modeled small-scale parameter is beginning to see an increase. The experimentally observed scintillation index $\sigma^2_{I\,meas}$ and the theoretically observed scintillation index $\sigma^2_{I\,thry}$ match decently well with the modeled scintillation index.

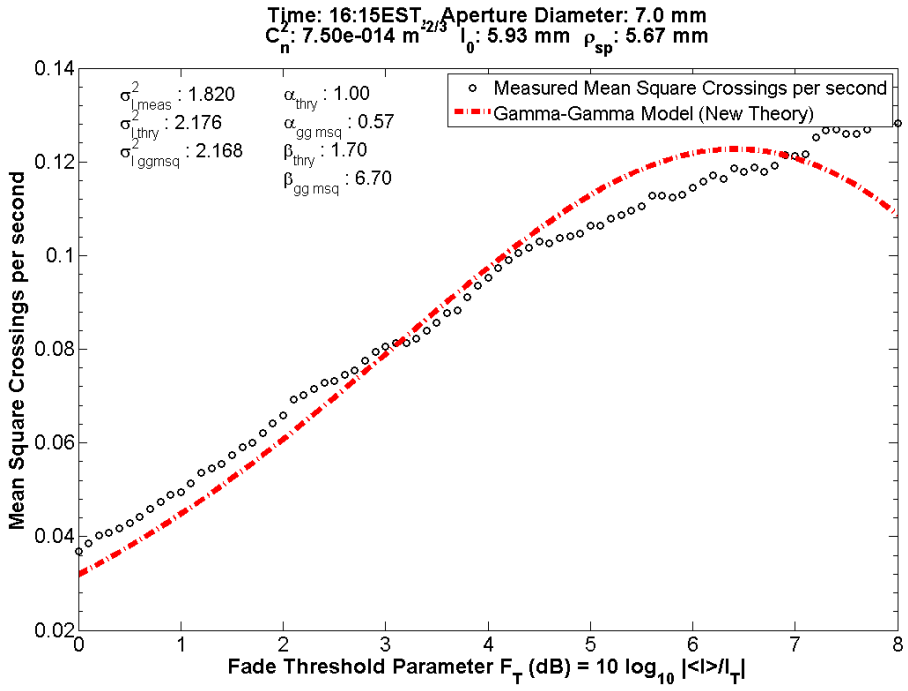

Figure 55: Experimental data mean square number of crossings per second, 7.0mm aperture diameter.

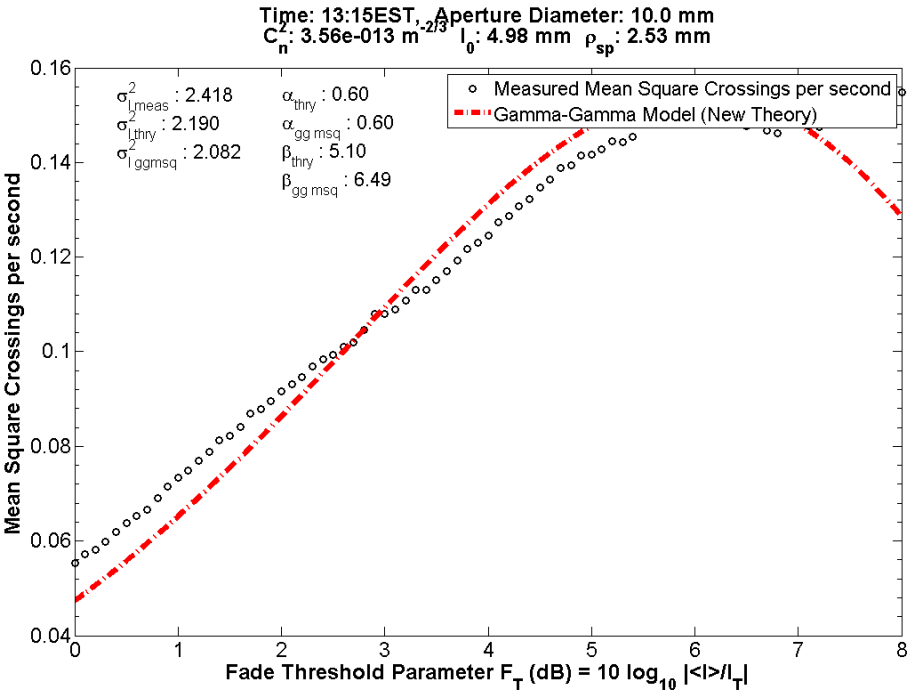

Figure 56: Experimental data mean square number of crossings per second, 10.0mm aperture diameter.

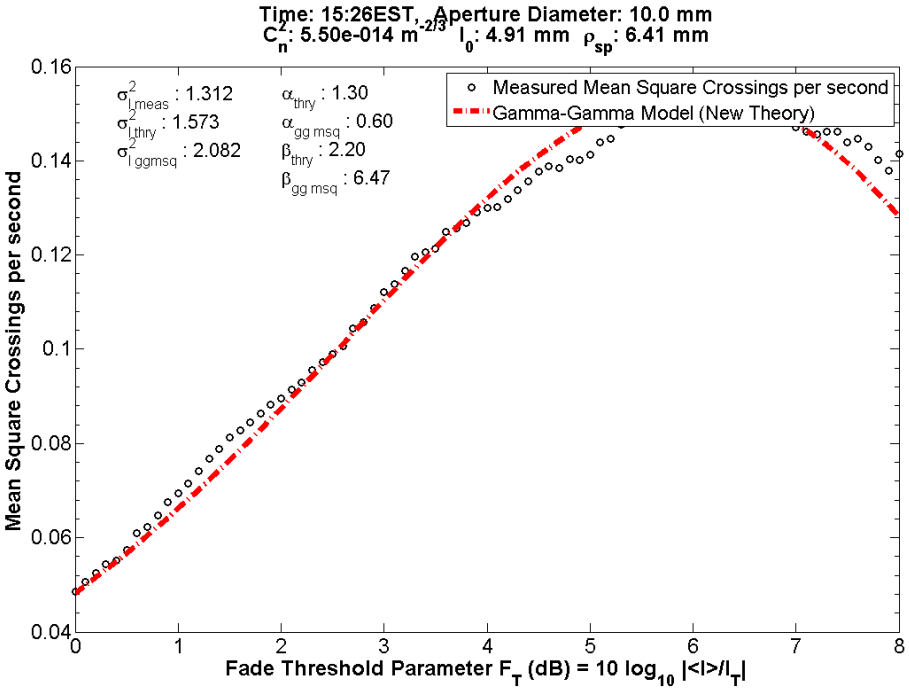

Figure 57: Experimental data mean square number of crossings per second, 10.0mm aperture diameter.

The data collections for the 20.6mm aperture are presented in Figure 71, Figure 72, and Figure 73. It is here that we begin to notice the difficulty in utilizing larger values of $\beta_{gg\ msq}$ due to numerical instability; this issue is further outlined in APPENDIX C. To overcome this obstacle, the small-scale gamma-gamma shape parameter for the mean square fade model is limited such that the calculation can be successfully completed. This will cause the mean square fade model's scintillation index $\sigma^2_{I\ ggmsq}$ to be slightly larger than it should be. The effect of this is demonstrated in the modeled values for 20.6mm and greater aperture diameters.

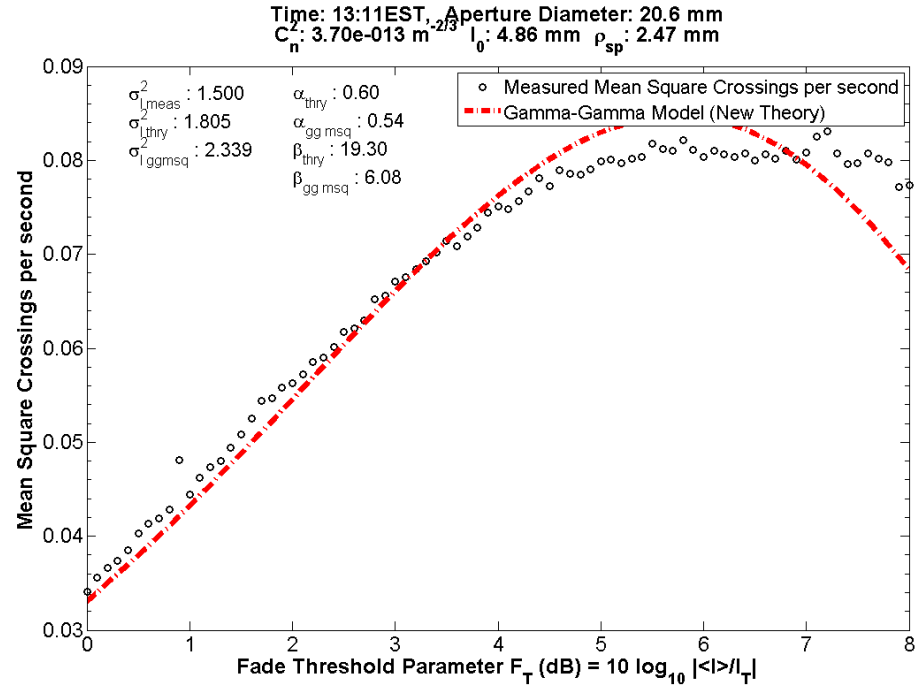

Figure 58: Experimental data mean square number of crossings per second, 20.6mm aperture diameter.

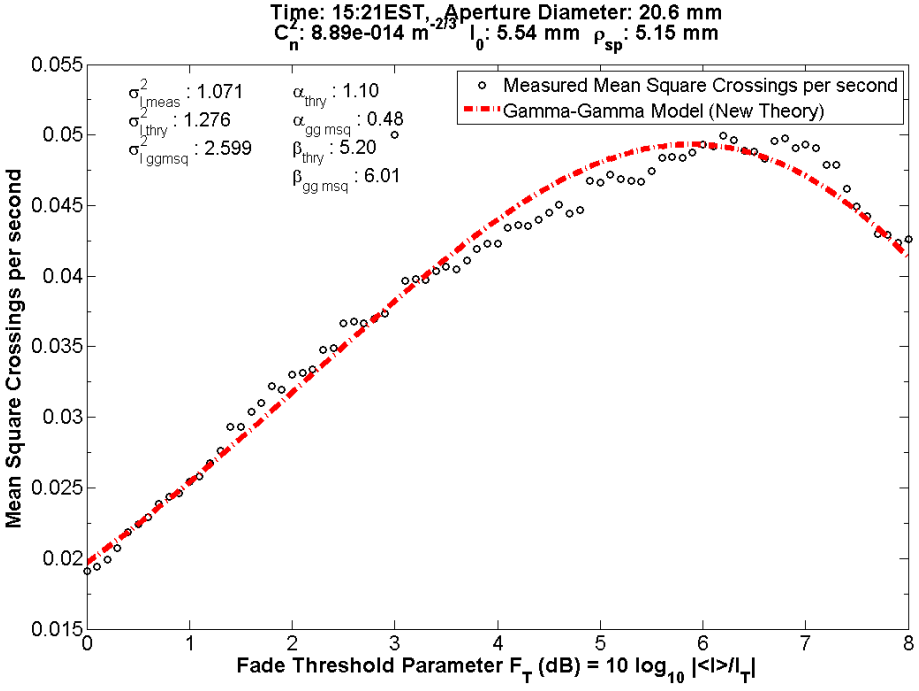

Figure 59: Experimental data mean square number of crossings per second, 20.6mm aperture diameter.

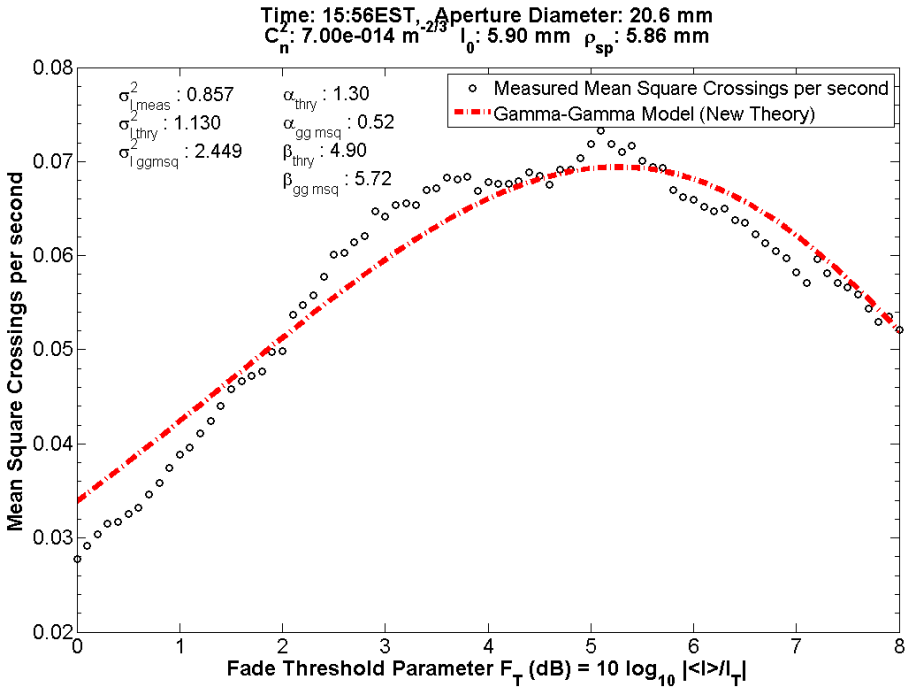

Figure 60: Experimental data mean square number of crossings per second, 20.6mm aperture diameter.

Received irradiance data for aperture of diameter 55mm is shown in Figure 61 and in Figure 62. In these plots the hump of the curve has continued to move towards lower values of F_T when compared to the results from smaller apertures. We notice the significance of limiting the small-scale parameter $\beta_{gg\ msq}$ for numerical stability on the modeled scintillation index $\sigma^2_{gg\ msq}$ (the scintillation indices differ by a significant amount). It is noted that the models definitely have the potential to correctly fit the data; however use of the theoretically observed small-scale parameter β_{thry} is impractical for computation and unable to be utilized for these larger apertures. Instead, the largest value of $\beta_{gg\ msq}$ that calculation will permit is utilized.

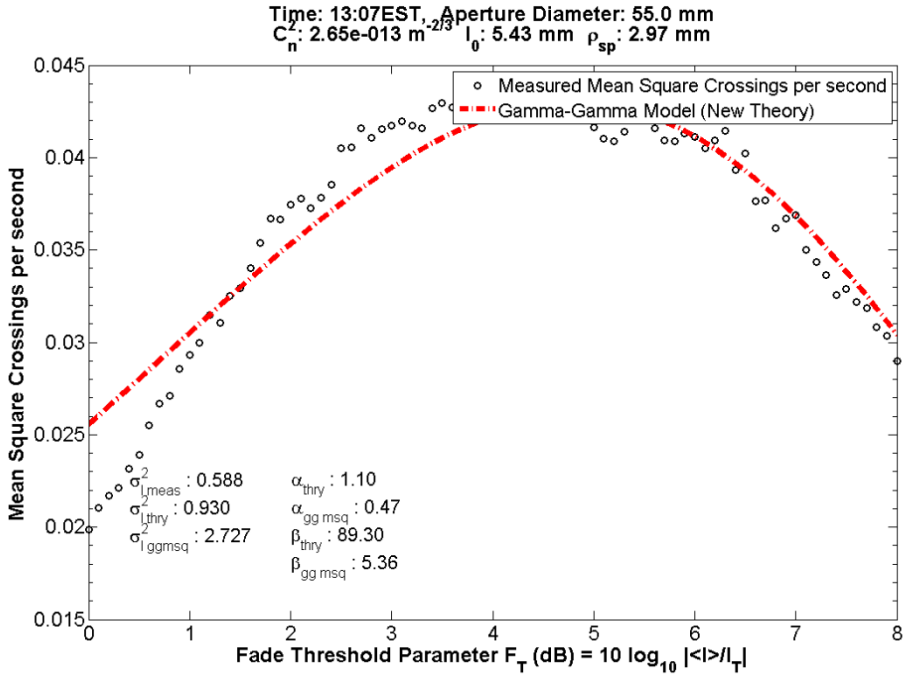

Figure 61: Experimental data mean square number of crossings per second, 55.0mm aperture diameter.

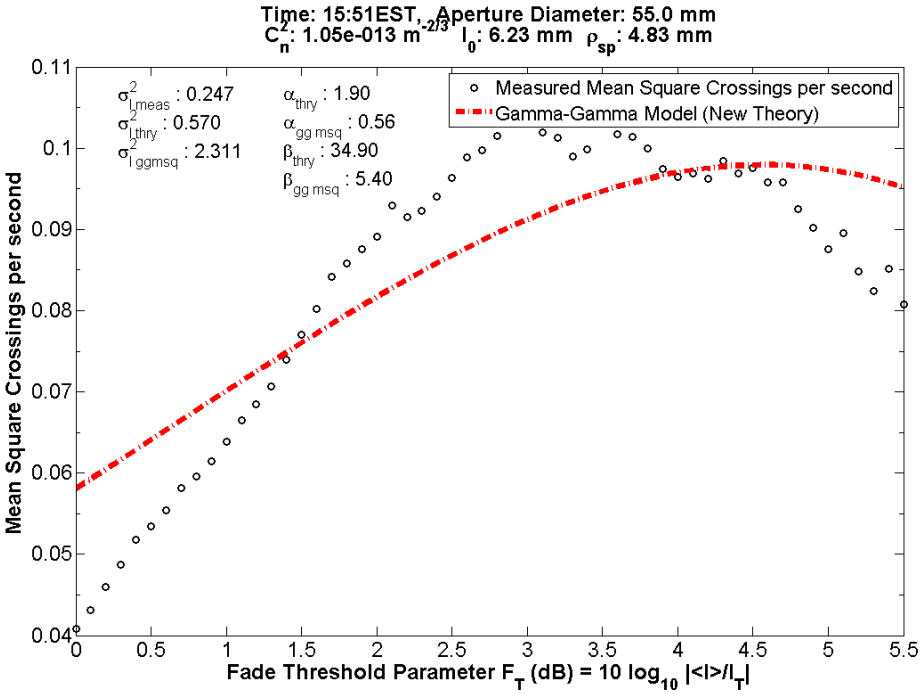

Figure 62: Experimental data mean square number of crossings per second, 55.0mm aperture diameter.

The largest aperture diameters of 101.6mm and 151mm are shown in Figure 63 and Figure 64, respectively. The peak of the curve continues to move toward lower values of F_T with increasing aperture diameters. Additionally, the calculation for such large values of the gamma-gamma model parameter $\beta_{gg\ msq}$ is not readily computable. We find the general shape of the curve to be about the same, and postulate that the model would fit the presented data if computation were made possible.

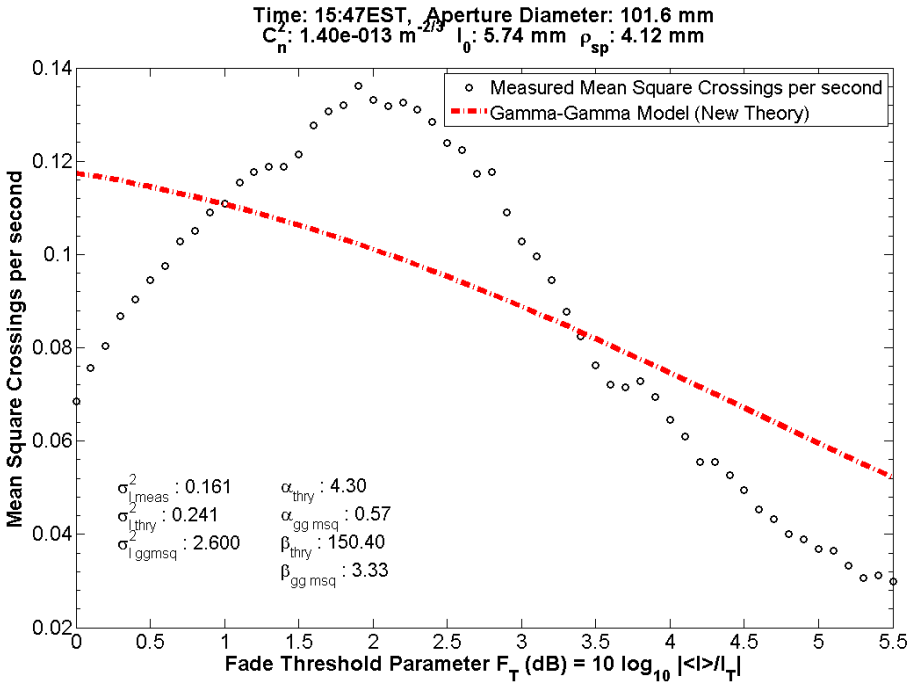

Figure 63: Experimental data mean square number of crossings per second, 101.6mm aperture diameter.

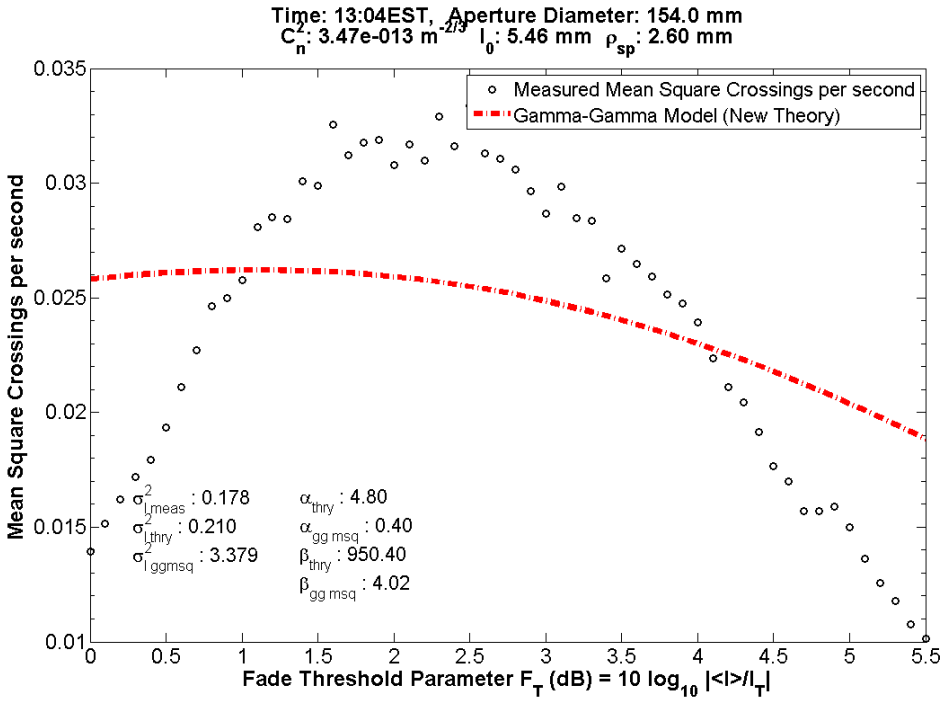

Figure 64: Experimental data mean square number of crossings per second, 154.0mm aperture diameter.

It is observed that with the mean square number of crossings per second, apertures of diameter 20.6mm or greater exhibit deviation from the theoretical expression. It is known that larger values of the gamma-gamma model parameter $\beta_{gg\ msq}$ attribute difficulty in numerical computation. An avoidance of the numerical computational issue is feasible, and would likely lead to better modeled results. It is also postulated that this is due to aperture averaging effects ($D > 3\rho_{sp}$), which are not taken into account with the gamma-gamma irradiance PDF model. It is suggested that a better PDF model, encompassing the effects of aperture averaging, would lead to more suitable results.

4.4.5 Standard Deviation of Fade Time of Experimental Data

We will now compare the developed theoretical model for the standard deviation in fade time for a gamma-gamma distributed irradiance signal with the experimental data collected at the ISTEF range. The theoretical model derived and utilized is detailed in Section 3.4.3 Gamma-Gamma Fade Time Statistics. Although variance of fade time is nominally mentioned, standard deviation of fade time may be readily substituted due to the half power relation between the two. This analysis will look at standard deviation of fade time as the time unit of *milliseconds* is more familiar, and is also readily comparable with mean fade time.

The data presented in this section are the amalgamation of the data presented in the previous sections (PDF, mean number of level crossings, mean fade-time, and mean square number of level crossings). With this in mind, one could reasonably expect the greatest deviance of experimental data from the theoretical model. However, the presented data represent a scenario in which the theoretically derived and experimentally obtained values show agreement.

We begin with the smallest receiver aperture of 1.5mm in diameter in Figure 65. As stated before in Section 4.4.4 Mean Square Number of Level Crossings of Experimental Data, the scintillation indices share agreement in these smaller apertures. The standard deviation of fade time shows a good agreement with the collected data at the lower irradiance thresholds I_T (large F_T). It would be best to agree in this region is it is the region most likely to be used when operating a communication system (greater average irradiance $\langle I \rangle$, lower threshold irradiance I_T). It is noticed that the gamma-gamma model exhibits an overestimation of standard deviation in fade

time as F_T becomes small. This appears to only be prevalent with the smaller aperture sizes and the model appears to improve as $\beta_{gg\ msq}$ increases (that is, until its increase leads numerical instability).

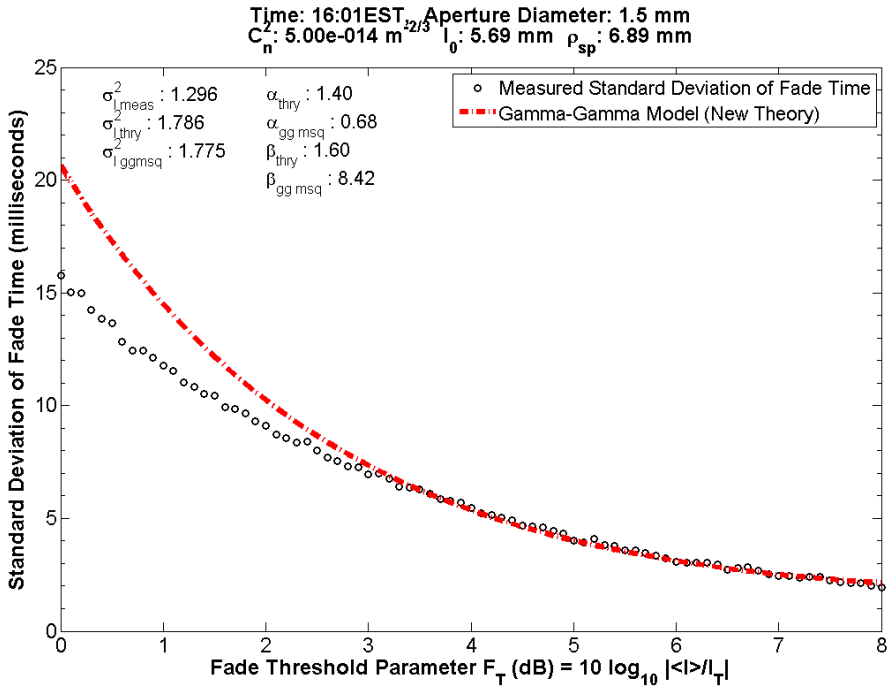

Figure 65: Experimental data standard deviation of fade time, 1.5mm aperture diameter.

The 4mm aperture data is analyzed in Figure 66 and again in Figure 67. The results appear almost identical to what is seen with the 1.5mm aperture. The results presented in this section signify that the standard deviation of fade-time is considerable when compared to the mean fade-time data presented in Section 4.4.3. The standard deviation of fade time is generally on the same order of magnitude as the mean fade time.

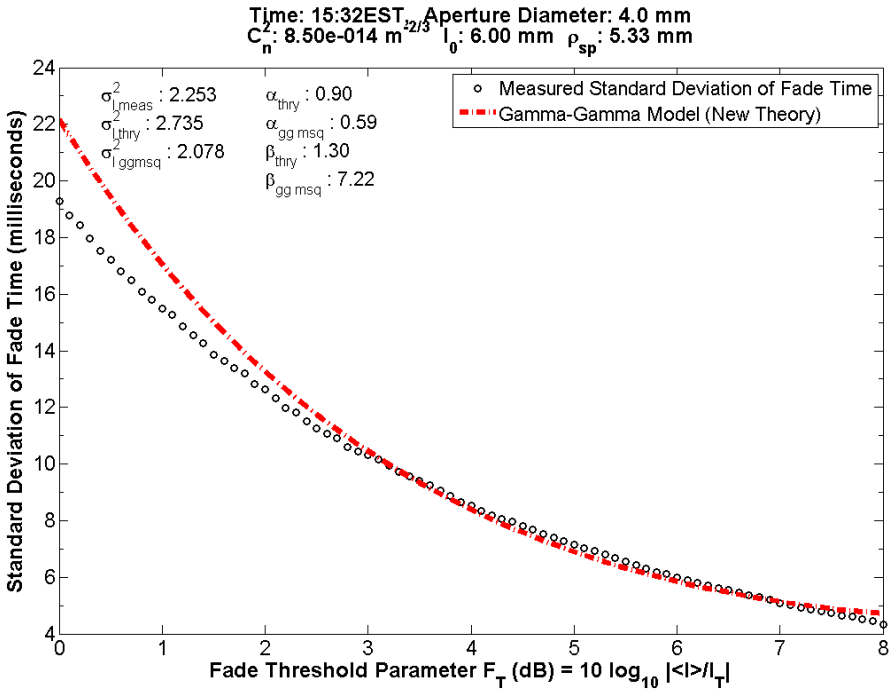

Figure 66: Experimental data standard deviation of fade time, 4.0mm aperture diameter.

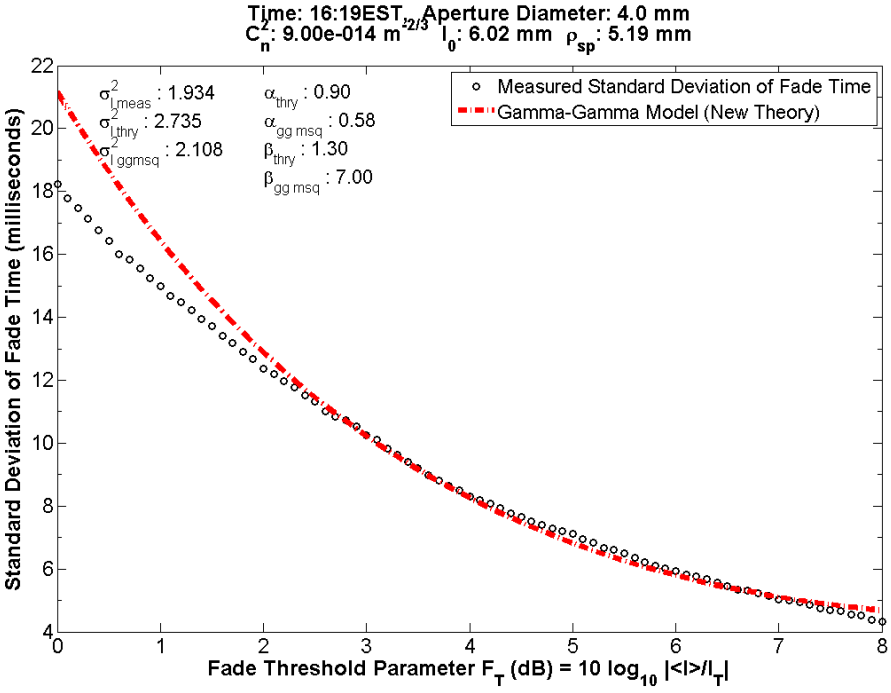

Figure 67: Experimental data standard deviation of fade time, 4.0mm aperture diameter.

As aperture size is slightly increased to 7mm, the data exhibits similar characteristics. Figure 68 shows the data, and we again note the agreement at the larger values of F_T. As mentioned in the previous section, the modeled parameters and the scintillation indices all show relatively good agreement. This continues strong motivation to conclude that the derived gamma-gamma model provides a feasible estimation of experimental data. Figure 69 and Figure 70 shows the data collected with the 10mm aperture. It is again noted that there is strong agreement between the experimental data and the gamma-gamma model predictions. Additionally, the experimentally determined and modeled gamma-gamma model parameters track one another a practical amount.

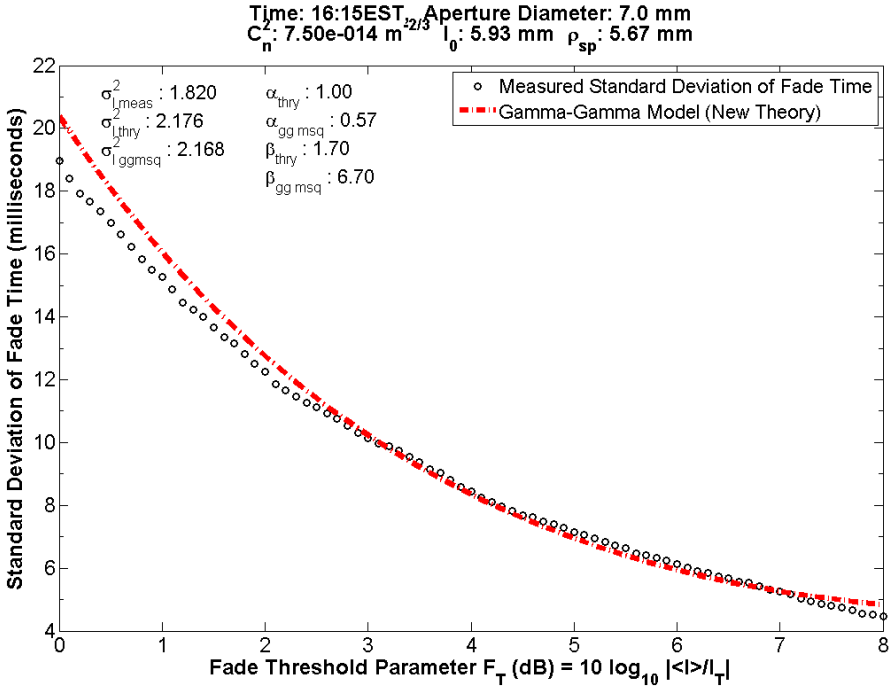

Figure 68: Experimental data standard deviation of fade time, 7.0mm aperture diameter.

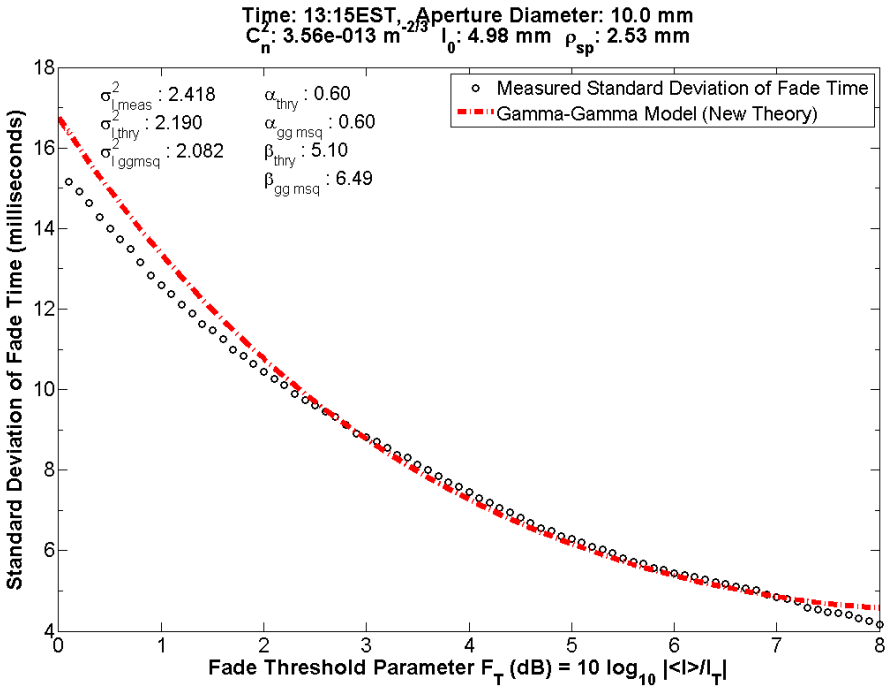

Figure 69: Experimental data standard deviation of fade time, 10.0mm aperture diameter.

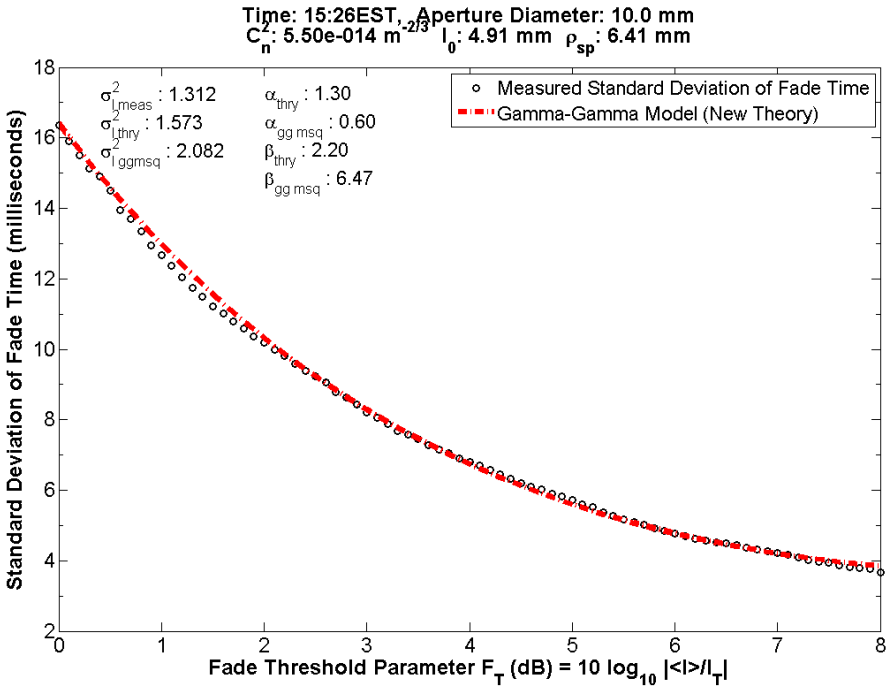

Figure 70: Experimental data standard deviation of fade time, 10.0mm aperture diameter.

As aperture size is continued to be increased, the comparison between gamma-gamma model parameters and experimentally determined parameters once again becomes problematic due to the numerical instability issue outlined in APPENDIX C. The irradiance data collected with the 20.6mm aperture is shown in Figure 71, Figure 72, and Figure 73. Aperture averaging criteria are met as we find that $D > 3\rho_{sp}$. Again, the gamma-gamma model does a good job of matching the shape of the data received within the experiment. The theoretically modeled parameters match up somewhat sensibly with the experimentally observed parameters. The predicted scintillation index $\sigma^2_{I\,ggmsq}$ in these three plots is consistently larger than the experimentally measured scintillation index $\sigma^2_{I\,meas}$. We again attribute this to not being able to effectively compute the gamma-gamma model standard deviation of fade time result for larger values of $\beta_{gg\ msq}$.

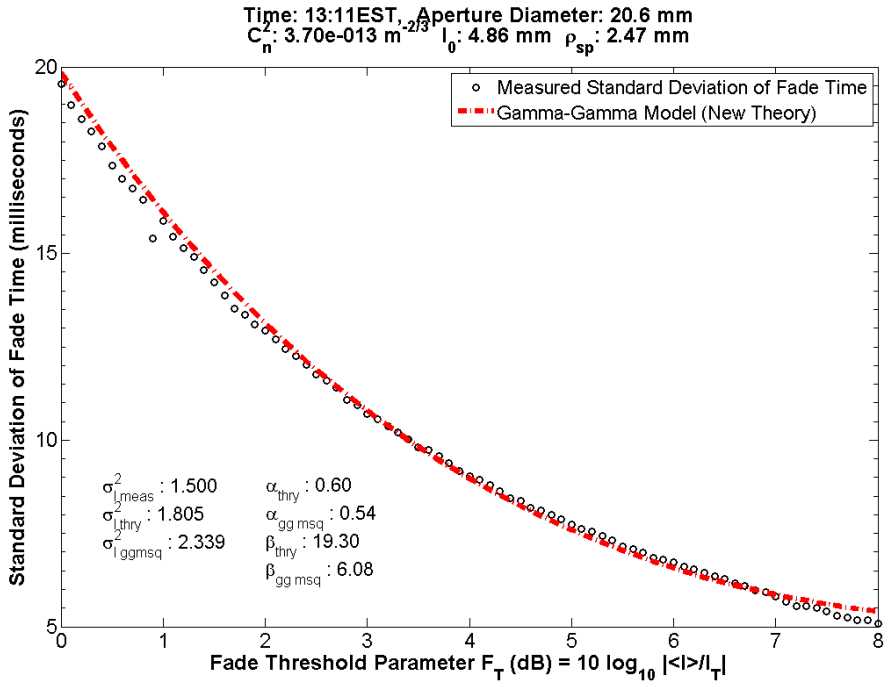

Figure 71: Experimental data standard deviation of fade time, 20.6mm aperture diameter.

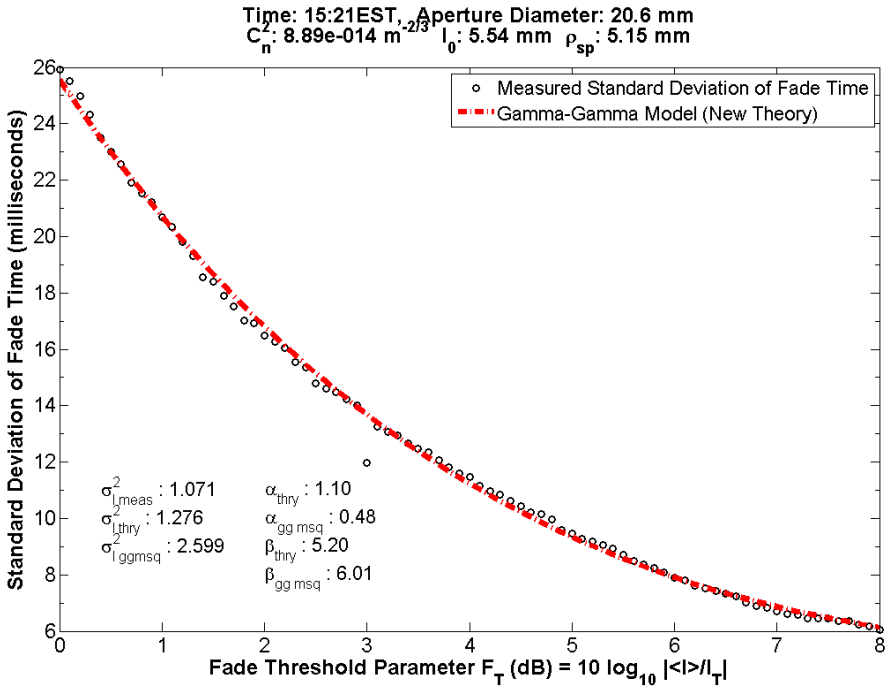

Figure 72: Experimental data standard deviation of fade time, 20.6mm aperture diameter.

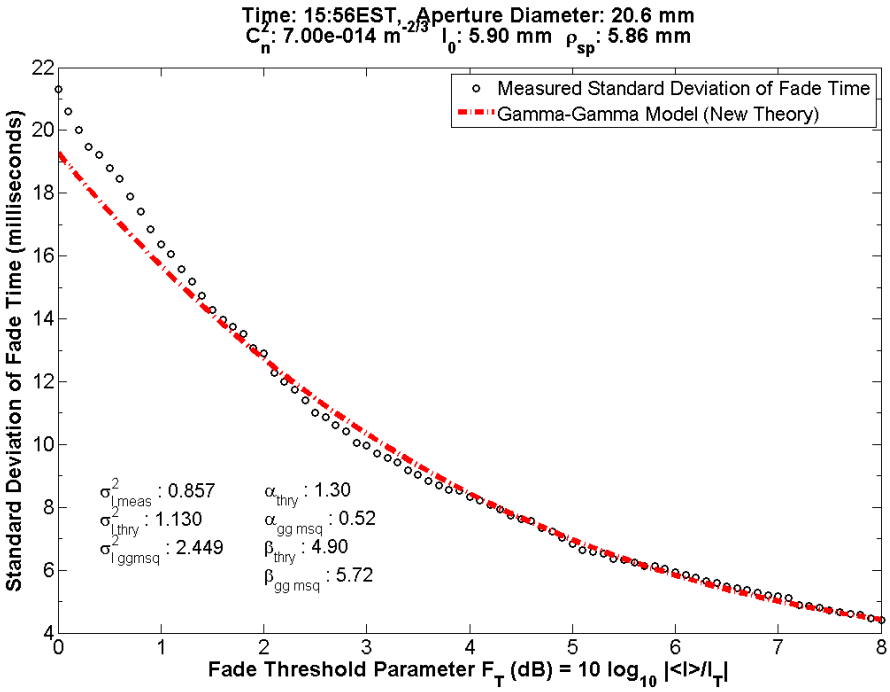

Figure 73: Experimental data standard deviation of fade time, 20.6mm aperture diameter.

Even as aperture diameter is further increased, the curve shape continues to maintain its consistency. The largest of apertures sizes are presented in Figure 74, Figure 75, Figure 76, and Figure 77. It is useful to discuss these plots as a collective because they portray similar results. We further see the gamma-gamma standard deviation of fade time model is able to successfully fit the provided data. However, it is again problematic to use the large $\beta_{gg\ msq}$ values in the computation ($\beta_{gg\ msq} > 8$). In line with this, the predicted scintillation index $\sigma^2_{I\,ggmsq}$ values in these plots are again larger than the experimentally measured scintillation index $\sigma^2_{I\,meas}$ values.

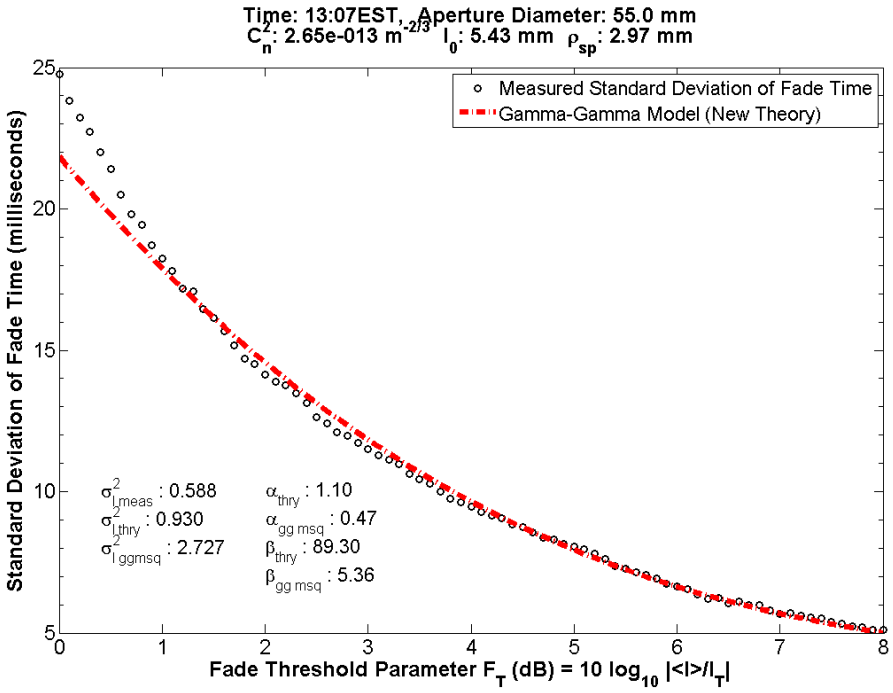

Figure 74: Experimental data standard deviation of fade time, 55.0mm aperture diameter.

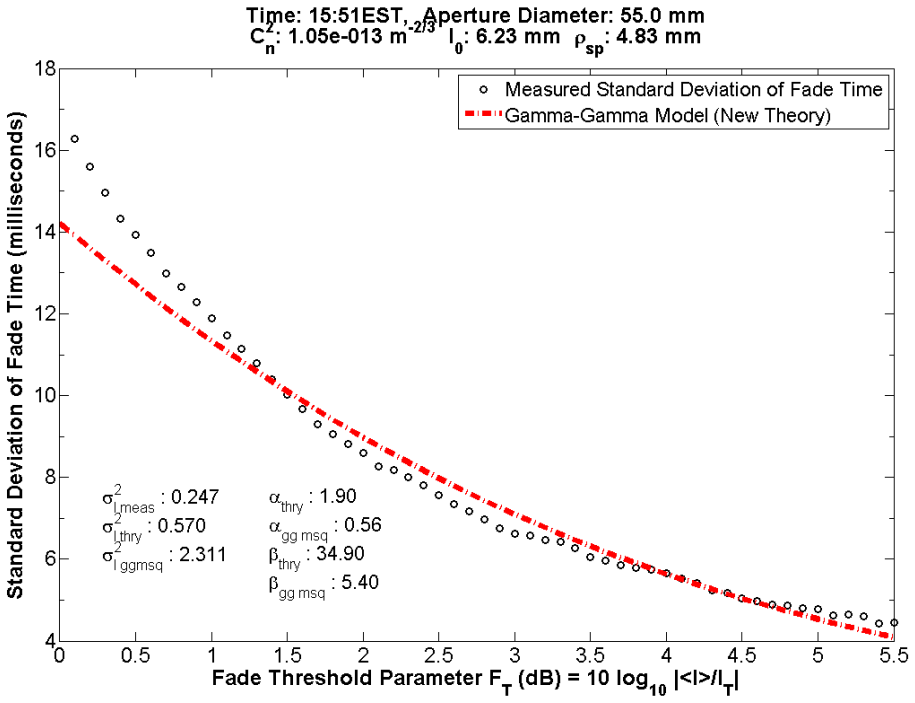

Figure 75: Experimental data standard deviation of fade time, 55.0mm aperture diameter.

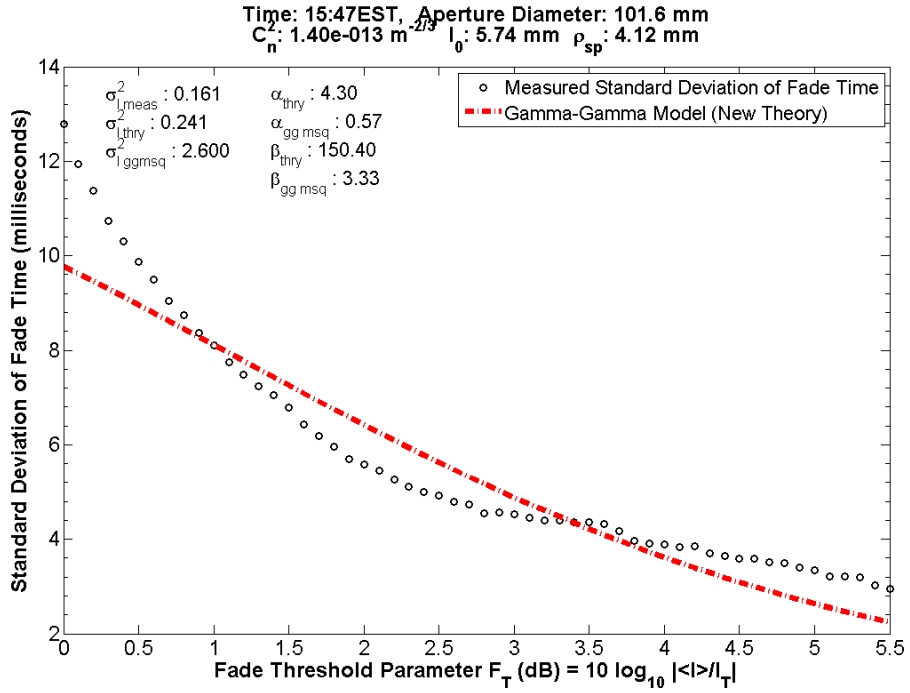

Figure 76: Experimental data standard deviation of fade time, 101.6mm aperture diameter.

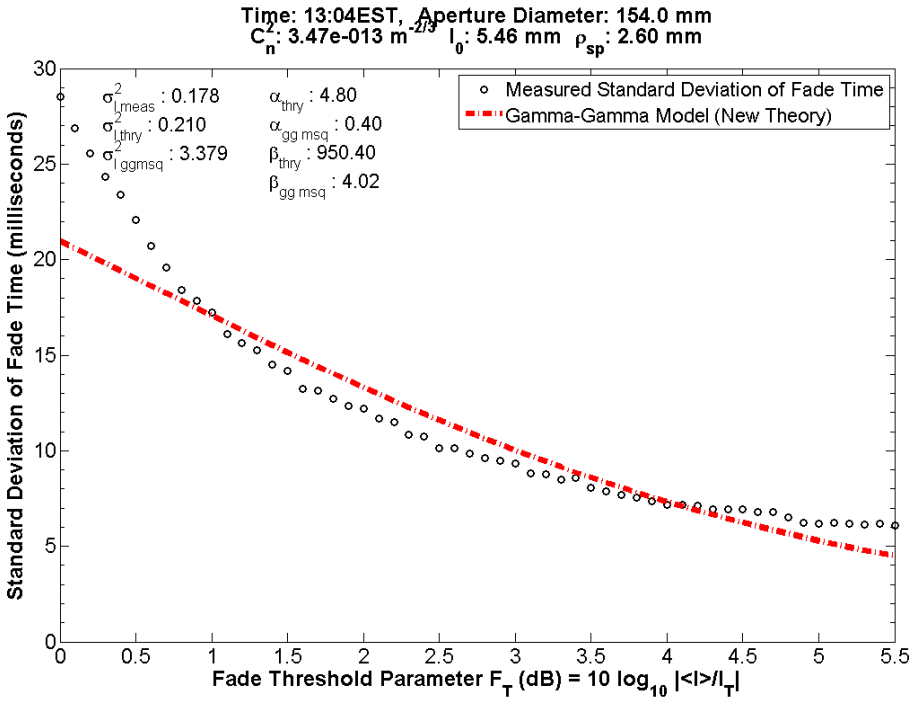

Figure 77: Experimental data standard deviation of fade time, 154.0mm aperture diameter.

As with mean fade time data, the standard deviation of fade time data were found to agree reasonably well with the experimental data. It has been pointed out that aperture averaging effects are not well encompassed within the gamma-gamma irradiance PDF model, and the influence of aperture averaging greatly affects the results of fade statistics. Data generally agree with theoretical predictions for aperture diameters of 20.6mm or less, and the data tend to deviate from the theoretical predictions for apertures of greater diameter. This is again attributed to the difficulty in computing the model with large values of $\beta_{gg\ msq}$.

It is observed that standard deviation in fade time can be as large as the mean fade time. This is thought to be an important observation as mean fade time is generally the main characteristic of the fade time distribution that is analyzed in the design of FSO communication systems [7, 10,

13, 34, 45]. Additionally, it is observed that the standard deviation in fade time can be theoretically determined given the mean fade time statistics. This is because the gamma-gamma model parameters α and β have been shown here to be somewhat consistent whether analyzing the PDF, mean fade time, or standard deviation of fade time.

4.5 Sources of Inaccuracy in Analysis

There are always non-deterministic factors introduced by measurements, whether they are expected or unexpected. The experiments presented in the analysis are no exception, and noise sources can be present within measurements. In our analysis, we will consider the following sources of error and address each individually: gamma-gamma PDF model inadequateness, aperture averaging, detector noise, sunlight irradiance, and error related to open-air operation.

The gamma-gamma PDF model is known to be a competitive model in the prediction of irradiance received through atmospheric turbulence; however it does display exact behavior [7, 12, 13, 45, 50]. The PDF is a model used to approximate a natural phenomenon, and therefore is always prone to predictive inaccuracy. Aperture averaging is an effect touched on within the gamma-gamma model, however not inherent within its modeled parameters. It is known that an increase in aperture size will decrease the received irradiance scintillation index σ_I^2, and decreasing the aperture size will have the converse effect. An increase an aperture size will increase both gamma-gamma model parameters α and β, however the small-scale scattering parameter β will exhibit the more drastic increase of the pair. As either parameter approaches infinity, the gamma-gamma model asymptotically approaches a gamma model [7]. The gamma-gamma model parameters (representing the number of large-scale scatterers α and the number of

small-scale scatterers β) both impart an increasingly large sensitivity on gamma-gamma modeled scintillation index as either of the model parameters becomes less than unity. This will make gamma-gamma model estimation of the scintillation index difficult when either of the gamma-gamma model parameters is small ($\alpha, \beta \to 1$).

As for noise influencing the shape of the irradiance PDF, portions representing detector noise were analyzed. Because laser power was at its maximum of 800mW and the experiment was conducted on a 1km range, SNR was deemed sufficiently large enough to neglect noise contribution. These contributions turn out to represent a portion of the signal PDF well below any detected laser signal, especially when compared to background sunlight. In both the preliminary setup and measurements, the thermal noise was essentially washed out by detected background/sunlight irradiance noise.

Since measurements were made during daytime hours, sunlight becomes an obvious contributor to detector noise in the form of *in-band* irradiance. Additionally, thermal cooling was not applied to the detector circuit although the detector was housed within an air-conditioned trailer (with the window open). Pointing inaccuracy (and even thermal expansion of optics) is also known to attribute a transmitter pointing mistake that is not correctable within the time frame of interest without additional compensation [1, 6, 10]. Stationarity of daytime conditions is also very difficult to achieve as the atmosphere's conditions generally change on the order of 30 minutes or less [4, 5].

The amount of sunlight noise signal versus received laser signal is quantified in the following item. Measurement of background/sunlight signal were made roughly every ten minutes, and found not to change too drastically as most of the data were collected during the period approaching and directly after the sun's midday. The transmitting laser was operated at approximately maximum power to obtain the largest possible SNR at the receiver (system was not considered *eye safe*). In each of the data runs, the measured detector noise was found to be at least 45 dB below the mean value of received irradiance $\langle I \rangle$. In the PDF plots, this can be seen because a slight spike of probability is present in the lowest presented irradiance values. Mean fade time and standard deviations of fade time analysis are not as heavily influenced by such irradiance values because the most desired threshold irradiance I_T values are many orders of magnitude larger.

5. CONCLUDING REMARKS

We have discussed the results of the experimental data as presented in Section 4 EXPERIMENTATION. This section will contribute as an expedited overview of the results presented in the aforementioned section.

The probability density function (PDF) of the received irradiance data were found to compare sensibly well with the gamma-gamma irradiance PDF model. Aperture averaging attributes to a reduction in the received scintillation index σ_I^2 as the aperture diameter D is increased well beyond the spatial coherence length ρ_{sp}. In the PDF, aperture averaging can also be seen to have the effect of narrowing the irradiance distribution's range.

Mean fade time of received irradiance were found to be agreeable with the results obtained in past experiments by other researchers. An increase in mean irradiance $\langle I \rangle$ (or decrease in threshold irradiance I_T) was shown to reduce fade time, as would be expected. The effect of aperture averaging was presented and discussed.

Variance (alternatively defined in terms of standard deviation) of received irradiance fade time data were found to agree well for smaller apertures where effects of aperture averaging are not present. When aperture averaging begins to become present, the gamma-gamma model small-scale scattering parameter β is known to contribute to the numerical instability seen in the model as its value will become large for the computations to follow. Given this hurdle, the experimental data matches the theoretically derived gamma-gamma variance in fade time expressions well

enough such that they can be considered agreeable. Future work may be done to approach or work around the pitfall in having a large value of β.

In conclusion, we note the procedure presented in Section 3.2.3 Fade Time Statistics shall remain valid regardless of the PDF model utilized. For other future work it is suggested that a more appropriate PDF, with a heavier focus on aperture averaging, should be applied in studies of these fade statistics. Additionally one may find a more streamlined method of collecting irradiance data with a series of receiver aperture sizes to allow for more data under similar atmospheric conditions.

APPENDIX A
INTEGRAL APPROXIMATION OF GAMMA-GAMMA MEAN FADE TIME

The modified Bessel function of the second kind $K_v(\cdot)$ is known to follow the integral relationship [44]

$$\int_0^\infty w^{v-1} \exp\left(-\alpha w - \frac{\beta}{w}\right) dw = 2\left(\frac{\beta}{\alpha}\right)^{v/2} K_v\left(2\sqrt{\alpha\beta}\right), \tag{A.1}$$

where w is a dummy variable, α is the large scale gamma-gamma parameter, β is the small scale gamma-gamma parameter. Plane wave expressions for large scale and small scale log-irradiance covariance functions were used to explore relations between b, b_x, and b_y. It was determined that $b_y \gg b_x$ and $b \approx b_y$ in the strong fluctuation regime. From this, the square root term in the integrand of $A(\alpha, \beta, I_T)$ may be approximated as [10]

$$\sqrt{b_x^2 I_T + b_y^2 w^2} = b_y w \sqrt{1 + \frac{b_x^2}{b_y^2}\frac{I_T}{w^2}} \approx bw, \tag{A.2}$$

where the approximations $b \approx b_y$ and $b_x^2/b_y^2 \approx 0$ were made from the previously stated observation. With this approximation, Equation (A.2) then becomes

$$A(\alpha, \beta, I_T)_{Approx\ 1} = b\int_0^\infty w^{\alpha-\beta-1/2} \exp\left[-\alpha w - \frac{\beta I_T}{w}\right] dw \tag{A.3}$$

$$= 2b\left(\frac{\beta I_T}{\alpha}\right)^{\frac{\alpha-\beta}{2}+\frac{1}{4}} K_{\alpha-\beta+1/2}\left(2\sqrt{\alpha\beta I_T}\right).$$

APPENDIX B
RELATION OF GAMMA-GAMMA MODEL PARAMETERS TO MEASURED PARAMETERS

This section details the calculation of gamma-gamma parameters from measured atmospheric parameters using spherical wave theory. The gamma-gamma PDF has two reciprocal parameters; α representing the number of large-scale scatterers observed by the aperture and β representing the number of small-scale scatterers observed by the aperture. In practice three parameters are use to encompass the current atmospheric channel conditions: the refractive index structure parameter C_n^2, the inner scale of atmospheric turbulence l_0, and the outer scale of atmospheric turbulence L_0. Commercial instruments are capable of measuring C_n^2 and l_0, and engineers have developed instrumentation to simultaneously measure L_0 as well [7, 8, 31, 48, 49].

The total number of large-scale and small-scale scatterers may be written as

$$\alpha = \frac{1}{\sigma_X^2} = \frac{1}{\exp(\sigma_{\ln X}^2) - 1}, \tag{B.1}$$

$$\beta = \frac{1}{\sigma_Y^2} = \frac{1}{\exp(\sigma_{\ln Y}^2) - 1},$$

where σ_X^2 and σ_Y^2 are the large-scale and small-sale scintillation indices, $\sigma_{\ln X}^2$ and $\sigma_{\ln Y}^2$ are the respective log-irradiance scintillation indices. It will be the focus of this section to relate the gamma-gamma model parameters α and β to the model's measureable parameters C_n^2, l_0, and L_0.

The Rytov variance is defined in the literature as [7, 13]

$$\sigma_R^2 = 1.23 C_n^2 k^{7/6} L^{11/6}, \tag{B.2}$$

with k being the wave number and L representing the path length. For mathematical compatibility, the Rytov variance is defined differently with each optical wave model. The *spherical wave* Rytov variance is written as

$$\beta_0^2 = 0.4\sigma_R^2. \tag{B.3}$$

In the regime of weak irradiance fluctuations, the large-scale log-irradiance scintillation index has been derived as [7, 53]

$$\sigma_{\ln X}^2(l_0) = 0.04\beta_0^2 \left(\frac{8.56 Q_l}{8.56 + Q_l + 0.20\beta_0^2 Q_l^{7/6}} \right)^{7/6} \times \left[1 + 1.75 \left(\frac{8.56}{8.56 + Q_l + 0.20\beta_0^2 Q_l^{7/6}} \right)^{1/2} - 0.25 \left(\frac{8.56}{8.56 + Q_l + 0.20\beta_0^2 Q_l^{7/6}} \right)^{7/12} \right], \tag{B.4}$$

where

$$Q_l = 10.89 L / k l_0^2. \tag{B.7}$$

In a somewhat similar manner, the small-scale log-irradiance scintillation index has been previously developed as [7, 53]

$$\sigma_{\ln Y}^2(l_0) = \frac{0.51\sigma_{SP}^2}{\left(1 + 0.69\sigma_{SP}^{12/5}\right)^{5/6}}, \tag{B.5}$$

where

$$\sigma_{SP}^2 \cong 9.65\beta_0^2 \left\{ 0.40(1+9/Q_l)^{11/12} \left[\sin\left(\frac{11}{6}\tan^{-1}\frac{Q_l}{3}\right) + \frac{2.61}{(9+Q_l^2)^{1/4}} \sin\left(\frac{4}{3}\tan^{-1}\frac{Q_l}{3}\right) - \frac{0.52}{(9+Q_l^2)^{7/24}} \sin\left(\frac{5}{4}\tan^{-1}\frac{Q_l}{3}\right) \right] - \frac{3.50}{Q_l^{5/6}} \right\}, \quad \text{(B.6)}$$

It is important to note that this analysis is valid for the spherical optical wave model, in weak-turbulence regime ($\sigma_I^2 < 1$), with an infinite outer-scale of turbulence ($L_0 = \infty$).

APPENDIX C
NUMERICAL STABILITY OF GAMMA-GAMMA MEAN SQUARE FADE TIME EXPRESSIONS

This section will focus on the expression derived in Section 3.4.2 Mean Square Level Crossing Rate of Gamma-Gamma Distributed Irradiance. We start with Equation (3.87) for the mean square number of crossings of a gamma-gamma distributed irradiance,

$$\overline{n^2} \cong \frac{4}{\pi}\left[\frac{\alpha\beta I_T}{\langle I\rangle}\right]^{\alpha+\beta}\left[\frac{K_{\alpha-\beta}\left(2\sqrt{\frac{\alpha\beta I_T}{\langle I\rangle}}\right)}{\Gamma(\alpha)\Gamma(\beta)I_T}\right]^2, \tag{C.1}$$

where α is the gamma-gamma model large-scale scattering parameter, β is the gamma-gamma model small-scale scattering parameter, I_T is the threshold irradiance level, and $\langle I\rangle$. Taking account of only the beginning term $[\alpha\beta I_T/\langle I\rangle]^{\alpha+\beta}$, we notice the power that which the expression is raised $(\alpha+\beta)$. We find a somewhat difficult situation arises, namely because of the α and β terms appearing in the power. This term has been found to be problematic in the presented analysis.

The largest floating point number that can be successfully utilized in 64-bit MATLAB is approximately 1.7977×10^{308} decimal; this value is found by typing *realmax* into the MATLAB console. For argument we choose some typical parameters, $I_T/\langle I\rangle = 1$, $\alpha = 2$ and $\beta = 100$. Putting these terms into the relation in C.1 we find

$$[\alpha\beta]^{\alpha+\beta} = [200]^{102} \cong 5.0706 \cdot 10^{234}, \tag{C.2}$$

which is beginning to approach the maximum computation limit. If were instead to choose $\alpha = 8$, it would be quickly found that MATLAB returns an answer of "*Inf*" (this is how the program signifies the maximum limit has been reached).

As such, care is taken to avoid combining large values of α and β in the data analysis. This is normally done by placing an upper bound on the size that which β may become. Since the gamma-gamma PDF parameters are mathematically reciprocal in the model (one can be traded in place with the other), care must also be taken to ensure such that $\alpha < \beta$. One possible approach to calculating large values of this parameter would be to take a half power of the parameters (stored as separate numerical results in computation, i.e. separate double floating point variables)

$$[\alpha\beta]^{\alpha+\beta} = [\alpha\beta]^{\frac{\alpha+\beta}{2}}[\alpha\beta]^{\frac{\alpha+\beta}{2}}. \tag{C.3}$$

One would employ successive operations in a manner to maintain numerical limits, such as to multiply the half powered term by a smaller number within the equation first. This would only work if a term elsewhere is less than unity, such that each number could be reduced before it would have to be multiplied. The main idea would be to avoid the upper numerical limit of computation, known as the "ceiling" value (1.7977×10^{308} decimal, as case).

REFERENCES

[1] J. Kiriazes, J. E. Valencia, R. Peach, C. Visone, G. Burdge, J. Vickers, T. Leclerc, P. Sauer, L. Andrews, and R. Phillips, "Performance of a 10 Gbps FSO System Implementing Novel Beam Tracking a Dynamic Buffering Modem," *IEEE Photonics Society*, July 2012 2012.

[2] B. Stadler, P. Kolodzy, A. Pike, T. G. Moore, D. W. Young, R. Smith, Z. Bagley, N. Plasson, B. Graves, D. Daugherty, J. Douglas, and T. Martin, "Optical RF communications adjunct: Coming of age," *IEEE Avionics, Fiber-Optics and Phototonics Technology Conference AVFOP '09*, 2009.

[3] J. C. Juarez, D. W. Young, R. A. Venkat, D. M. Brown, A. M. Brown, R. L. Oberc, J. E. Sluz, H. A. Pike, and L. B. Stotts, "Analysis of link performance for the FOENEX laser communications system," *SPIE Atmospheric Propagation IX*, vol. 8380, 2012.

[4] Vinnichenko, Penko, Shmeter, and Shur, *Turbulence in the free atmosphere*. New York: Consultants Bureau, 1980.

[5] H. A. Panofsky and J. A. Dutton, *Atmospheric turbulence : models and methods for engineering applications*. New York: Wiley, 1984.

[6] N. S. Kopeika, *A system engineering approach to imaging*. Bellingham, Wash.: SPIE Optical Engineering Press, 1998.

[7] L. C. Andrews and R. L. Phillips, *Laser beam propagation through random media*, 2nd ed. Bellingham, Wash.: SPIE Press, 2005.

[8] Scintec. (2006). *Why scintillation is superior*. Available: http://www.scintec.com/scinti.htm

[9] V. I. Tatarskii, *Wave propagation in a turbulent medium*. Newe York: Dover Publications, 1967.

[10] F. Stromqvist Vetelino, "Fade Statistics for a Lasercom System and the Joint PDF of a Gamma-Gamma Distributed Irradiance and its Time Derivative," Doctor of Philosophy, University of Central Florida Department of Mathematics, University of Central Florida, Orlando, Florida, 2006.

[11] F. Strömqvist Vetelino, C. Y. Young, L. C. Andrews, and J. Recolons, "Aperture averaging effects on the probability density of irradiance fluctuations in moderate-to-strong turbulence," *Optical Society of America Applied Optics*, vol. 46, 2007.

[12] L. C. Andrews and R. L. Phillips, *Field guide to probability, random processes, and random data analysis*. Bellingham, Wash.: SPIE Press, 2012.

[13] L. C. Andrews, R. L. Phillips, and C. Young-Hopen, *Laser beam scintillation with applications*. Bellingham, Wash.: SPIE Press, 2001.

[14] R. E. Hufnagel and N. R. Stanley, "Modulation transfer function associated with image transmission through turbulent media," *J. Opt. Soc. Am.*, vol. 54, pp. 52-61, 1964.

[15] M. Bass and Optical Society of America., *Handbook of optics*, 2nd ed. New York: McGraw-Hill, 1995.

[16] M. V. Klein, *Optics*. New York,: Wiley, 1970.

[17] E. Hecht and A. Zajac, *Optics*, 2nd ed. Reading, Mass.: Addison-Wesley Pub. Co., 1987.

[18] N. Focus, "High-Dynamic-range Power Sensors Models 2101 & 2103 User's Guide," 2010.
[19] D. A. Neamen, *Microelectronics circuit analysis and design*, 3 ed. New York, NY: McGraw-Hill, 2007.
[20] Thorlabs. (2012). Available: http://www.thorlabs.us/
[21] F. W. Schmidt, R. E. Henderson, and C. H. Wolgemuth, *Introduction to thermal sciences : thermodynamics, fluid dynamics, heat transfer*, 2nd ed. New York: Wiley, 1993.
[22] M. Van Dyke, *An album of fluid motion*. United States: The Parabolic Press, 1982.
[23] R. E. Hufnagel, "Propagation through atmospheric turbulence," in *The Infrared Handbook*, ed Washington, D.C.: USGPO, 1974.
[24] A. N. Kolmogorov, "The local structure of turbulence in an incompressible viscous fluid for very large Reynolds numbers," *C. R. (Doki) Acad. Sci. U.S.S.R. (Moscow)*, vol. 30, pp. 301-305, 1941.
[25] S. Bendersky, N. S. Kopeika, and N. Blaunstein, "Atmospheric optical turbulence over land in middle east coastal environments: prediction modeling and measurements," *Appl. Opt.*, vol. 43, p. 9, 2004.
[26] T. T. Leclerc, R. L. Phillips, L. C. Andrews, D. Wayne, and P. Sauer, "Prediction of the ground-level refractive index structure parameter from the measurement of atmospheric conditions " *SPIE*, vol. 7685, 4 May 2010 2010.
[27] L. C. Andrews, R. L. Phillips, D. T. Wayne, P. Sauer, T. Leclerc, and R. Crabbs, "Creating a Cn2 profile as a function of altitude using scintillation measurements along a slant path," *SPIE*, vol. 8238, 2012.
[28] D. L. K. Walters, K. E., "Atmospheric modulation transfer function for desert and mountain locations: the atmospheric effects on r0," *J. Opt. Soc. Am.*, vol. 71, p. 8, 1981.
[29] A. L.C., R. L. Phillips, D. T. Wayne, T. Leclerc, P. Sauer, R. Crabbs, and J. Kiriazes, "Near-ground vertical profile of refractive index fluctuations," *Proc. SPIE*, vol. 7324 2009.
[30] Y. Han Oh, "Estimating optical turbulence effects on free-space laser communication: modeling and measurements at ARL's A_LOT facility," *SPIE*, vol. 5550, p. 8, 2004.
[31] D. T. Wayne, R. L. Phillips, L. C. Andrews, F. Stromömqvist Vetelino, B. Griffis, M. R. Borbath, D. J. Galus, and C. Visone, "Measuring optical turbulence parameters with a three-aperture receiver," *Proc. SPIE*, vol. 6709, 2007.
[32] S. D. Lyke, D. G. Voelz, and M. C. Roggemann, "Probability density of aperture-averaged irradiance fluctuations for long range free space optical communication links," *Appl. Opt.*, vol. 48, pp. 6511-6527, 2009.
[33] F. Strömqvist Vetelino, C. Young, L. C. Andrews, and J. Recolons, "Aperture averaging effects on the probability density of irradiance fluctuations in moderate-to-strong turbulence," *Appl. Opt.*, vol. 46, pp. 2099-2108, 2007.
[34] F. Strömqvist Vetelino, C. Young, and L. C. Andrews, "Fade statistics and aperture averaging for Gaussian beam waves in moderate-to-strong turbulence," *Optical Society of America Applied Optics*, vol. 46, p. 10, 2007.
[35] F. Strömqvist Vetelino, B. Clare, K. Corbett, C. Young, K. Grant, and L. C. Andrews, "Characterizing the propagation path in moderate to strong optical turbulence," *Appl. Opt.*, vol. 45, pp. 3534-3543, 2006.

[36] J. G. Proakis and M. Salehi, *Digital Communications*, 5 ed. New York, NY: McGraw-Hill, 2008.
[37] B. Sklar, *Digital communications fundamentals and applications*. Upper Saddle River, NJ: Prentice-Hall Inc., 2001.
[38] D. Middleton, *Topics in communication theory*. New York,: McGraw-Hill, 1965.
[39] D. Middleton, *An introduction to statistical communication theory*. New York,: McGraw-Hill, 1960.
[40] E. Vanmarcke, *Random fields analysis and synthesis revised and expanded new edition*. Hackensack, NJ: World Scientific Publishing Co. Ptd. Ltd., 2010.
[41] J. S. Bendat, *Principles and applications of random noise theory*. New York, NY: John Wiley & Sons, Inc., 1958.
[42] L. C. Andrews and R. L. Phillips, *Mathematical techniques for engineers and scientists*. Bellingham, Wash.: SPIE Press, 2003.
[43] L. Devroye, *Non-uniform random variate generation*. New York: Springer-Verlag, 1986.
[44] L. C. Andrews, *Special functions of mathematics for engineers*. Bellingham, Wash., USA: SPIE Optical Engineering Press Oxford University Press, 1998.
[45] P. R. Sauer, R. L. Phillips, L. C. Andrews, D. T. Wayne, and T. T. Leclerc, "Analysis of fading in the propagation channel for the ORCA laser communication system," *SPIE Proc. Atmospheric Propagation VIII,* vol. 8038, 2011.
[46] J. S. Bendat and A. G. Piersol, *Random data : analysis and measurement procedures*, 2nd ed. New York: Wiley, 1986.
[47] "Operators manual for a sonic anemometer/thermometer, Rev.H2," I. Applied Technologies, Ed., ed. Longmont, CO, 2008.
[48] Scintec. (2006). *Surface Layer Scintillometers - Scintec A.G. - SLS 20 - Product Manual*. Available: http://www.scintec.com/download.htm
[49] Scintec. (2006). *Boundary Layer Scintillometers - Scintec A.G. - BLS 900 - Product Manual*. Available: http://www.scintec.com/download.htm
[50] D. T. Wayne, "The PDF of irradiance for a free-space optical communications channel a physics based model," University of Central Florida, Orlando, Fla., 2010.
[51] L. C. Andrews, *Field guide to atmospheric optics* SPIE Publications, 2004.
[52] N. I. Corporation. (2010). *NI 9234 24-bit DAQ Data Sheet*. Available: http://www.ni.com/
[53] L. C. Andrews, R. L. Phillips, and B. K. Shivamoggi, "Relations of the parameters of the I-K distribution for irradiance flctuations to physical parameters of turbulence," *Appl. Opt.*, vol. 27, p. 7, 1988.